Department of Precision and Microsystems Engineering

# Inkjet-printed boron-doped diamond electrode sensor for the detection of the antidepressants venlafaxine and desvenlafaxine

Thomas Peeters

Report no : 2023.086
Coach : Dr. S. Baluchová
Professor : Dr. J.G. Buijnsters
Specialisation : Micro and Nano Engineering (MNE)
Type of report : Thesis
Date : 18 October 2023

# Inkjet-printed boron-doped diamond electrode sensor for the detection of the antidepressants venlafaxine and desvenlafaxine

By

**Thomas Peeters**

in partial fulfilment of the requirements for the degree of

**Master of Science**
in Mechanical Engineering

at the Delft University of Technology,

to be defended publicly on 18-10-2023

Student number: 4577434

| | | |
|---|---|---|
| Thesis supervisor: | dr. J.G. Buijnsters | TU Delft |
| | dr. S. Baluchová | TU Delft |
| Thesis committee: | dr. J.G. Buijnsters | TU Delft |
| | dr.ir. S. Vollebregt | TU Delft |
| | dr. S. Baluchová | TU Delft |

# Acknowledgements

First, I would like to express my thanks to my supervisor, Dr. Ivan Buijnsters. His enthusiasm and openness during this project has been of significant help, and his knowledge and experience supported the completion of this research significantly. I also would to thank my other supervisor Dr. Simona Baluchová for her continued assistance throughout this work. Her experience in electrochemical sensing was invaluable during the progress of this work. Her prompt replies to any questions and excellent advice was a constant source of encouragement during this project. I am grateful for all the support given during this project by my supervisors.

Furthermore, I would like to thank Zhichao Liu for his involvement and help during the inkjet printing of the nanodiamond seeds. His previous experience with this subject helped ease the start of the printing process significantly. Also, I would like to acknowledge my fellow students, Stach van Leeuwen and Dilpreet Singh. We all did our thesis at a similar time and with Dr. Ivan Buijnsters, this allowed for good discussion and cooperation with each other during the research process.

My gratitude goes to my family and friends for all the assistance given throughout the thesis project. Their support and encouragement are what continue to motivate me. Thank you for being there for me.

*Thomas Peeters*
*Rijswijk, October 2023*

# Abstract

Boron-doped diamond (BDD) is a popular material for electrodes and it exhibits metal-like conductivity when a sufficient quantity of boron atoms is incorporated in the diamond lattice. BDD has distinct advantages over alternative electrode materials. It has diamond's chemical stability and biocompatibility in conjunction with excellent electrochemical characteristics including large potential window and low background current. Thus, BDD has great potential as an electrode material in electrochemical sensors for the detection of pharmaceutical compounds.

Of particular interest is the monitoring of the antidepressants venlafaxine (VF) and desvenlafaxine (DVF). These pharmaceuticals are prescribed to those suffering from major depressive disorder, generalized anxiety disorder, panic disorder and/or social anxiety disorder. However, they can have adverse effects on the health and behaviour of aquatic life, and harmful quantities have already been detected in nature. Monitoring of DVF and VF in a patient's blood and urine is required to ensure correct dosage levels**,** which in turn could mitigate environmental pollution. An electrochemical sensor with BDD electrodes would be well-suited for this application.

In this research, two distinct BDD electrode materials were used for the electrochemical detection of VF and DVF. For initial experimentation, a robust and well-established free-standing BDD electrode type was utilized in a voltammetric study. Optimized detection conditions were achieved on hydrogen-terminated BDD for DVF and oxygen-terminated BDD for VF in a 0.1 M $H_2SO_4$ solution (pH 0.6), yielding limits of detection (LOD) of 0.31 µM and 0.17 µM and limits of quantification (LOQ) of 0.94 µM and 0.57 µM for VF and DVF, respectively. The scan rate study demonstrated that the oxidation reactions for both compounds are diffusion controlled. VF and DVF have excellent repeatability in the presence of several interfering compounds, such as inorganic ions, sucrose, glucose, and dopamine. To assess the suitability of the detection method, electroanalysis of VF and DVF in synthetic human serum, synthetic urine, and river water was conducted. Besides, a commercially available BDD electrode chip was employed for VF and DVF detection under optimized conditions. The measurement results of the different BDD electrodes were compared; in particular, when the less robust commercial electrode chip was used, larger values of LOD (1.9 µM and 8.0 µM) and LOQ (5.8 µM and 24.1 µM) were reached for VF and DVF, respectively. The fabrication of analogue BDD-based electrochemical sensors by utilizing direct inkjet printing of diamond nanoparticles on silicon substrates was evaluated in parallel. Various electrode designs were successfully printed, however subsequent chemical vapor deposition of thin-film BDD did not satisfy the required electrode quality. Notwithstanding, the use of a BDD electrode allows for the creation of a modification-free and promising practical method for VF and DVF detection.

# Contents

# 1 Introduction

Depression is a severe mental health issue that affects hundreds of millions of people worldwide [1]. This has led to a high usage of the antidepressants venlafaxine (VF) and desvenlafaxine (DVF) [2]. These serotonin-norepinephrine reuptake inhibitors are compounds which combat the symptoms of depression [3, 4]. It is therefore of high importance to monitor a patient's blood concentration levels to limit the excess intake and maintain treatment efficacy. Substantial amounts of both compounds VF (5% as VF, 29% as DVF) and DVF (45%) are excreted out of the body and end up as environmental pollutants. Also, these antidepressants have been identified as a water pollutant on a large scale, both in wastewaters and surface waters [5]. DVF and VF are toxic to aquatic life and poorly degradable and therefore it is crucial to limit its presence in the environment, and they have therefore been placed on the European Union watchlist [6, 7]. It is imperative that suitable methods are developed for the monitoring of VF and DVF in clinical (biological fluids obtained from patients) and environmental samples.

An excellent technique for their detection is electrochemical sensing and conductive diamond is a material that has garnered interest in this field in recent years. Diamond is a desired material for such application due to its excellent properties, in particular its extreme mechanical performance, biocompatibility, and chemical stability [8, 9]. Electrically conductive thin-film diamond, which is synthesized by using chemical vapor deposition (CVD), is of particular interest for these applications. CVD allows for the coating of different substrate materials by a thin film (micron-scale) of polycrystalline diamond. CVD has enabled a wide field of applications for synthetic diamond and allows for the doping of boron in the diamond lattice. This boron-doped diamond (BDD) is electrically conductive and serves as electrode material in electrochemical (bio)sensors. BDD preserves diamond's desirable features and functions as an electrode with a wide potential window, low background and capacitive currents, and low signal noise. It can outperform more standard electrode materials (e.g., platinum/silver) and other ($sp^2$) carbon-based electrodes [10].

In standard CVD diamond growth experiments, an entire substrate is usually seeded with diamond nanoparticles and thin-film diamond growth takes place uniformly. Diamond patterning takes place post-growth by using etching [11], lithography [12], or laser machining methods [13] in a cleanroom. These methods are time-consuming, resource intensive and above all expensive. A simpler method for diamond patterning is to use a bottom-up approach, in which the nanodiamond particles are seeded in the desired pattern pre-growth, and thus CVD growth only takes place in desired locations. One of these methods is inkjet printing. This technique allows for freedom in electrode design and recent studies in our group [14] have explored the patterned growth of BDD through inkjet printing for the manufacturing of miniaturized electrodes. Further investigation into this technique is important to further improve the process and to simplify the manufacturing of complex-shaped BDD electrodes for applications in electroanalysis.

The main objectives of this MSc thesis are to investigate and optimize the electroanalytical method for the detection of DVF and VF on BDD electrodes and to employ the inkjet-printed three-electrode BDD sensors for such purpose. The thesis is divided into six chapters, with the first being the introduction. Chapter two encompasses a literature review on VF, DVF, and synthetic diamond. The third chapter explains the research focus, while the fourth chapter delves into the research methodology. In chapter five, the analysis of the obtained results is presented and discussed. Lastly, in chapter six, the research conclusions are summarized, and the recommendations for future investigations are provided.

# 2 Literature Review

## 2.1 Pharmaceutical pollution

One of the areas where electrochemical BDD sensors can be applied is the detection of environmental pollutants and specifically pharmaceuticals. In this chapter, first, the necessity behind sensing these pharmaceutical compounds is discussed. Second, the antidepressants desvenlafaxine and venlafaxine are investigated, and their current (electrochemical) sensing possibilities are described.

### 2.1.1 The pollution of the world's rivers

In Figure 2.1, an overview of pharmaceutical pollution of the world's rivers can be found as investigated by Wilkinson et al. [5]. They studied the pollution levels of several rivers in each continent and found a wide variety of toxic concentrations for several chemicals. The chemicals range from fluoxetine, which was present at 0.1% of all tested sites, to carbamazepine, which was present in more than 60% of all tested sites (Fig. 2.1a). Figure 2.1b also shows that many sites contain more than a single active pharmaceutical ingredient (API). This means that toxicological effects could be even greater as APIs can react with each other to more dangerous substances. It is therefore imperative that methods are developed to detect these pollutants such that filtration steps can begin to take place. Many of these chemicals have been researched with conventional electrodes and there has been a great deal of interest in the use of BDD electrodes for these sensors [15–25]. Pharmaceuticals that have not yet been investigated with BDD electrodes are desvenlafaxine and venlafaxine, even though they are present in over a third of all examined rivers.

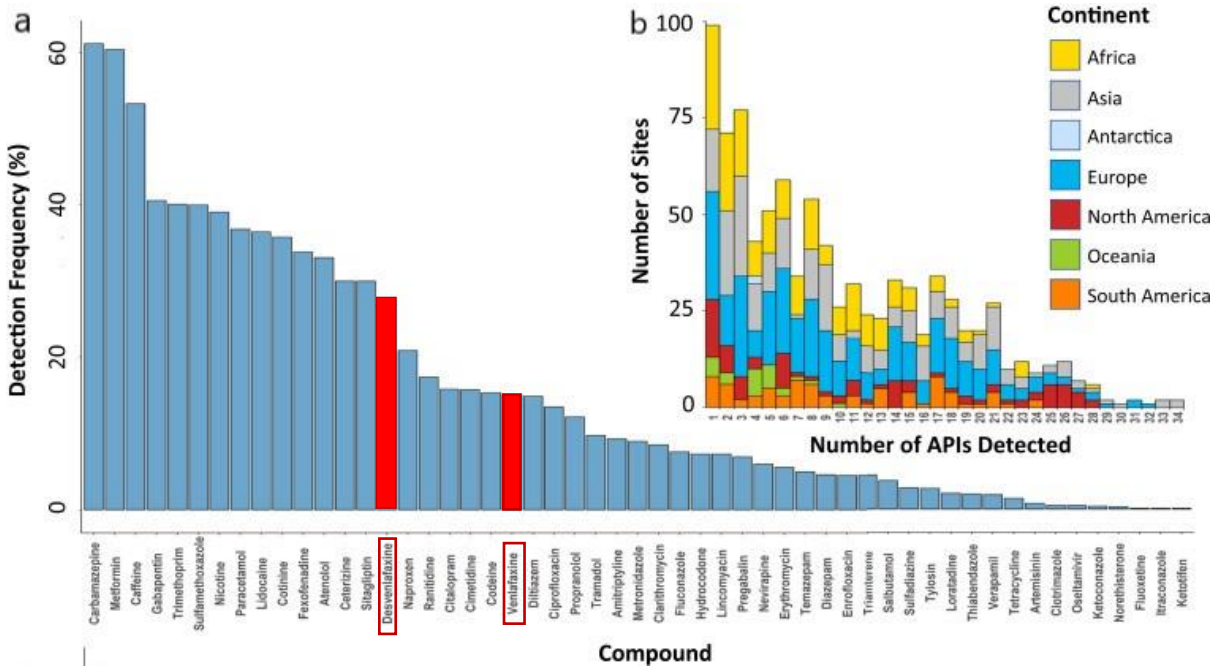


*Figure 2.1. (a) Frequency of detection of harmful concentrations of active pharmaceutical ingredients at sampling sites, and (b) number of active pharmaceutical ingredients detected at amount of sample sites [5].*

### 2.1.2 Background information on desvenlafaxine and venlafaxine

Both VF and DVF are used as anti-depressants to treat major depressive disorders and function as serotonin-norepinephrine reuptake inhibitors (SNRI). A SNRI inhibits the reabsorption of serotonin and norepinephrine on an axon after these compounds served their function as a neurotransmitter. These are

important for mood regulation. The reuptake is inhibited by blocking the action of transporters that regulate the concentrations of extracellular neurotransmitters. As these re-uptake transport proteins are blocked, the neurotransmitters will remain present at the synapse, and thus their overall concentration increases. In Table 2.1 an overview of the physical-chemical properties of venlafaxine and desvenlafaxine can be found.

*Table 2.1. An overview of the physical-chemical properties of venlafaxine* [3] *and desvenlafaxine* [4]*.*

| | **VF** | **DVF** |
|---|---|---|
| **IUPAC name** | 1-[2-(dimethylamino)-1-(4-methoxyphenyl) ethyl]cyclohexan-1-ol | 4-[2-(dimethylamino)-1-(1-hydroxy cyclohexyl) ethyl]phenol |
| **Molecular formula** | $C_{17}H_{27}NO_2$ | $C_{16}H_{25}NO_2$ |
| **Molecular weight** | 277.4 | 263.27 |
| **Solubility in water at 25 °C** | 267 mg/L | 3700 mg/L |
| **Dissociation constants (p$K_a$)** | 9.5 | 9.45 (amine)<br>10.66 (phenol) |

VF can be seen as the first structure of Figure 2.2a and is usually sold under the name Effexor. It is a well-absorbed chemical, a minimum of 92% of oral doses is absorbed. In the liver, it is metabolized into DVF and functions as the active metabolite. Up to 5% is secreted out via the kidneys as unchanged VF and 29% as DVF [27].

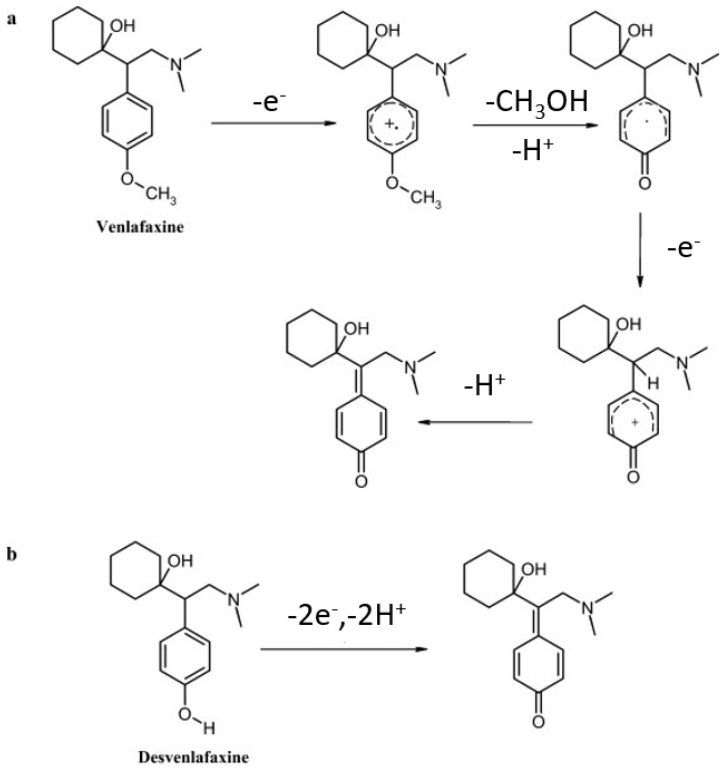


*Figure 2.2 Chemical structure and likely oxidation scheme of (a) venlafaxine and (b) desvenlafaxine [26].*

Synthetic DVF is usually sold under the name Pristiq, and its chemical structure can be seen in Figure 2.2b. In DVF a methoxy group is replaced by a hydroxy group, and this small change has a big impact on performance as DVF is the active metabolite. The effects of DVF and VF are similar, as most of the venlafaxine is metabolized into desvenlafaxine after intake. For DVF up to 45% is excreted unchanged out of the body. This leads to high concentrations of DVF and VF in wastewater [28] before they find their way into nature. In wastewater treatment plants only a mediocre degradation of DVF and VF takes place [29] and it is sensitive to environmental conditions (other pollutants, temperature, etc.) which can further inhibit remediation. Furthermore, barely any degradation of DVF and VF will take place after passing through treatment plants**,** thus they end up as pollutants [30]. Other methods, such as adsorption using clay or the introduction of reactants appear to have minimal effect on the degradation of DVF and VF [31, 32].

DVF and VF present in wastewater end up in nature and will have an adverse effect on the health of aquatic life. The behavior of aquatic invertebrates and vertebrates is affected, negatively influencing their reproduction and survival [6]. Therefore, in 2020, the European Union considered DVF and VF suitable for inclusion in the Surface water Watch List (WL) under the European Union Water Framework Directive [7]. The list contains monitoring data on emerging pollutants that pose a potentially significant risk to the aquatic environment without adequate data to conclude.

### 2.1.3 Electrochemical sensing of desvenlafaxine and venlafaxine

There has only been a limited number of studies on the sensing of DVF using (carbon-based) electrochemical sensors and these are typically combined with VF sensing. However, VF detection using (carbon-based) electrodes is more widely reported. In Table 2.2, an overview of several different studies with the found analytical parameters of DVF and VF is provided.

A common sensing technique is differential pulse voltammetry (DPV), whilst the pH and electrolyte vary from one study to another. Also, all previously used electrodes are modified, a bare non-modified electrode has not yet been investigated. Overall, Table 2.2 gives a good starting point for establishing the sensing method when BDD electrodes are to be used. For practical applications the following information has to be taken in to account. The recommended levels of DVF in blood plasma are between 0.4 µM and 1.5 µM and concentrations higher than 2.28 µM are cause for alarm. For VF, recommended levels are between 0.35 µM and 1.45 µM, whereas a concentration above 2.26 µM is considered dangerous [33]. The concentrations found in hospital wastewater are significantly lower, 0.6 nM for VF and 2.5 nM for DVF [34].

In conclusion, the presence of DVF and VF in our environment is of concern for aquatic organisms and human health. Proper monitoring and eventual degradation of DVF and VF in wastewater and rivers should be of paramount interest. Also, the common use of DVF and VF as antidepressants makes the fast determination of sample concentrations in the medical field interesting. The current state-of-the-art of electrochemical sensing of DVF and VF uses carbon nanotubes; this makes BDD with its superior properties an electrode of promise for the development of improved sensor with desirable performance.

*Table 2.2. An overview of reported carbon-based electrodes for the detection of desvenlafaxine and venlafaxine partially reproduced from Tran et al.* [35] *and expanded.*

| Electrode | Electrolyte | pH | Linear range (μM) | LOD (μM) | Sensing technique | Samples analyzed | Ref. |
|---|---|---|---|---|---|---|---|
| **Desvenlafaxine** | | | | | | | |
| NAF/CNT/ GCE | 0.1 M acetate buffer | 5.0 | 0.053 - 35.8 | 0.0211 | AdS-DPV | pharmaceutical formulations, urine, and blood serum | [26] |
| MWCNT/ ZnONPs/ CPE | 0.04 M BRB | 9.0 | 1.7 – 21.1 | 0.7 | CV, DPV | pharmaceutical formulation, combined dosage form, and urine | [36] |
| C/SWCNTs/ MIP-ODV | 10 mM phosphate buffer | 6.0 | 5.0 – n.d. | 2.0 | CC, EIS | pharmaceutical formulation, and urine | [37] |
| **Venlafaxine** | | | | | | | |
| $Eu^{3+}$ doped/NiO/CPE | 0.1 M PBS | 7.0 | 0.04-300 | 0.01 | CV, DPV | pharmaceutical formulation, urine, and synthetic serum | [38] |
| MWCNTs/ CILE/CPE | 0.1 M phosphate buffer | 9.0 | 10.0 -500 | 0.47 | CV | pharmaceutical formulations, urine, and blood serum | [39] |
| Co–Pd $Al_2O_3$/GCE | BRB | 7.0 | 0.00195 – 0.5 | n.d. | SWASV, CV | pharmaceutical formulations, synthetic serum | [40] |
| NAF/CNT/ GCE | 0.05 M BRB | 7.0 | 0.0038 –62.2 | 0.00124 | AdS-DPV | pharmaceutical formulation, urine, and blood serum | [26] |
| VFMNPs/ CPE | BRB | 7.0 | 0.01-10 | 0.006 | EIS, CV, DPV | pharmaceutical formulation, urine, and blood serum | [41] |
| NiCo-MOF/SPGE | 0.1 M PBS | 7.0 | - | - | CV, DPV | pharmaceutical formulation, urine, and tap water | [42] |
| MWCNT/ RTIL | 0.1 M phosphate buffer | 6.8 | 2.0 –2000 | 1.69 | SWV | pharmaceutical formulations | [43] |
| $NiCo_2O_4$/ rGO | BRB | 10.5 | 0.005-0.5 | 0.0034 | CV, EIS, SWV | pharmaceutical formulation and human plasma | [44] |

*The following abbreviations are used in the table: NAF, Nafion. MW/SW CNT, multi-walled/ single-walled carbon nanotubes. GCE, glassy carbon electrode. AdS-DPV, adsorptive stripping differential pulse voltammetry. ZnONPs, zinc oxide nanoparticles. CPE, carbon paste electrode. BRB, Britton-Robinson buffer. CV, cyclic voltammetry. SWASV, Square wave anodic stripping voltammetry. MIP-ODV, molecular imprinted polymer-desvenlafaxine. CC, chronocoulometric. EIS, electrochemical impedance spectroscopy. VENMNP, venlafaxine imprinted polymer coated silica-coated magnetite nanoparticles. CILE, carbon ionic liquid electrode. MOF/SPGE, metal organic framework/screen printed graphite electrode. RTIL, room-temperature ionic liquid. rGO, reduced graphene oxide. n.d. for not determined.*

## 2.2 Synthetic diamond

This chapter begins with a background on diamonds and follows with the most widely applied techniques used to synthesize diamonds. Three techniques are considered, these are detonation synthesis, high-pressure-high-temperature synthesis, and chemical vapor deposition (CVD). CVD is considered in-depth as it is most relevant for the focus of this project. A brief overview of diamond patterning methods is given in the final section.

### 2.2.1 Diamond lattice and material properties

Diamond and graphite are both allotropes of carbon. Their difference lies in the structure of the carbon atoms inside the unit cell. Diamond consists of so-called $sp^3$ hybridized carbon atoms, this allows for bonding to four neighboring atoms. This arrangement creates a cubic system (space group fd3m) wherein tetrahedral bonds are made between equally spaced atoms. These bonds have an angle of 109° 28′ and form an extremely strong covalent bonding network [8, 9]. This leads to diamonds having desirable material properties such as extreme hardness, high electrical resistance, low thermal expansion coefficient, high chemical inertness, low fouling, and wide optical transparency. Furthermore, diamond has a wide range of variables that can influence material properties, such as grain size, graphite content, and even doping with boron or nitrogen. An overview of the principal properties of diamond can be found in Table 2.3

*Table 2.3. Principal properties of diamond* [45]

| **Property** | |
|---|---|
| Hardness | 10000 kg/mm$^2$ |
| Tensile strength | >1.2 GPa |
| Compressive strength | >110 GPa |
| Young's modulus | 1.22 TPa |
| Density | 3.52 g/cm$^3$ |
| Thermal conductivity | 20.0 W/cm K |
| Bandgap | 5.45 eV |
| Resistivity | $10^{13}$-$10^{16}$ ohm cm |

These properties make diamond a material of interest in a wide variety of fields. As natural diamond is expensive, has a bulky shape and there is no control over its contaminants, its practical use is limited. Therefore, several methods to synthesize diamond in a lab environment have been developed. Figure 2.3 illustrates how diamond is thermodynamically stable under high-temperature and high-pressure conditions. Several of the synthesis techniques are in this region, such as HPHT and detonation synthesis (marked as shock wave synthesis in the diagram). It is common knowledge that diamond also exists at atmospheric conditions, yet in the phase diagram graphite is the more thermodynamically stable form of carbon. The transformation from diamond to graphite is inhibited by the large amount of energy required to convert between phases because of the strong covalent bonds. This is known as metastability and is employed in CVD to create diamonds without high pressure.

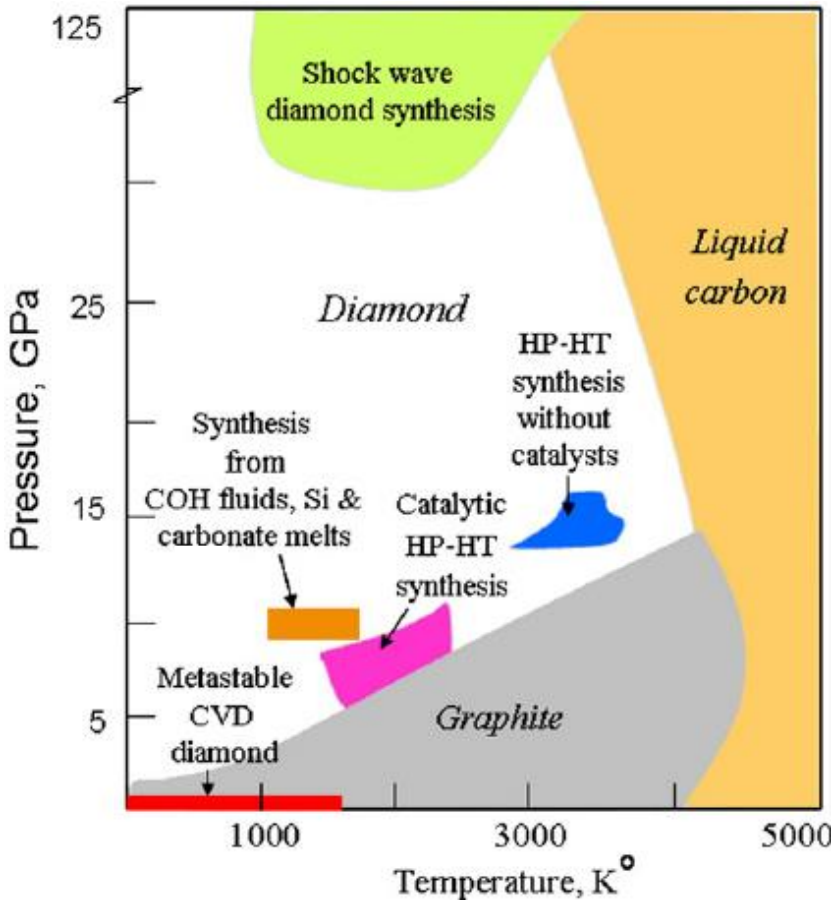


*Figure 2.3 The phase diagram of elemental carbon with various diamond synthesis methods indicated* [8].

### 2.2.2 Growth of synthetic diamond

Chemical vapor deposition (CVD) was developed with a desire to reduce the pressure at which synthesis takes place. In CVD a heated chamber under a vacuum is utilized to deposit films on a substrate. For diamonds, a carbon-containing gas, usually methane, is pumped into the CVD chamber and is decomposed into radical carbon molecules which interact with (a combination of deposition and desorption) the substrate. This process is not driven by thermodynamics but by kinetics. Consequently, the reaction can form diamonds when it is not thermodynamically stable according to the phase diagram. When these diamond structures are formed, they will stay as diamonds due to the previously discussed metastability. The diamond formation process can be divided into three steps:

1. Diamond nucleation
2. Growth of diamond aggregates
3. Growth of the diamond layer

#### *2.2.2.1 Chemistry of CVD*

The key aspect of the diamond formation process is hydrogen gas. The carbon precursor is diluted with hydrogen gas and together they form the reactants. These reactants enter the CVD chamber and are activated, this process decomposes $H_2$ into atomic hydrogen. This atomic hydrogen is a critical component of several main processes [46]:

I. The atomic hydrogen radicals react with the carbon precursor gas to form reactive carbon radicals. These carbon radicals react with the nucleation layer consisting of diamond nanoparticles to form the diamond film.

II. Dangling bonds are present at the surface of the diamond bulk. These bonds must be terminated to prevent cross-linkage, which would lead the surface to restructure to graphite. Either hydrogen or OH is used to terminate these bonds and thus stabilize the diamond. However, for diamond growth, the dangling bonds need to react with carbon-containing species.

III. The excess atomic hydrogen radicals can react with the surface hydrogen to create a dangling bond thereby establishing a reaction cycle until the bond reacts with a carbon-containing species.

IV. Many different $C_xH_y$ compounds can be formed when carbon-containing radicals react with each other. Hydrogen atoms are efficient in cracking these hydrocarbons and thus ensure that no polymers or other long carbon chains can be formed which would limit the diamond growth. An overview of such reactions taking place between methane and hydrogen in the gas phase of a CVD process can be seen in Figure .4. It is generally accepted that the $CH_3$ radical contributes the most to the growth of diamond.

V. During the growth process, graphite is formed on the surface as well according to the Ostwald-Vollmer law [47] due to graphite's lower density. These graphite layers etch much faster with atomic hydrogen than diamond does. The hydrogen thus "cleans" the surface by removing unwanted graphite.

Besides the requirement of a significant amount of hydrogen, there are several other CVD parameters that are important and some of which can be adjusted slightly. These are the carbon-to-hydrogen ratio (99.5%-87% $H_2$), the system pressure (5-100 mbar), and substrate temperature (700 °C - 1000 °C) [48]. The carbon-to-hydrogen ratio influences the growth rate. More carbon leads to faster growth but also increased graphite content. Lower pressure can promote the formation of atomic hydrogen. A substrate temperature of 800 °C is considered optimal, above 1000 °C graphite forms, and below 600 °C diamond growth is hampered.

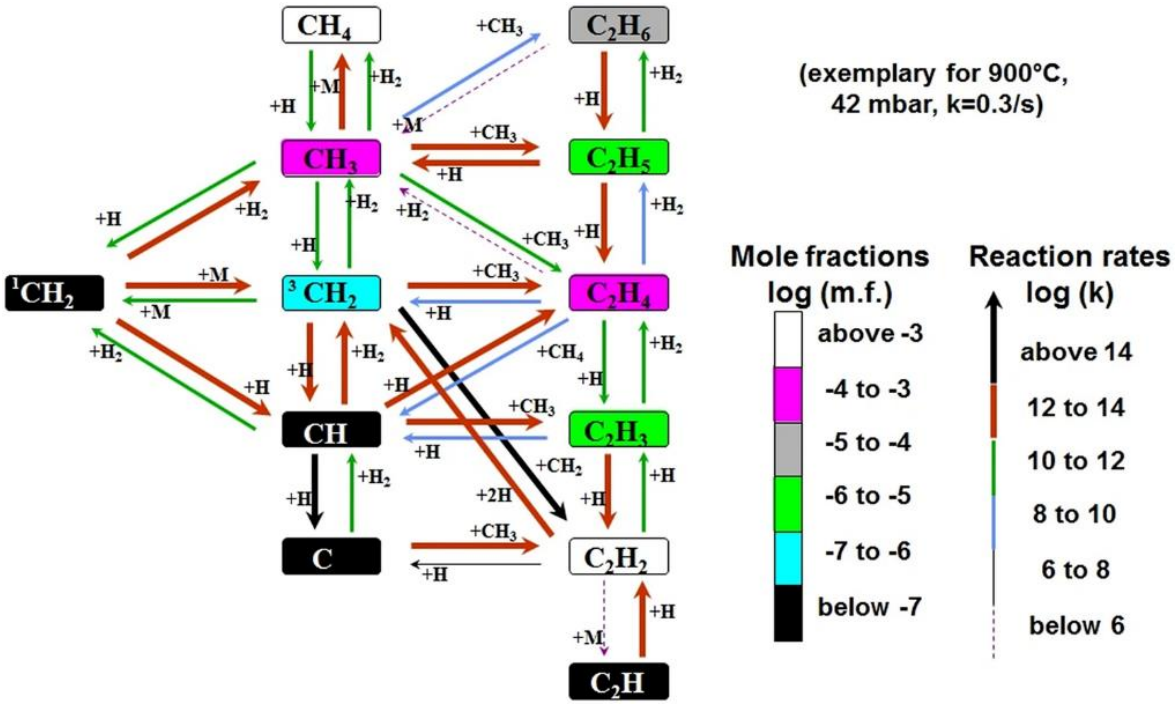


*Figure 2.4. The gas-phase reactions of the reactants (methane and hydrogen) in the diamond CVD chamber. The arrows show which molecules are reacting with each other. [47]*

A crucial factor in the growth of diamond is nucleation. Control over it is essential for optimizing the grain size, grain orientation, optical transparency, adhesion, and surface roughness of as-grown films. Nucleation is the generation of small diamond nuclei and clusters at the substrate surface. A low nucleation density can have adverse effects on the quality of the diamond grown. For instance, a lower nucleation density leads to a thicker film before the entire surface is covered and no pinholes to the substrate are present, as diamond growth happens in all directions equally from a nucleation point [3]. Low nucleation density can also lead to the presence of voids. When film coalescence is achieved, diamond growth no longer takes place beneath the film and thus any voids persist. This has a negative effect on the adhesion between diamond and substrate, also thermal transfer is diminished. Nevertheless, voids can have desired effects as well, as they can accommodate strain and thermal expansion.

#### *2.2.2.2 Diamond material types*

Diamond can be further characterized by its crystal structure. There are two main categories; single crystalline diamond (SCD) and polycrystalline diamond (PCD). SCD consists of a singular continuous crystal that extends unbroken between all edges as can be seen in Figure .5. SCD can be grown by two different methods, homoepitaxy, and heteroepitaxy. Homoepitaxial films are grown on existing high-quality polished SCD substrates, whereas heteroepitaxial films are grown on a non-diamond substrate. Iridium has been found to allow for the highest crystalline quality. However, silicon wafers are popular due to their availability. In general, homoepitaxial films are of better quality than heteroepitaxial films. However, heteroepitaxial films can be grown at a much larger size. Although both homo- and heteroepitaxial films have their own fields of application, they overlap each other's fields significantly [49].

PCD consists of multiple crystals or grains of diamond, where each has its own size, orientation, and structure. The creation of this polycrystalline structure begins during the initial stage of diamond growth. The film is still non-continuous and consists of isolated growth locations. These growths expand, meet one another and coalesce into the diamond film as time progresses [9]. These growths form the crystals of the PCD structure and at the locations where the individual growths intersect, the grain boundaries are formed. At these grain boundaries, $sp^2$ carbon and hydrogen are present. The grain boundary volume is thus related to the purity of the diamond film. Grain size is directly related to the number of grain boundaries, therefore four divisions in microstructure are made: micro-crystalline (MCD, >1 µm) diamond, sub-micro crystalline diamond (200-1000 nm), nano-crystalline diamond (NCD, 10-200 nm) and ultra-nano-crystalline diamond (UNCD, < 10 nm) [9]. Figure 2.5b-c shows SEM images of these types of diamonds.

For the growth of micro- or sub-micro crystalline diamonds initial nucleation density is low ($<10^{10}/cm^2$). The grains exhibit a clear column structure as they grow. This leads to the diamond coarsening as it thickens and the root mean square (RMS) roughness value is typically ~10% of the film [50, 51]. For most applications post-treatment is required to decrease the roughness. A high hydrogen environment (~ 99%) and low methane content are essential for the growth of MCD, as this limits the secondary nucleation rates (the formation of new grains/crystals on existing ones). For systems with a higher methane content (>3-5%) secondary nucleation is encouraged. NCD combines this with a higher initial nucleation density ($>10^{12}$ / $cm^2$) to achieve its smaller grain size. NCD has a lower surface roughness, but a higher $sp^2$ percentage than MCD or sub-micro crystalline diamond. The growth of UNCD diamond differs from MCD, sub-micro crystalline diamond, and NCD in the use of an argon-rich environment instead of a hydrogen-rich environment. The high argon concentration induces a large amount of re-nucleation and the formation of a large number of small grains. Compared to MCD and NCD diamond, UNCD has a significantly larger amount of $sp^2$ carbon as grain boundaries make up 10% of the total volume. The larger amount of $sp^2$ and smaller grain size influences the properties of the diamond film. It was found by Cheng et al. [52] that: UNCD has lower thermal conductivity, stiffness, and hardness. In contrast, the minimal thickness of the film is dependent on grain size, thus small grain sizes allow for the creation of thinner films. Moreover, for UNCD the grain size no longer determines the surface roughness and allows for the creation of smoother films [51, 53].

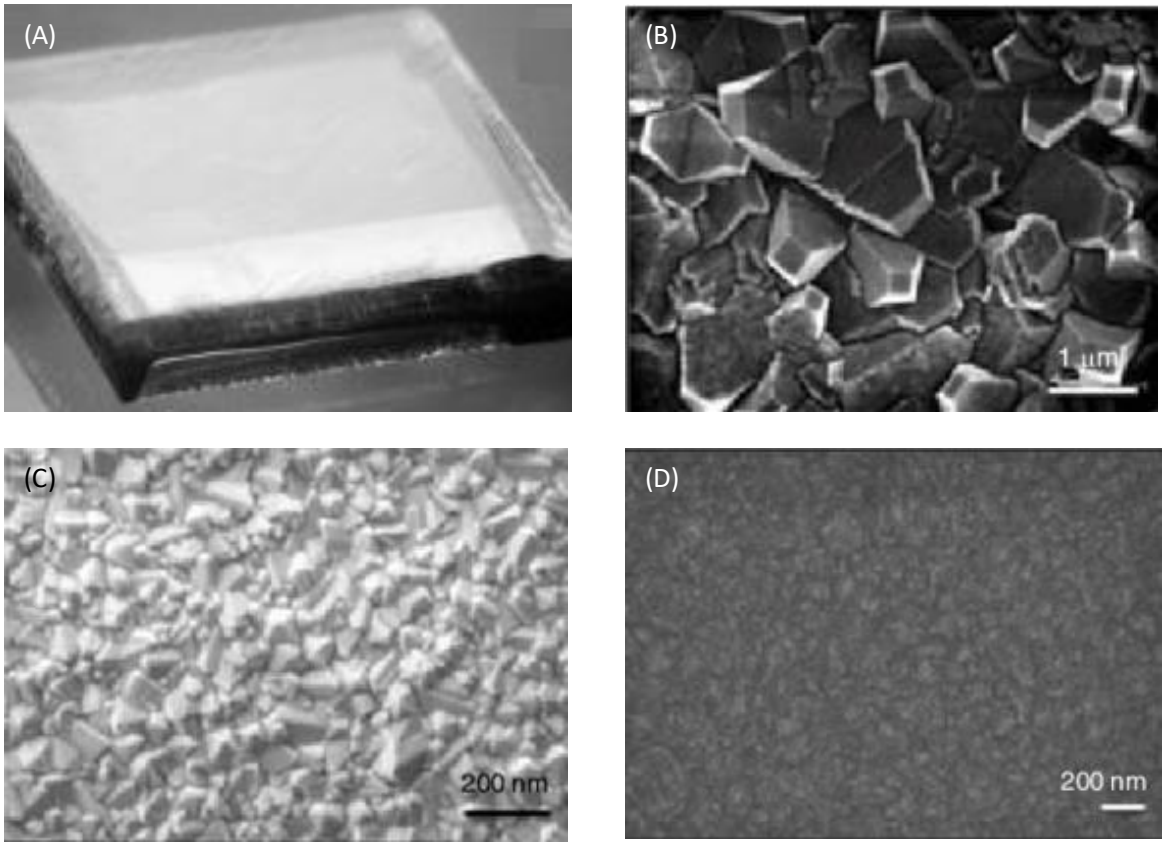


*Figure 2.5. SEM images of different diamond material types, (A) CVD grown single crystalline diamond (2.5 × 2.5× 0.3 mm)* [54]*, (B) microcrystalline diamond* [50]*, (C) nanocrystalline diamond* [50]*, and (D) ultra-nanocrystalline diamond* [50].

#### *2.2.2.3 Growth of synthetic diamond.*

Microwave CVD (MWCVD) is a form of plasma-enhanced CVD (PECVD) and is the most commonly used deposition technique. Other, less popular methods to generate plasma are radio-frequency (RF), direct current (DC), and arc plasma jet [9, 46, 48], and are not discussed in depth here. All have in common that hot plasma is generated inside a reaction chamber of stainless steel or a tube of quartz glass. For MWCVD, microwaves (~2.45 GHz) are guided into the chamber using a waveguide. A ball-shaped plasma, confined to the center of the chamber and touching the substrate, is formed. This plasma generates atomic hydrogen and allows for the creation of radical hydrocarbons similar to the filament in HFCVD. The generated atomic hydrogen has high kinetic energy and the collisions between the molecules in the chamber lead to a high ionization rate.

### 2.2.3 Doped diamond

In this work, diamond-based electrochemical sensors are of interest. Applications of undoped diamond are more limited as diamond itself cannot transfer electrical signals. Thus, its (passive) use is mainly limited to mechanical resonators or transparent coatings. This can be changed by doping diamond with another material during the growth process, modifying the electric or optical properties [9, 55, 56]. Currently known doping elements are boron, nitrogen, phosphorus, sulfur, and arsenic.

Boron-doped diamond (BDD) is created by adding diborane or trimethyl borane among the reactant gases in CVD. BDD is widely used in electrochemistry, as it has low background and capacitive currents, a wide

solvent window, and all the advantages of undoped synthetic diamond. The amount of doping influences the electrical conductivity: at low doping levels (≤ $10^{19}$ atoms/$cm^3$), BDD functions as a semiconductor, whilst at high doping levels (≥ $10^{20}$ atoms/$cm^3$) it acts as a semi-metal with high conductivity. For highly doped BDD, the resistivity can range between $10^{-3}$ and $10^{-1}$ Ωcm. This can be modified by altering the boron concentration.

To manufacture p- and n-type conductive diamond coatings, boron and nitrogen/phosphorus are used, respectively. However, the equilibrium solubility of nitrogen dopants in bulk diamond is often incredibly low. Nevertheless, doping of nitrogen also allows for the creation of nitrogen-vacancy (NV) centers, which have become popular for optical applications and quantum computing, among others. NV pairs are created by replacing two carbon atoms in the lattice with a nitrogen atom and a vacant atom. The NV centers can have certain charge states ($NV^-$, $NV^0$, and $NV^+$) that depend on electron orbit and create color centers. Different luminescence can be achieved, depending on the concentration and number of each charge state [57]. Phosphorus has been used successfully to produce n-type diamond [56]. Phosphorus-doped diamond (PDD) is less investigated than BDD and typically much lower conductivity is reached.

Another method in which BDD films can be modified is in the chemical groups (CO,O,H) present at the surface of the film, this is known as surface termination. The first of which is hydrogen-terminated (or H-BDD) surface [58]. As-grown BDD films are hydrogen-terminated as growth is conducted in a hydrogen rich environment. Hydrogenated surfaces have general hydrophobic properties and can also be achieved by hydrogen plasma treatment or cathodic pretreatment. When a large number of oxygen groups (e.g., C-OH, C-O-C, and C=O) are present an oxygen-terminated (O-BDD) surface is created. The electrons in these groups are more attracted to the carbonaceous atoms of the BDD surface, which results in a partially negative charge of the oxygen atoms. The following techniques can be used to create oxygen terminated surfaces: wet-chemical etching, dry-chemical oxidation, mechanical treatment, and anodic pre-treatment. Oxygen-enriched surfaces are overall more stable, while hydrogen-enriched surfaces oxidize over time.

## 2.3 BDD-based electrochemical sensors

One of the most prominent uses of BDD is the development of electrochemical sensors; this application therefore deserves a more in-depth look. To understand why BDD is an excellent electrode material an understanding of electroanalytical, particularly voltammetric, techniques is required.

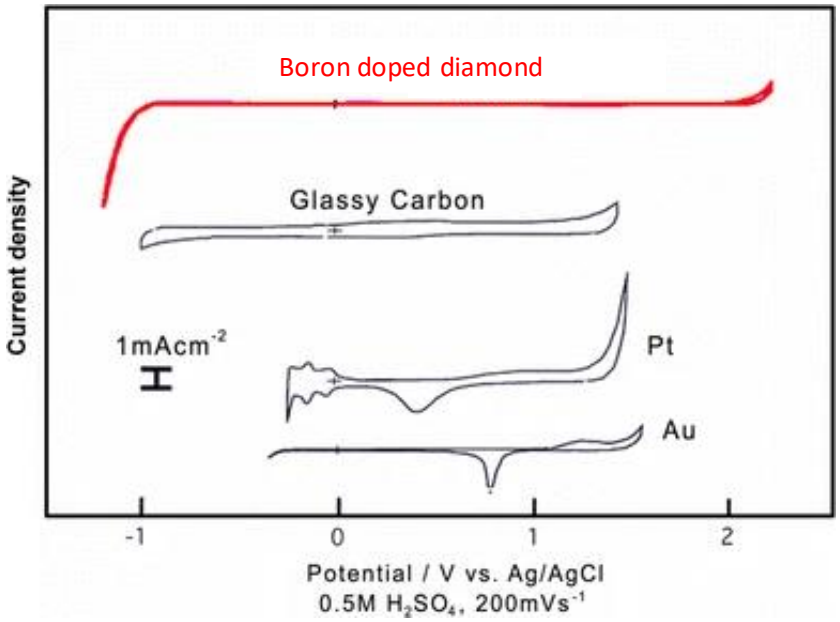


*Figure 2.6. The potential windows of several electrode materials, BDD included as 'diamond' (in red) [59].*

In electrochemical sensors, a set of electrodes is employed as the main component. For the sensor to work, two electrodes are required – the working electrode (WE) and the counter/auxiliary electrode (CE/AE). The sensing process takes place at the WE, which simultaneously controls the magnitude of the current generated due to the oxidation or reduction of the electroactive compound. The AE enables current flowing and its surface area is typically significantly larger than that of the WE. Often a third electrode is added to create a three-electrode cell – the reference electrode (RE). The RE has a known and fixed potential and no current may flow through the RE as this would alter this potential. The potential placed on the WE is determined by the RE by measuring the voltage between them. By varying the voltage over the WE and measuring the current, oxidation and reduction peaks can be found as electrons move between the WE and the electroactive analyte solution.

Every electrode material has its potential range and analytes must be oxidizable and/or reducible inside this range for detection to be possible. The potential window of BDD can be seen in Figure 2.6 (in red color) and is compared to several other common electrode materials. The electrochemical window of the BDD is the largest and thus offers a superior application range for possible analytes. Besides the potential windows, the background currents of various electrode materials can be seen as well. The magnitude of the background current is one of the limiting factors in an electrode's sensitivity, as it can mask the signal of the analyte, and thus increase the limit of detection (LOD). BDD has an exceptionally low background current and often provides an remarkable signal-to-noise ratio.

Additionally, BDD shows a large resistance to (bio)fouling and is chemically inert. This is in contrast to metallic or $sp^2$ carbon-based electrodes which often have a problem with adsorption and fouling effects

that increase the contamination on the electrode surface and negatively affect the repeatability of the measurements [60]. Besides, such fouling significantly increases the background current and thus lowers signal-to-noise ratios and sensitivity. When the superior electrochemical behavior of BDD is combined with diamond's robust physical characteristics an attractive alternative to traditional electrodes is formed.

Interesting feature of the BDD is that its surface termination can be modified by anodic or cathodic pretreatment, which lead to the preparation of oxygen enriched (O-BDD) or hydrogen-terminated (H-BDD) electrodes, respectively. Naturally, this influences the electrochemical characteristics and performance of the BDD electrodes [61]. Figure 2.7b shows the difference in results between hydrogen-terminated (green) and oxygen-enriched (orange) surfaces for ferrocyanide $[Fe(CN)_6]^{3-/4-}$. $[Fe(CN)_6]^{3-/4-}$ redox reactions are an inner-sphere processes and therefore largely dependent on the surface characteristics. The O-BDD surface is partially negatively charged and will thus interfere with the reaction; electrostatic repulsion of anionic $[Fe(CN)_6]^{3-/4-}$ is expected [62]. This results in increased peak-to-peak separation, and can be used as an indicator for the surface characteristics. Figure 2.7a displays the results for BDD electrodes with various levels of boron doping and the effect they have on the redox reaction of $[Ru(NH_3)_6]^{3+/2+}$. This redox reaction is of outer-sphere nature, and is thus independent of the surface termination and other BDD's surface characteristics. However, $[Ru(NH_3)_6]^{3+/2+}$ is sensitive towards density of states and can be used as a suitable indicator for boron doping levels, and thus conductivity. The lower boron doping will lead to poorer conductivity, which makes the electron transfer more difficult; this is then manifested by an increase in the peak-to-peak separation of oxidation and reduction peaks.

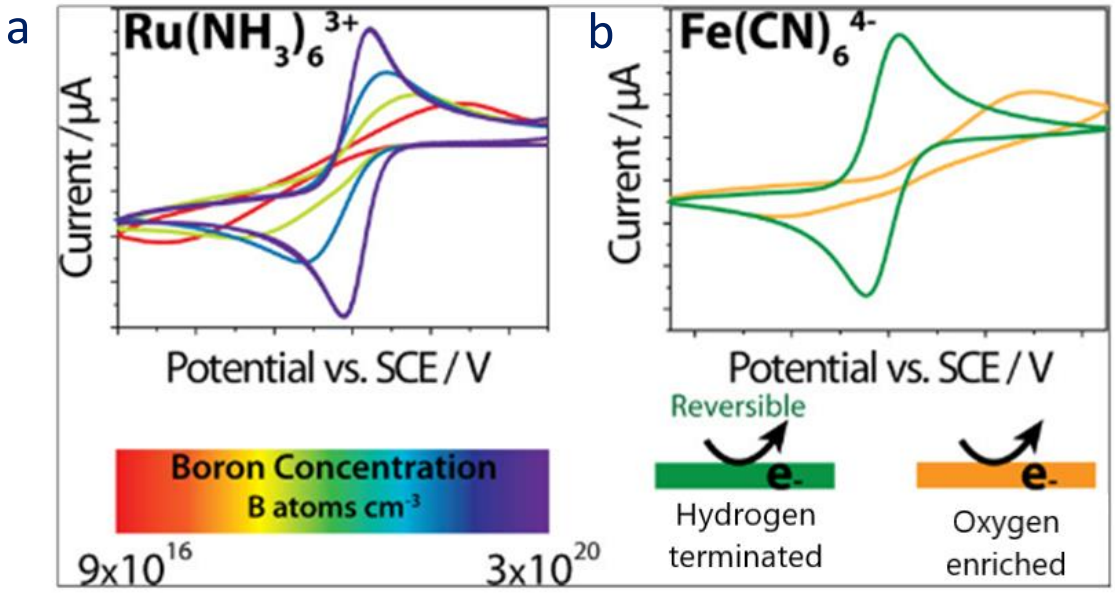


*Figure 2.7. Cyclic voltammetry results obtained for, a) $Ru(NH_3)_6^{3+}$ on BDD electrodes with different boron concentrations, and b) $Fe(CN)_6^{4-}$ on either hydrogen-terminated or oxygen-enriched BDD surfaces [63].*

Moreover, the electrochemical characteristics of BDD electrodes can be further fine-tuned by the $sp^3/sp^2$ carbon ratio. Graphite ($sp^2$) is typically found at the ground boundaries due to defects during growth. On one hand, it can act as a charge transfer mediator between the BDD and redox couples and can thus accelerate electrode reactions [64]. On the other hand, BDD electrodes with high $sp^2$ content act more like graphite electrodes and have deteriorated electrochemical behavior, often manifested by higher

background currents and a smaller potential window [65]. These consequences make the use of $sp^2$ in BDD electrochemistry a controversial topic.

## 2.4 Patterning of diamond

For the use of diamond in applications a patterning step must take place. In this step, the desired shape is given to the grown diamond film as it usually covers the entire substrate wafer. This is done with a top-down method such as dry etching or cutting. For cutting, a laser is usually used to remove unwanted parts of the bulk. For etching, a mask with the desired pattern is created and placed on the bulk. An etching method is chosen (e.g., deep reactive ion or plasma etching) which can achieve the desired effects. The mask protects the selected parts of the bulk whilst other parts are selectively removed. Both these methods create waste and subject the diamond film to another processing step. This can be avoided by using bottom-up patterning.

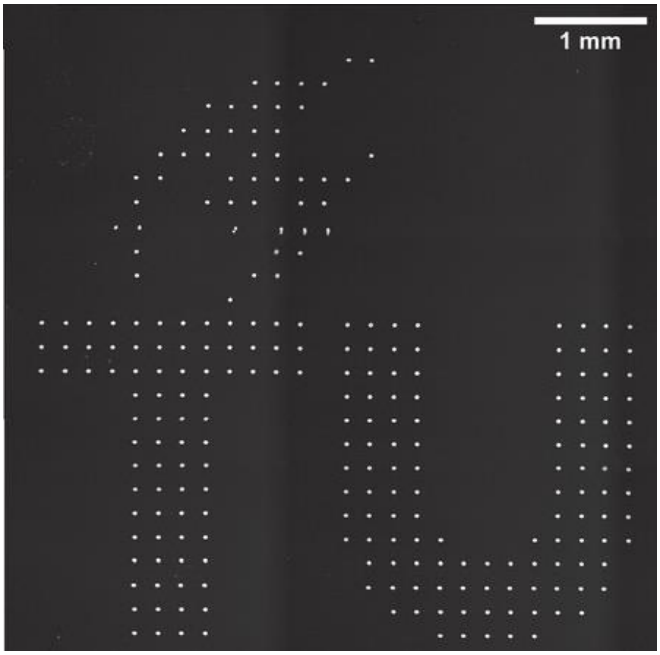


*Figure 2.8. SEM image of an array of nanocrystalline diamond disks produced on a Si substrate* [66].

In bottom-up approaches, only the desired pattern of the diamond film is grown. This is achieved during the seeding process, wherein only the pattern is seeded. One method to pattern CVD diamond films is by making use of a mask. The mask may be printed onto the substrate (e.g., by two-photon polymerization of photosensitive resin) and acts as a negative of the desired pattern. Seeding takes place and seeds are deposited on both the mask and substrate. By removing the mask, a seed pattern is left behind on the substrate. This pattern can then be grown to create the desired diamond film shape. Alternatively, a porous mask may be applied as the growth template during the diamond growth to produce micro-pillar arrays [67].

A second method to fabricate diamond structures utilizes screen printing. This technique is used for the manufacture of electrodes and the method has been developed by the group of Kondo [68–73]. Diamond powder (<500 nm) was coated with a layer of BDD using MWCVD and post-treated to remove impurities. This boron-doped-diamond powder (BDDP) was mixed with polyester (Vylon GK-140) resin in solvents (2-butanone and isophorone) to create a BDDP-ink paste. This was used in a screen printer to print an electrode with a diameter of 6 mm. All current screen-printing methods have a major downside in common: the use of toxic solvents. The method of Kondo and Matsunaga has this as well, a potential future solution is non-toxic aqueous solvents [74]. The elimination of toxic solvents would make this a viable method for large-scale manufacturing of diamond electrodes and microelectronics in general.

Another method to achieve this was investigated at TU Delft by Sartori et al. [66]. They used an inkjet printer with a diamond containing ink to selectively seed parts of a silicon substrate. This is a fully digital technique and requires no mask for each design. Figure 2.8 shows an all-diamond print pattern forming the letters “T” and “U” of the TU Delft logo. The letters were formed by nanocrystalline diamond disks

and in the figure appear as white circles. After the ink had evaporated, only the nanodiamond seeds were left behind and circular seed areas with a diameter of ~38 µm were created. These seed locations were used to create suspended NCD micro-disk resonators by growing the NCD on the Si substrate and then partially etching the silicon to suspend the disks. Further research by Liu et al. [14] has continued with this technique. By pretreating the surface the ink drops become connected and can be used to create a patterned structure. Figure 2.9 presents a schematic view of this method. The diamond ink would create a continuous path, and after the ink evaporates a pattern of nanodiamond seeds is left behind.

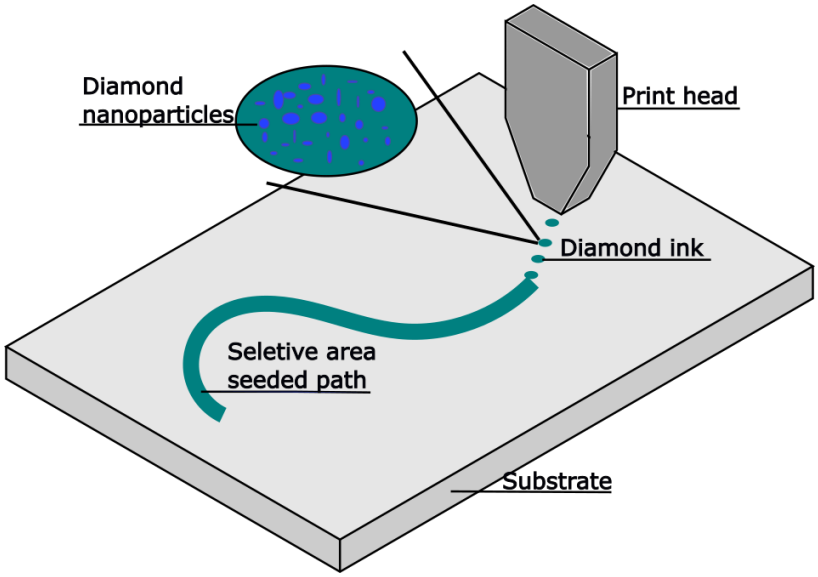


*Figure 2.9. A schematic overview of selective area seeding using inkjet printing.*

The feature size of this method depends on the printing resolution. A combination of minimum droplet size and droplet contact angle defines this resolution. This makes surface wettability and nozzle characteristics important criteria in inkjet printing. To evaluate ink printability the dimensionless Ohnesorge (Oh) number can be used. This number gives an evaluation of the relation between viscosity, surface tension, and internal forces. An Oh below 0.1 results in satellite droplets forming behind the main droplet, and an Oh above one results in the ink becoming too viscous. Also, the ink has to have sufficient energy for droplet formation and no splashing should take place when hitting the substrate [75]. Another aspect is the coffee-stain effect, a phenomenon that inks containing (diamond) nanoparticles suffer from. The deposition of the nanoparticles is influenced by the evaporation rate of the ink. Capillary flows are generated as the edges of the ink droplet evaporate; these push the nanoparticles from the center to the edge. Mitigation is required to ensure the proper distribution of the diamond nanoparticles [76].

# 3 Project proposal

In this chapter, the MSc thesis project is outlined. To start with, the goal of the thesis project is explained. Secondly, the main research question and sub-questions are presented.

## 3.1 Research objective

The main goal is to fabricate a three-electrode sensor for the reliable detection of DVF and VF. The sensor will comprise of BDD working and counter miniaturized electrodes, which will be manufactured by inkjet printing of diamond nanoparticles and subsequent CVD growth of thin-film BDD. In the literature, it was found that DVF and VF are electroactive and can be detected using carbon-based electrodes such as carbon paste [36, 41] or glassy carbon electrodes [26]. Therefore, it is of interest to investigate these compounds using BDD because it has superior electrode properties compared to other carbon-based materials. It must be evaluated if diamond ($sp^3$ carbon) is a viable carbon allotrope for the detection of DVF and VF and if a higher content of $sp^2$ carbon will allow for better detection parameters. The optimal supporting electrolyte (its composition and pH value) will have to be found in combination with the best voltammetric technique. Contaminants are often present in nature and thus their effects on DVF and VF detection should be investigated.

## 3.2 Research questions

**Main research question:** How can inkjet-printing manufactured boron-doped diamond be applied as a sensing material for the electrochemical detection of DVF and VF?

**Sub questions:**

1. Can DVF and VF be detected on as-produced non-modified boron-doped diamond (BDD)?
2. To what extent do the following BDD thin-film material properties affect the sensor performance?
    a. Type of surface termination (H-BDD vs. O-BDD).
    b. The relative content of $sp^2$ carbon.
3. What is the effect of interferents on the selectivity and sensitivity of the proposed BDD-based sensor?
4. How to manufacture miniaturized (feature size of millimeters) BDD electrodes using inkjet printing?
5. Which miniaturized electrode design is best suited for the detection of DVF and VF?

# 4 Methodology

In this chapter, the experimental methods, materials and setup are explained. The chapter is divided into two different parts: a section about the inkjet printing and a section about the electrochemical experiments.

## 4.1 Inkjet printing

### 4.1.1 Ink formulation

Two different ink types were prepared for the fabrication of the various electrodes, namely a nanodiamond ink for the WE and CE and a silver ink for the RE. To create a solution with 0.1 % (wt./vol) nanodiamond concentration, a 5.0 % (wt./vol) colloid (NanoCarbon Research Institute, Japan) was diluted by glycerol and deionized water (1:1 volume ratio). The method for nanodiamond ink preparation was investigated in previous work by our group [14]. Commercially available silver ink (25 wt.% Metalon JS-B25P, NovaCentrix) with 75 nm nanoparticles was purchased and used for the printing of the reference electrode.

### 4.1.2 Substrate and surface pretreatment

Silicon/silicon dioxide wafers (300 nm thermal $SiO_2$ dry/wet/dry layer, MicroChemicals, Germany) with a thickness of 525 ± 25 nm, a resistivity of $10^3$-$10^5$ Ω cm and a 4-inch diameter were used as printing substrates. The hydrophilicity of the substrates was increased by oxygen plasma treatment (12 seconds at 20 W with a Diener Femto plasma setup). The pretreatment allowed for homogeneous distribution of the nanodiamond ink to create an uninterrupted pattern, as the individual droplets coalesce.

### 4.1.3 Inkjet printing of electrodes

A PIXDRO LP-50 advanced research printer was used for printing of the nanodiamond and silver inks, an image of which can be seen in Figure 4.1. It utilizes piezoelectric nozzles and drop-on-demand technology to facilitate high control over the printing process. The printer has a precision of ±5 µm and an accuracy of ±15 µm. It contains a DMC printhead module wherein the ink cartridges are to be placed. For this project, new DMC-samba printhead cartridges were used for the printing of the nanodiamond ink. The cartridge has 12 square nozzles and ejects 2.4 pL droplets. An additional filter was used before filling the cartridge, this removes large particles and prevents clogging. The silver ink was prone to clogging the DMC-samba nozzles, therefore an older DMC-11610 printhead was used. The printhead has sixteen square nozzles and ejects 10 pL droplets, the larger droplet size reduces clogging chance. The printer prints a bi-directional pattern along the Y-axis, whilst the head was heated to a temperature of 29 °C.

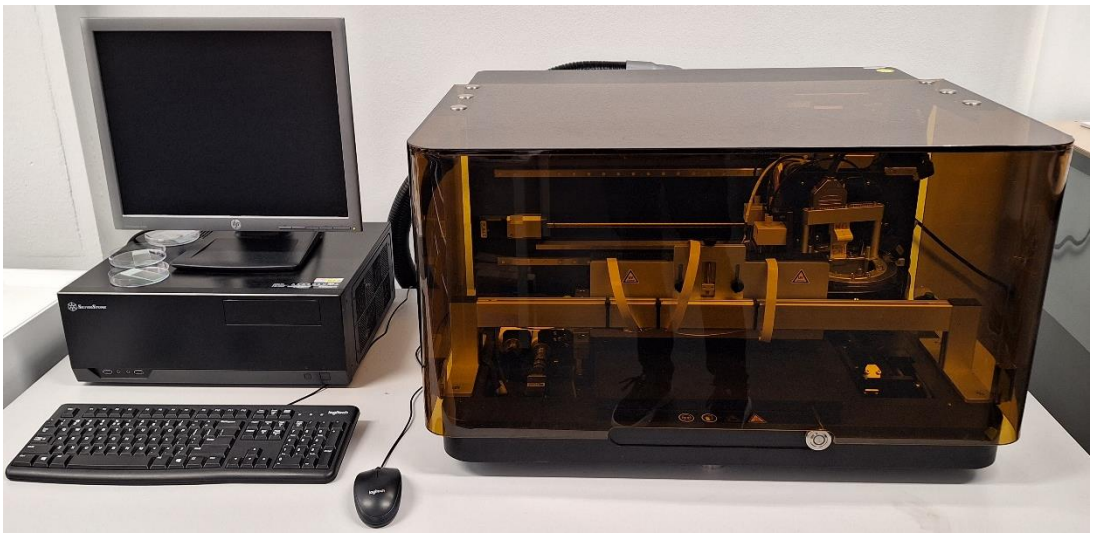

*Figure 4.1. The Pixdro LP-50 inkjet printing setup used for seeding the nanodiamond particles.*

### 4.1.4 Electrode print post-processing

After printing of the nanodiamond ink, the $Si/SiO_2$ wafers were placed in a vacuum oven for 1 h at 60 °C to evaporate all solvents and leave behind a nanodiamond-seeded pattern. A Binder VD23 vacuum oven, which can reach a minimum system pressure of 0.001 mbar, was used to further process the printed electrode patterns. Following, the wafers were ready for BDD growth (for the details of this growth process see section 4.1.5). After BDD growth, an Optec micro laser cutter was used to dice the wafers into individual sensor chips. The Optec is equipped with a 15 W Talon UV nanosecond laser. A diode current of 6 A was used in combination with 100 cut repetition to engrave lines, and thus weak points, into the wafer. The wafer was then placed on a slight elevation and carefully broken along the engraved lines.

After dicing of the wafer, a silver RE was printed on each sensor. The sensors with a silver RE were then placed on a hot plate for 5 min at 100 °C. This evaporates the ink solvents and leaves behind silver nanoparticles. The electrodes were placed in the vacuum oven for 1 h at 250 °C to sinter the silver [77]. This process improves adhesion of silver to the substrate. A vacuum oven was chosen to minimize the formation of silver oxides on the electrode, as this would interfere with the electrochemical measurements.

### 4.1.5 BDD growth

The growth of the BDD layer was carried out by the University of Hasselt (Hasselt, Belgium). An ASTeX 6500 series microwave plasma enhanced CVD reactor was used and a mixture of $CH_4$, $H_2$ and trimethyl boron was applied with gas flow rates of 5/395/100 sccm, respectively. As a result, a boron/carbon ratio of 20000 ppm (trimethyl boron was diluted to 1000 ppm in $H_2$) and 1 % $CH_4$ concentration were present in the reactor chamber. The BDD growth took place at the following deposition parameters: working pressure of 40 mbar, microwave power of 3500 W, growth time of 14 hours and a deposition temperature of >500 °C.

Additional BDD layer growth was performed at the Institute of Physics of the Czech Academy of Sciences (Prague, Czech Republic). An ASTeX 5010 (Seki Technotron, Japan) deposition system was used with the following conditions: 0.5% of methane in hydrogen, a gas pressure equal to 50 mbar, a microwave power

of 1150 W, a substrate temperature of 750 °C and a growth duration of 10 h. Boron doping was obtained by the addition of trimethylboron in the gas phase as a boron precursor for a B/C ratio of 4000 ppm.

## 4.2 Electrochemistry

### 4.2.1 Reagents and solutions

Both VF and DVF were acquired from Sigma-Aldrich. They were obtained in the form of venlafaxine hydrochloride ($C_{17}H_{27}NO_2$▪HCl) and desvenlafaxine hydrochloride ($C_{16}H_{25}NO_2$▪HCl) and are of analytical reagent grade. For the experiments, a stock solution of 1 mM dissolved in a mixture of deionized water (15 MΩ cm, IQ 7003) and isopropanol (IPA) (1:1) was created. This solution was then diluted in the selected electrolyte to the desired concentration. Both solutions were stored in the dark, VF at room temperature and DVF in the fridge at 4 ± 1 °C. The following chemicals, used for the preparation of supporting electrolyes, were acquired from Sigma-Aldrich as well: sulfuric acid (97%), sodium hydroxide, potassium nitrate and phosphate buffered saline (tablets, pH 7.4). All electrolytes were prepared in purified water to create solutions of 0.1 M sulfuric acid, 0.1 M sodium hydroxide and 0.5 M potassium nitrate with pH values of 0.7, 13 and 5.9. Furthermore, universal Britton -Robinson buffers (BRB) were made with pH ranging from 2.0 to 12.0. These were prepared by mixing an acidic solution of ortho-phosphoric acid (85%), acetic acid and boric acid (all acquired from Sigma Aldrich) and mixing it with 0.2 M sodium hydroxide to reach the desired pH value. The pH value was measured by a Metrohm 913 pH meter, laboratory version. Similarly, both redox couples were obtained from Sigma-Aldrich, in the forms of potassium hexacyanoferrate(II) trihydrate (≥99%) and hexaammineruthenium(II) chloride (98%). They were dissolved in a potassium nitrate (0.5 M) to a 1 mM solution and used for electrochemical characterization of the electrodes.

The following chemicals are all of analytical grade and acquired from Sigma-Aldrich to be used in the interference study of the compounds VF and DVF (see section 4.2.3). The interfering compounds of glucose, ascorbic acid, uric acid, sucrose and dopamine were dissolved to their desired concentrations in the selected electrolytes. A synthetic urine matrix was created based on the procedure proposed by Dbira et al. [78], 3.3 g/L Urea (55 mM), 0.05 g/L uric acid (300 µM), 0.166 g/L creatine (1.3 mM), 0.166 g/L $NaHCO_3$ (2 mM) and 0.025 g/L $Na_2HPO_4$ (180 µM). 250 mL of river water was procured from de Schie in Delft as well. Additionally, a synthetic human serum matrix was created according to the procedure proposed by Parham and Zargar [79]: 1.3 g of NaCl (87 mM), 0.16 g of NaHCO3 (7.9 mM), 29 mg of aspartic acid (0.88 mM), 9.1 mg of alanine (0.41 mM), 10 mg of arginine (0.21 mM), 9.1 mg of lysine (0.20 mM), 6.6 mg of phenylalanine (0.16 mM), 2.3 mg of glycine (0.14 mM), 3.2 mg of serine (0.12 mM), 6.3 mg of histidine (0.12 mM), 3.7 mg of tyrosine (81 µM), and 3.5 mg of tryptophan (69 µM) were dissolved in deionized water in a 250 mL volumetric flask.

### 4.2.2 BDD electrodes

A BDD electrode (700 µm thick, boron concentration of $3 \times 10^{20}$ atoms/cm$^3$) was supplied by Mintres B.V and used for the electrochemical experiments characterizing DVF and VF. Both sides of the electrode, nucleation, and polished growth side, were used for experiments. This is a free-standing electrode (FSE). The nucleation side was the area attached to the substrate and thus where seeding took place, whereas the growth side is exposed to the reactor. The growth side is usually characterized by larger grain sizes and lower $sp^2$ carbon content [80].

### 4.2.3 Electrochemistry experiments

An Autolab PGSTAT128N operated by Nova 2.1 software (Metrohm, The Netherlands) was used to conduct electrochemical measurements. The BDD WE was employed with a silver-silver chloride electrode (RE-1BP from ALS co.) as RE and a 23 cm platinum wire (catalog No. 012961 from ALS, Japan ALS co.) as CE to create a conventional three-electrode setup. The electrodes were placed inside a Teflon cell with 5 mm diameter hole for the BDD WE exposure to the solution, and both the CE and RE were submerged inside. All experiments were performed in laboratory conditions (23 °C).

Several voltammetric techniques were applied to perform the experiments. The first was cyclic voltammetry (CV). In CV the voltage is swept from zero to a positive value to a negative value and back to zero. For each CV scan this was done three times to verify its accuracy. Another similar method used is linear sweep voltammetry (LSV). Unlike CV, in LSV the potential applied only sweeps from zero to a desired positive value for a anodic scan, and negative value for a cathodic scan.

To develop a sensitive and reliable method a more robust technique was used, differential pulse voltammetry (DPV). In DPV a constant potential pulse ($E_{pulse}$) is superimposed on a dc-potential ($E_{begin}$) and increased by a potential step ($E_{step}$) after each pulse. The current is sampled before ($i_1$) and at the end of ($i_2$) the potential pulse and the difference is graphed versus the potential, a scheme of DPV pulse waveform can be found in Figure 4.5. DPV has several advantages over CV, it has lower capacitive currents (higher sensitivity) and better-developed peak-shaped signals (easier to distinguish similarly positioned oxidation peaks). The initial values for the significant DPV parameters are: $E_{pulse}$ of 60 mV, $E_{step}$ of 15 mV and $t_{int}$ of 50 ms.

Two surface terminations were tested for the BDD electrode, namely a oxygen-enriched surface and hydrogen terminated one . To alter the BDD surface termination, two different pre-treatment procedures were employed, anodic oxidation and cathodic hydrogenation. For each method, 20 minutes of either +2.4 V (anodic mode) or –2.4 V (cathodic mode) was applied to the BDD electrode in 0.1 M $H_2SO_4$, and between individual measurements the treatment was reapplied for 30 s in the solution. The anodic potential will create an oxygenated BDD (O-BDD) surface and the cathodic potential a hydrogenated BDD (H-BDD) surface. The ferrocyanide solution was used to determine the effectiveness of each method.

Initial measurements were made for the characterization of the FSE. CV was used to determine the potential window and double-layer capacitance of FSE. The double layer capacitance ($C_{dl}$) can be determined by the following equation $C_{dl} = \Delta I_{AV}/v\, A_{geom}$, herein $\Delta I_{AV}$ is the average background current difference between the forward and backward CV scan (in A), $v$ is the used scan rate (0.1 V/s), $A_{geom}$ is the area of the electrode exposed to the measured solution (20 $mm^2$). Acidic (0.1 M $H_2SO_4$), neutral (Phosphate Buffered Saline, PBS) and alkaline (0.1 M NaOH) media were all investigated.

Furthermore, a scan rate study (10, 25, 50, 75, 100, 125, 150, 200 and 250 mV/s) was performed using the redox couples $[Fe(CN)_6]^{3-/4-}$ and $[Ru(NH_3)_6]^{3+/2+}$. The data obtained with $[Ru(NH_3)_6]^{3+/2+}$ redox markerwere used in the Randles-Sevcik equation for the determination of the effective electrode surface area ($A_{eff}$). The Randles-Sevcik equation for a reversible process is as follows: $I_p = 2.69 \times 10^5\, n^{3/2}\, A_{eff}\, D^{1/2}\, v^{1/2} c_0$. $N$ is the number of exchanged electrons (i.e., 1), $D$ is the diffusion coefficient of $[Ru(NH_3)_6]^{3+/2+}$ ($7.7 \times 10^{-6}$ $cm^2/s$), v is the scan rate, $c_0$ the concentration (1 mM), and $I_p$ the peak current

An initial investigation into VF and DVF was performed. Here both O-BDD and H-BDD terminated surfaces on the nucleation and polished growth side of the FSE were tested. 100 µM solutions of VF and DVF in acidic (0.1 M $H_2SO_4$), neutral (PBS) and alkaline (0.1 M NaOH) were investigated. The measurements were made using CV, and LSV.

After the initial measurements, a more in-depth investigation into the influence of the pH values was performed. The VF and DVF Britton-Robinson (pH 2-12), sulfuric acid (pH 0.7) and sodium hydroxide (pH 13) solutions were tested with the standard DPV parameters on both types of surface termination. The crucial DPV parameters were further optimized under optimal pH conditions. The following ranges were tested: $E_{pulse}$ 10-200 mV, $E_{step}$ 5-25 mV, and $t_{int}$ 10-70 ms. First, the optimal $E_{pulse}$ was determined (while other two parameters were kept constant), this value was then used in the determination of $t_{int}$ and similarly both optimized values are used for the assessment of $E_{step}$.

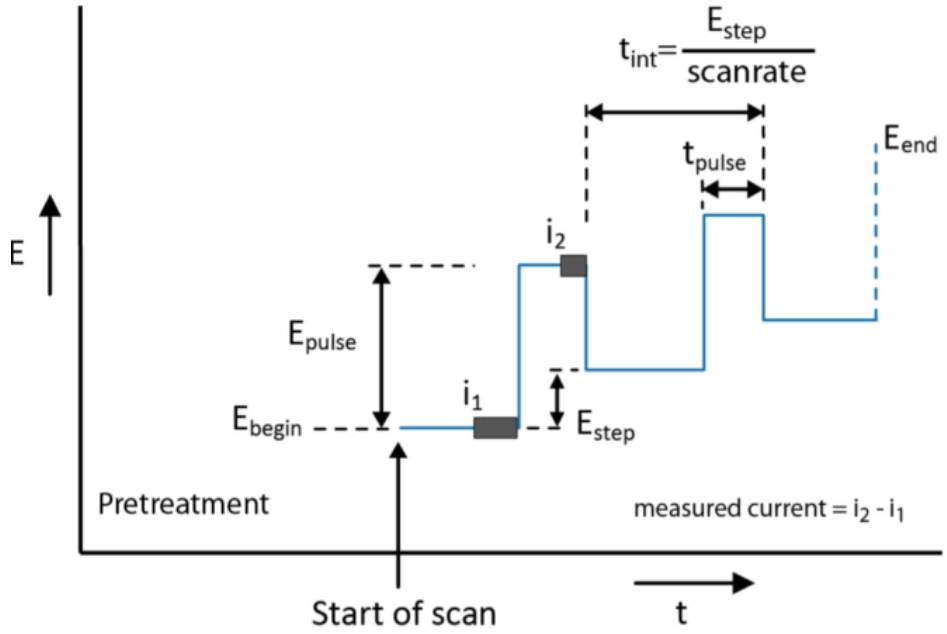


*Figure 4.5 An overview of a differential pulse waveform.* [81]

With the optimal DPV parameters a concentration study was performed, three replicate measurements were made for each VF and DVF concentration. The average was taken and used to create an analytical curve by least square's linear regression method. A threefold and tenfold of the standard deviation of the peak currents ($n$ = 10) of the lowest measurable concentration were taken ,and divided by the slope of the corresponding concentration dependence to assess limit of detection (LOD) and limit of quantification (LOQ), respectively.

Furthermore, the intra-day (n=10) repeatability of the method was investigated. The effect of stirring and thirty second reapplication of the pretreatment were investigated. A scan rate study of VF and DVF was performed with LSV. This was performed to determine if the reaction is diffusion or adsorption controlled.

Several interfering compounds typically present in biological fluids were investigated. A 500-fold excess of inorganic ions ($Na^+$, $K^+$, $Ca^{2+}$, $Mg^{2+}$, $Cl^-$, $HPO_4^{2-}$), sucrose and glucose and their effects on the DPV response were examined. Furthermore, the effect of dopamine, citric acid and ascorbic acid in the

following concentrations were investigated: 1:1,1:10, 1:25, 1:50, 1:100. Any interferent was insignificant if intensity was changed by less than 10%. The effects of synthetic urine, synthetic serum and river water on the detection method were investigated as well. The synthetic urine, serum and river water samples were spiked with 50 µM VF or DVF and subsequently diluted in the desired supporting electrode. The following concentrations were investigated, 25 µM, 10 µM and 5 µM. The standard addition method was applied, with three aliquots of stock solution (100 µL of 1 mM), to determine the VF and DVF concentrations.

## 4.3 Scanning electron microscopy (SEM)

A scanning electron microscope (JSM-6010LA) was used to investigate the sample surfaces in secondary electron imaging mode at a voltage of 10 keV and 15 keV. The surface morphology of the different electrodes (working, counter and reference) was examined at a magnification range from 500x to 25000x and the built-in software (In Touch Scope) was used for the analysis of the SEM images. To determine the grain size of the grown BDD films, four different images were taken per sample, and 10 random grains were measured from each electrode.

## 4.4 Raman spectroscopy

Raman spectroscopy (Horiba LabRAM HR setup) was used to assess the characteristics and composition of the different BDD electrodes. The measurements were performed with a solid state laser corresponding to an argon ion laser emitting at 514 nm wavelength, a slit of 100, a hole of 1000, a ND filter of 50%, a magnification of 50x, and 3-5 accumulations with an acquisition time of 10 seconds. The number of accumulations depended on the noise and spikes present in the curves, as they could be decreased by averaging them out. Several locations were investigated on each electrode in a spectral range of 200 $cm^{-1}$ to $2000^{-1}$ to determine boron doping levels and $sp^2$ content.

# 5 Results and discussion

## 5.1 Free standing electrode characterization

In this section, the FSE is characterized by SEM, Raman spectroscopy, and electrochemical tests. The nucleation side and polished growth side of the FSE are investigated. The differences between the surfaces are explored and clarified.

### 5.1.1 SEM

The SEM images displaying the surface morphology of the FSE electrode can be found in Figure 5.1A and 5.1B for the nucleation and polished growth side, respectively. By comparing the two different SEM images, it can be seen that the crystals at the nucleation side are significantly smaller than the crystals at the growth side. This is due to growth at the nucleation side beginning with small crystals grown from seeded nanodiamonds. As growth progresses, these crystals merge together, resulting in larger crystals which continue the growth. This will lead to an increase in grain size and a decrease in the amount of grain boundaries. The nucleation side has grain sizes ranging from 0.8 µm to 4 µm with an average size of 1.3 µm, whereas the growth side has grain sizes ranging from 60 µm to 130 µm and an average size of 105 µm.

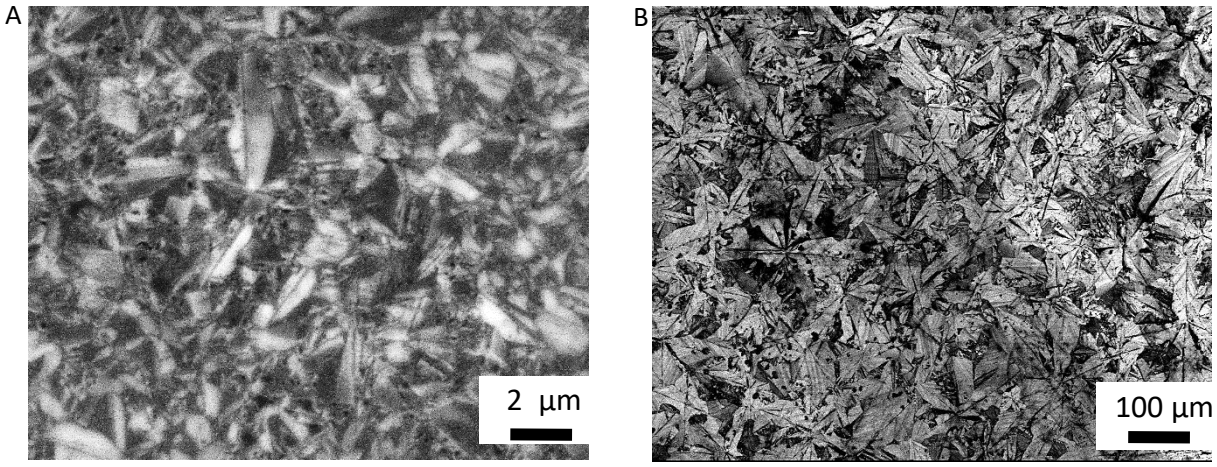


*Figure 5.1 SEM image of the A) Nucleation side and B) growth side of the free standing BDD electrode.*

### 5.1.2 Raman spectroscopy

The Raman spectra of the two sides of the FSE provide insight into the composition of the carbon material the electrode is made of. Three distinct peaks can be observed in the Raman spectrum of the nucleation side in Figure 5.2A, and only one major one for the growth side in Figure 5.2B. The peak at a Raman shift of circa 1332 $cm^{-1}$ corresponds to diamond ($sp^3$ carbon), the broader peak (the G band) between 1500 $cm^{-1}$ and 1600 $cm^{-1}$ indicates the presence of a variety of non-diamond carbon phases ($sp^2$ carbon). Qualitative information on the composition of the FSE sides can be determined from these Raman spectra, mainly the diamond quality factor and an estimate for the boron doping levels. The diamond quality factor is found by utilizing the following equation: $fq = 75\ I_d / 75\ I_d + \sum I_{nd}$, where $I_d$ is the Raman diamond peak area and and $I_{nd}$ the sum of the Raman $sp^2$ phase peak areas [82]. The boron doping level can be evaluated using a tool developed by Mortet et al. [83]. This tool allows for the evaluation of Raman measurements by analysing two characteristic Raman peaks which are associated with the Fano-shaped maximum of phonon density of states (1200 $cm^{-1}$) and zone-center phonon line of heavily boron-doped diamond (1330 $cm^{-1}$).

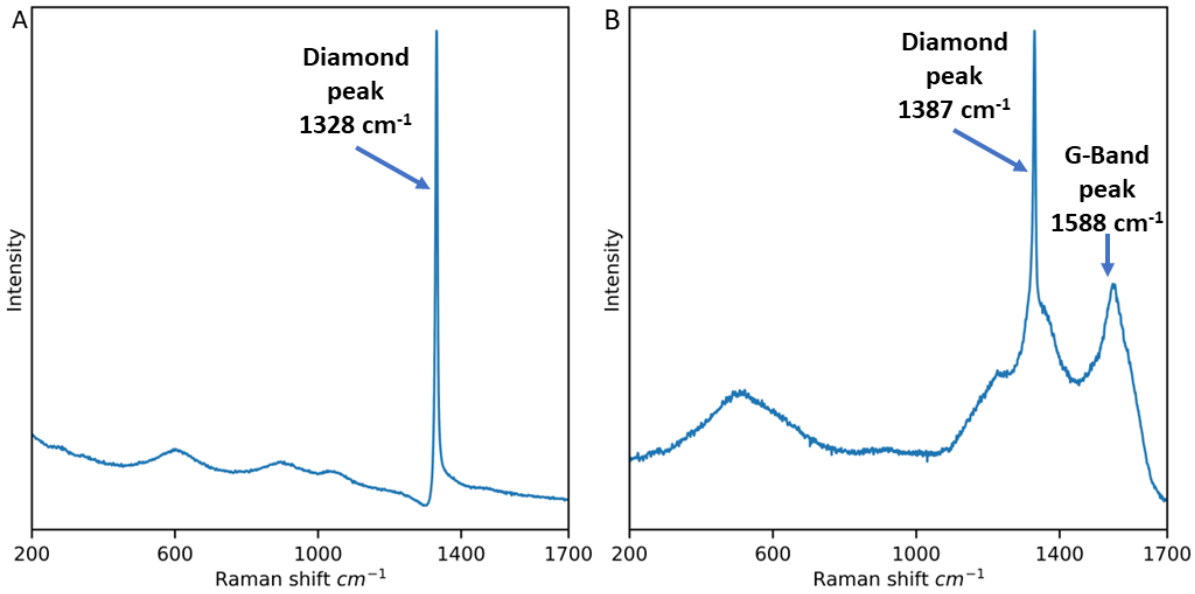


*Figure 5.2 Raman spectroscopy of A) growth and B) nucleation side of the FSE.*

The nucleation side has an diamond quality factor of 97.9%, whereas the growth side produces no visible G-band ($sp^2$). This difference in ratio can be explained by a difference in grain sizes observed in the SEM images of Figure 5.1. The boron doping level of both sides are ~$5 \cdot 10^{19}$ atoms/$cm^3$. This was unexpected as Mintres declares a doping level of $3 \cdot 10^{20}$ atoms/$cm^3$, one order of magnitude higher. The provided samples thus have a lower level of boron doping than expected.

### 5.1.3 Electrochemical characterization of free standing electrode

The differences in electrochemical responses between the nucleation and polished growth surface are studied using cyclic voltammetry of a alkaline electrolyte ( 0.1 M NaOH), neutral electrolyte (PBS), acidic electrolyte (0.1 M $H_2SO_4$) and the redox markers $[Fe(CN)_6]^{3-/4-}$ and $[Ru(NH_3)_6]^{3+/2+}$ (both 1 mM) in 0.5 M $KNO_3$. The results for the potential windows (limits are defined as when the current response reaches ~±30 µA) and double layer capacitance values for each electrolyte can be found in Table 5.1. Two trends can be observed: a lower pH shifts the potential window to a more positive range and the nucleation side has a smaller double layer capacitance and larger potential window overall. This could be due to the lower boron doping levels observed in the samples, which changes the effect of the $sp^2$ content. The larger $sp^2$ content could possible lead to a larger potential window, as was also observed in other lower boron doped diamond electrodes [84].

The hydrogen (HER) and oxygen (OER) evolution reactions of water determine the width of the potential window. The kinetics and efficiency of these reactions depend on the concentration of $H^+$ and $OH^-$ ions. A large amount of $H^+$ will ease the HER and a large amount of $OH^-$ will ease the OER. The shift in pH thus changes the concentration of $H^+$ and $OH^-$ and with the location of the reactions.

*Table 5.1. Electrochemical parameters obtained from CV measurements conducted in several supporting electrolytes.*

| | 0.1 M NaOH | PBS | 0.1 M $H_2SO_4$ |
|---|---|---|---|
| **Nucleation side** | | | |
| Available potential range (V) | −1.35 – +1.05 | −1.15 – +1.95 | −0.8 – +2.0 |
| Potential window (V) | 2.4 | 3.1 | 2.8 |
| $C_{dl}$ (µF/cm$^2$) | 6.1 | 4.4 | 4.4 |
| **Growth side** | | | |
| Available potential range (V) | -1.35 – +1.05 | -1.35 – +1.6 | -0.7 – +1.92 |
| Potential window (V) | 2.4 | 2.96 | 2.62 |
| $C_{dl}$ (µF/cm$^2$) | 66.9 | 41.8 | 33.0 |

Several electrochemical parameters can be acquired from the $[Fe(CN)_6]^{3-/4-}$ and $[Ru(NH_3)_6]^{3+/2+}$ redox reactions, these are the differences between the cathodic and anodic peak potentials ($\Delta E_p$), peak heights ($I_a$, $I_C$) and peak ratios ($I_c/I_a$). Table 5.2 summarizes the results for these characteristics for an untreated BDD surface. The main difference between the nucleation and growth side lies in the peak heights and peak ratios. For the nucleation side, the intensities of the responses ($I_a$ and $I_c$) are higher due to a higher conductivity, although the ratios between the peaks are similar. If this ratio where to be equal to 1 an ideal reversible process would be taking place. This is not the case, this indicates that the electron transfer kinetics are hindered slightly on both surfaces, due to the surface characteristics. The values for the $\Delta E_p$ of ferrocyanide are are lower for the nucleation side, whereas the values for $\Delta E_p$ of ferrocyanide are higher for $\Delta E_p$. $\Delta E_p$ is an indicator for the reversibility of the redox reaction. An $\Delta E_p$ of 59 mV is the theoretical value for an reversible reaction. A lower value indicates a slower redox process and is most likely due to surface termination of the BDD electrodes which influence the reaction. This is further supported by the difference between $[Fe(CN)_6]^{3-/4-}$ and $[Ru(NH_3)_6]^{3+/2+}$ on both electrodes. $[Fe(CN)_6]^{3-/4-}$ is more sensitive to the surface termination and is further off the ideal $\Delta E_p$ value. This would indicate the presence of oxygen groups at the surface.

*Table 5.2. Analytical results of CV from measurements of 100 µM $[Ru(NH_3)_6]^{3+/2+}$ in 0.5 $KNO_3$ and 100 µM $[Fe(CN)_6]^{3-/4-}$ in 0.5 $KNO_3$ on the nucleation and growth side of the FSE.*

| | $\Delta E_p$ (V) | $I_c$ (µA) | $I_a$ (µA) | $I_c/I_a$ |
|---|---|---|---|---|
| **Nucleation side** | | | | |
| $[Fe(CN)_6]^{3-/4-}$ | 0.253 | -35.0 | 39.6 | 0.88 |
| $[Ru(NH_3)_6]^{3+/2+}$ | 0.359 | -57.4 | 53.5 | 1.07 |
| **Growth side** | | | | |
| $[Fe(CN)_6]^{3-/4-}$ | 0.278 | -32.9 | 37.3 | 0.88 |
| $[Ru(NH_3)_6]^{3+/2+}$ | 0.303 | 48.1 | 45.8 | 1.05 |

As mentioned in section 5.1, the results of the scan rate study with $[Ru(NH_3)_6]^{3+/2+}$ were employed to calculate the effective surface area of the electrodes. This value is important for the comparison of different electrodes in section 5.4. Figure 5.3 shows the results from the study. By employing the Randles-Sevcik equation an effective surface area of 23.2 $mm^2$ and 18.9 $mm^2$ were determined for the nucleation and growth, respectively. The value for the nucleation side is larger than its geometric area, this could be explained by the unevenness of the surface. The surface is not perfectly flat and as such this could increase the effective surface area. For the growth side the surface is slightly smaller than the geometric area of 19.6 $mm^2$, it is possible parts of the electrode surface are incapable of interacting with the solution due to fouling.

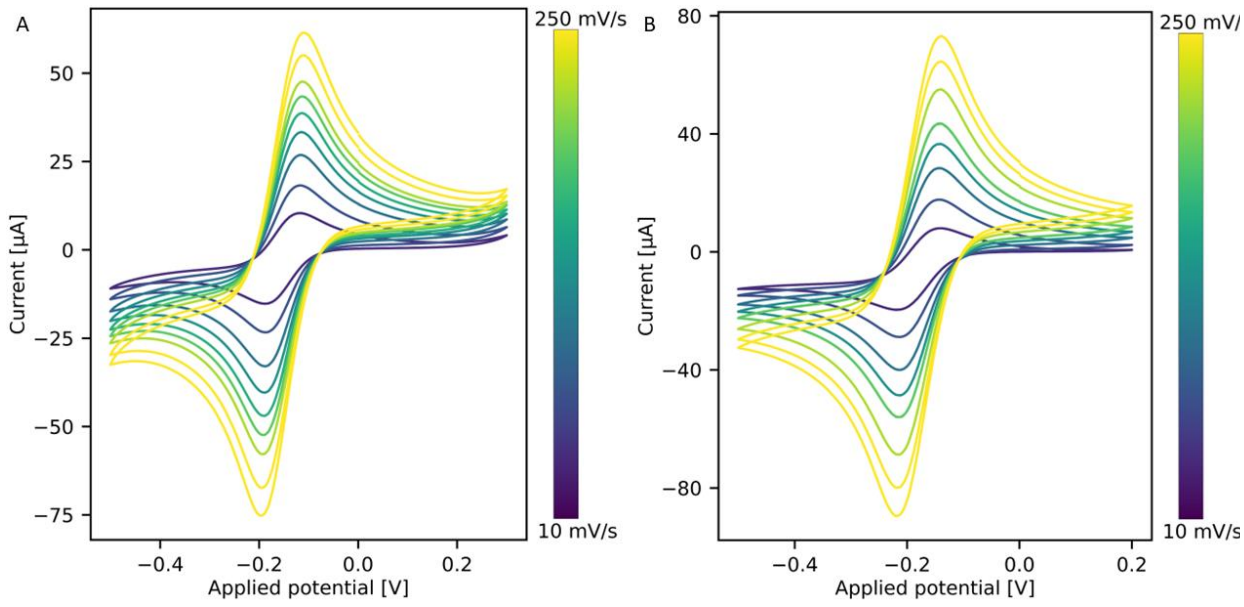


*Figure 5.3. Scan rate study results for A) the growth side and B) the nucleation side of the FSE with $[Ru(NH_3)_6]^{3+/2+}$ redox probe with scan rates varying in the range 10-250 mV/s.*

## 5.2 Detection of DVF and VF on free standing electrode

In this section, the electrochemical characteristics of VF and DVF are studied. An optimized electroanalytical detection method is created and the effect of several interfering compounds is explored. Further, the applicability of the developed method is investigated by investigating the compounds in synthetic serum, synthetic urine and river water.

### 5.2.1 Effect of surface termination and pH media

To investigate the effects of surface termination the redox marker $[Fe(CN)_6]^{3-/4-}$ is employed. As mentioned in Section 2.6., the reaction of $[Fe(CN)_6]^{3-/4-}$ is of an inner-sphere nature and the surface termination has significant influence on the electron transfer kinetics of $[Fe(CN)_6]^{3-/4-}$. The presence of oxygen groups with negative dipole moments created by anodic pretreatment (O-BDD) will repel the negatively charged ions, whereas a cathodic pretreatment (H-BDD) with positive dipole moments has the opposite effect. This corresponds with a shift in $\Delta E_p$; anodic pretreatment will increase it, while cathodic pretreatment will decrease it. This can be observed in Appendix A.1.

The CVs of VF and DVF were recorded in three distinct media (0.1 M $H_2SO_4$, 0.01 M PBS of pH 7.4, 0.1 M NaOH), encompassing two surface terminations (H-BDD, O-BDD) as well as the two surfaces (polished growth side, GS and nucleation side, NS), selected surface recordings with the best results are illustrated in Figure 5.4 (for others see Appendix A.2. and A.3.). It can be seen that VF provided two oxidation peaks at +1.30 V, +1.45 V in acidic media and one at circa +1.30 V for neutral media on all electrodes. DVF provides no oxidation peak for any O-BDD surface and only limited responses on H-BDD surfaces in acidic medium. Furthermore, no reduction peak is present in any CV, this implies all oxidative reactions of VF and DVF are irreversible in these conditions. The peak potentials ($I_p$) for the DPV measurements can be found in Table 5.3.

*Table 5.3. Peak potentials of peaks present in DPV measurements of 100 µM VF and 100 µM DVF in selected electrolytes and with different surface characteristics.*

| Electrolyte | Surface | $I_p$ (µA) | | | Ratio NS/GS | | |
|---|---|---|---|---|---|---|---|
| **100 µM VF** | | | | | | | |
| | | Peak 1 | Peak 2 | Peak 3 | Peak 1 | Peak 2 | Peak 3 |
| 0.1 M $H_2SO_4$ (pH 0.6) | H-BDD-GS | 5.8 | 0.6 | - | 0.95 | 7.83 | - |
| | H-BDD-NS | 5.5 | 4.7 | - | | | |
| | O-BDD-GS | 2.7 | 7.1 | 3.1 | 3.00 | 1.21 | 2.52 |
| | O-BDD-NS | 8.1 | 8.6 | 7.8 | | | |
| PBS | H-BDD-NS | 3.0 | | | - | | |
| | O-BDD-GS | 1.4 | | | 4.79 | | |
| | O-BDD-NS | 6.7 | | | | | |
| **100 µM DVF** | | | | | | | |
| 0.1 M $H_2SO_4$ (pH 0.6) | H-BDD-NS | 2.4 | | | - | | |

In addition, to ascertain the optimal surface between growth and nucleation side the DPV curves are displayed in Figure 5.4 B, D. An additional peak for VF is visible on the O-BDD surface at +1.6 V. Overall, the nucleation sides provided superior current peak heights to the growth side for VF, as can be seen

in Table 5.3. A possible explanation is the superior conductivity of the $sp^2$ carbon present at the nucleation side. As mentioned before, this improves the rate of electron transfer kinetics and can thus lead to higher peaks. The decision was made to continue all further tests on the nucleation side of the FSE.

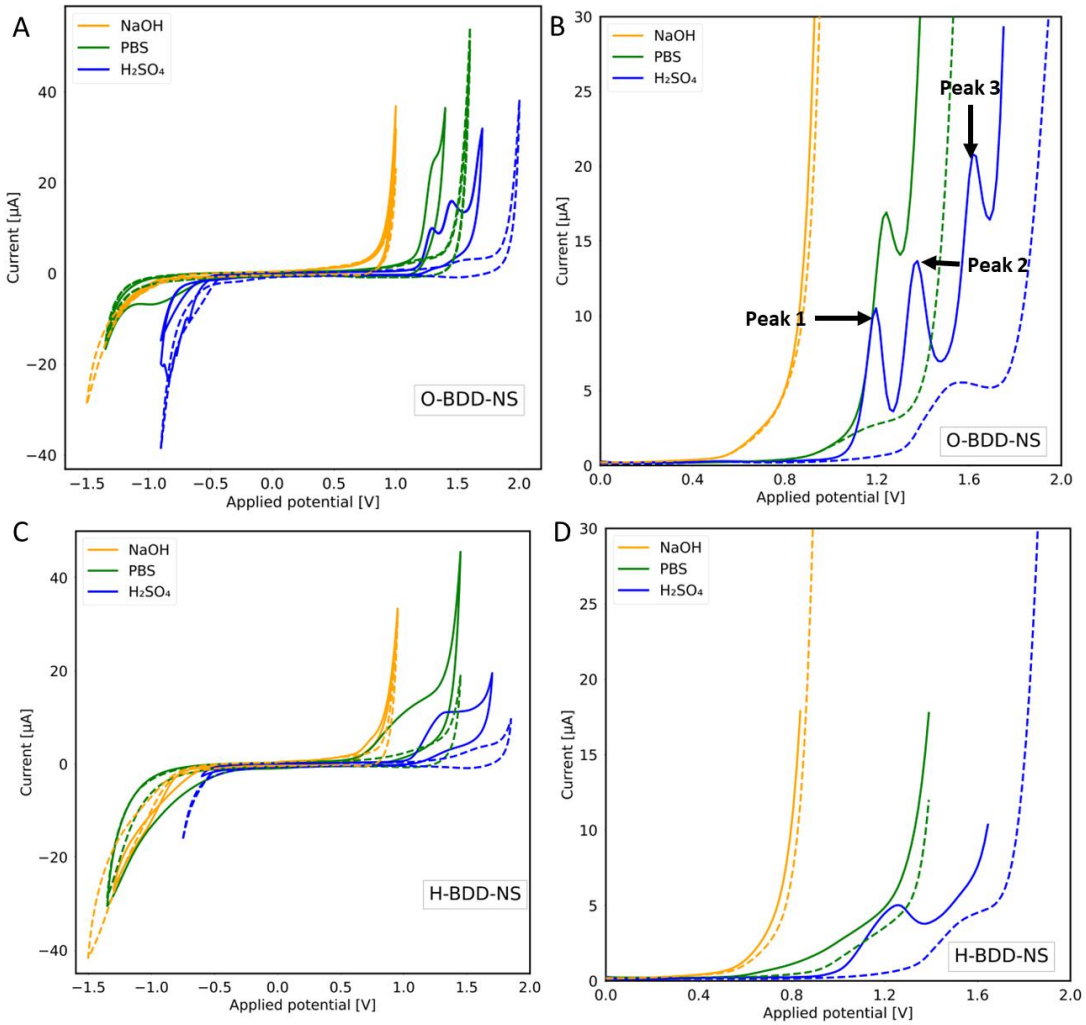


*Figure 5.4 Selected CV (A, C) and DPV (B, D) of 100 µM VF recorded on O-BDD-NS (A, B) and 100 µM DVF recorded on H-BDD-NS (C, D) and measured in various supporting electrolytes. The dashed lines correspond to the supporting electrolyte.*

### 5.2.2 pH study

The results of the DPV curves from the pH study can be seen in Figure 5.4 and noticeable differences are present between the different surface terminations. The characteristics of the oxidative peaks depend heavily on pH of the solution, which is evident in Figure 5.5. Which technique used, pH range – what types of supporting electrolytes (BRB, NaOH, H2SO4, etc.)

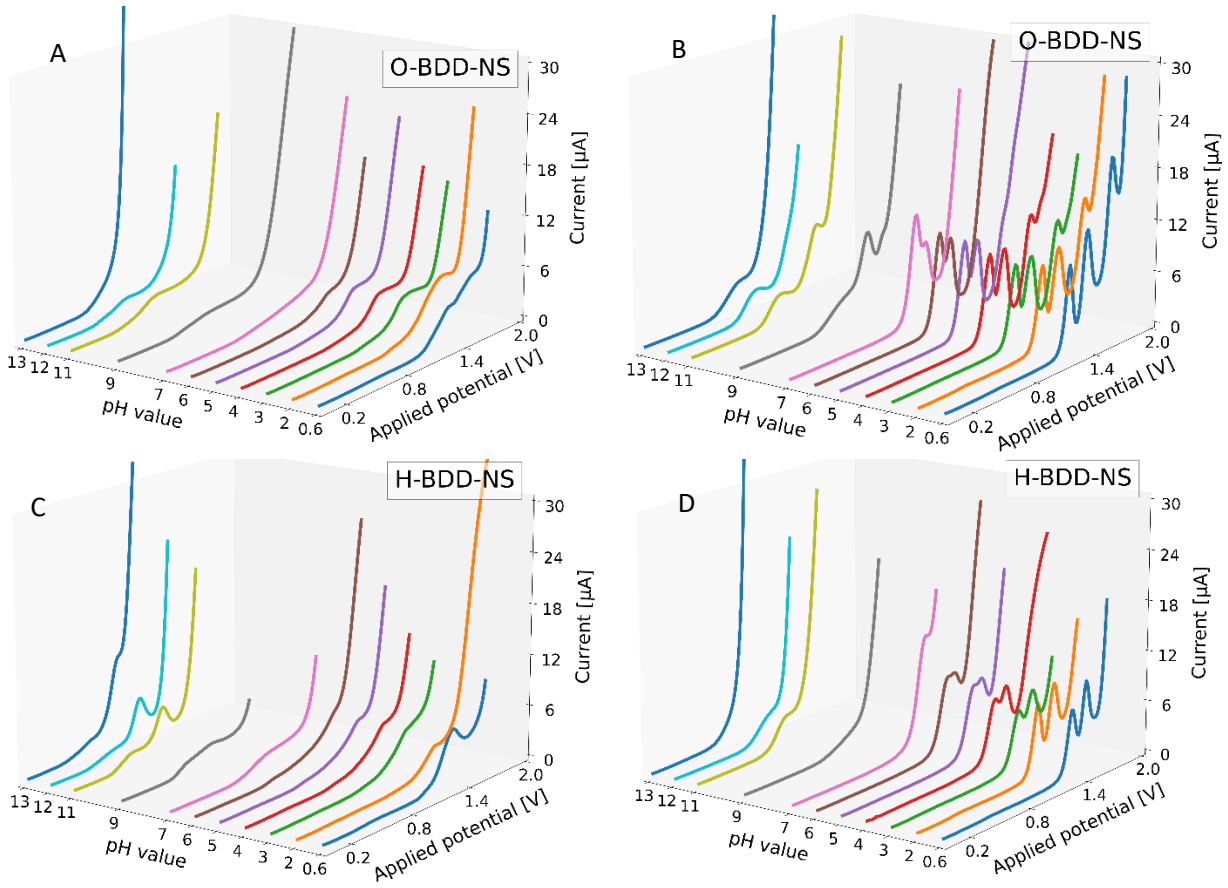


*Figure 5.5 The results DPV measurements for the pH study of (A, C) 100 µM DVF and (B, D) 100 µM VF on (A, B) O-BDD-NS and (C, D) H-BDD-NS surfaces.*

Figure 5.5A demonstrates that there is no observable development of any oxidative peak on the O-BDD surface for DVF. The hydroxyl groups most likely interfere with the electron transfer of the reaction and thus limit detection. Figure 5.5C illustrates that detection of DVF on the H-BDD surface is possible in a limited capacity. There is one peak at very acidic media add pH value and one peak at both pH 11 and 12. The peaks in alkaline media are from the deprotonated version of DVF. These are negatively charged, and thus would not appear on the O-BDD surface, as the negatively charged oxygen groups would repulse the deprotonated DVF molecules. No such effect takes place for the H-BDD as the lack of negatively charged O-groups makes it a more neutral surface, as can be seen in the difference between Figure 5.5A and Figure 5.5C. Furthermore, the peak developed in acidic medium is from a protonated version of DVF, a protonated form of DVF exists until pH 8.5 (Appendix Figure A.4). One would anticipate that the O-BDD surface would perform better for this molecule; however, as mentioned no reactions are discernible on this surface. The hydroxyl groups of the O-BDD surface thus inhibit the reaction. A possible explanation is the following, it has been noted that O-BDD surfaces are less conductive compared to H-BDD surfaces. This reduced conductivity could impede the reaction.

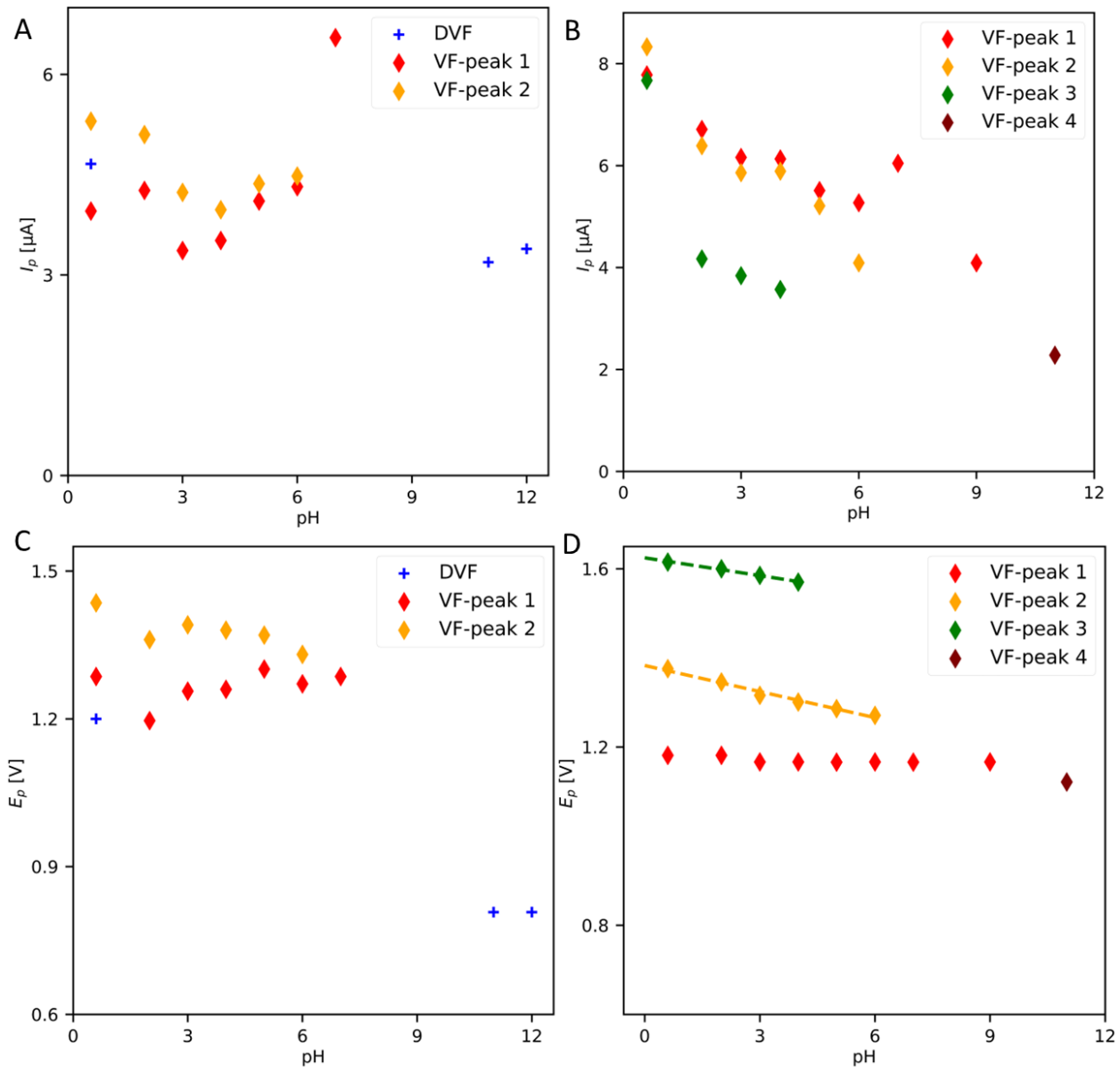


*Figure 5.6 The dependences of peak currents ($I_P$) (A, B) and peak potentials ($E_p$) (C, D) on the pH study on O-BDD (C,D) and H-BDD (A,B) surfaces. Here VF-peak 1,2 and 3 are the peaks developed in acidic media from lowest to highest potential, whereas peak 4 is the peak developed in alkaline media.*

For VF, several observations can be made in Figure 5.5B,D. In acidic media, from pH 0.6 to 4.0, three oxidative peaks are present on the O-BDD surface, while the H-BDD DPV curve records only two peaks in this range. However, for both O-BDD and H-BDD the two peaks continue into neutral media until pH 7.0 and one peak even to pH 9.0 for O-BDD. In Appendix Figure A.5, it can be noticed that only a single VF form exists in acidic media. The oxidation of VF most likely includes several sequential reactions which each exhibits its own oxidation peak. In Figure 5.6D it can be observed that both peak two and peak three have a clear linear shift to lower values on O-BDD surface. This relation can be expressed by the following two equations.

O-BDD: $E_{p2}$(V) = -0.019 · pH + 1.383 $R$ = 0.991 (Eq. 5.1)

O-BDD: $E_{p3}$(V) = -0.014 · pH + 1.624 $R$ = 0.996 (Eq. 5.2)

Both slopes of -0.019 V/pH and -0.14 V/pH are far from the theoretical Nernstian slope of -0.059 V/pH for redox reactions of an equal number of protons and electrons. This would suggest that these reactions involve an unequal number of protons and electrons. According to Appendix Figure A.5, until pH 9 the primary form (> 50%) of VF present in the solution is in protonated form. At higher pH (> pH 9.0) it will shift to the neutral form and at a pH of 13 a limited amount (<10%) of deprotonated VF will be present. This agrees with the observations of the linear shift and appearance of peaks one to three. However, peak three disappears due to the shrinking potential window and peaks one and two slowly merge until they become indistinguishable. For peak one an effectively stable peak potential is recorded between pH 1.0 to 9.0, this reaction is thus independent of the pH of the solution. At the peak developed in the alkaline media and neutral form of VF is present (peak four in Figure 5.6). Only on the O-BDD surface is present an observable peak from VF, which becomes almost indistinguishable in the OER of the solution. On the H-BDD surface, the OER is already fully occurring, and no discernible peak is evident.

From the Figures 5.6C and D several observations can be made for the current peak heights of DVF and VF. To begin with DVF, the pH analysis reveals the presence of only three peaks, with the highest peak occurring at pH 0.6 in 0.1 M $H_2SO_4$ compared to the peaks in the alkaline media. This lead to selection of pH 0.6 as the optimal condition for further voltammetric experiments and optimization.

Progressing to VF on the H-BDD surface, a certain degree of inconsistency in the peak currents of the two peaks is observed. These inconsistent results stem from the gradual merging of these peaks, making it challenging to differentiate the individual contributions to the signal. Distinguishable peak currents only manifest at lower pH values below pH 3.0. Small differences are present for VF on O-BDD surface. The larger potential window allows for the visibility of a third oxidative peak of VF. The third peak is visible for pH 1.0 to 4.0 afterwards the windows shrinks and the OER is already taking place. The peak currents of the three peaks decrease as the pH increases. This trend continues for peak three until disappears and for peak one and two until they coalesce at pH 7.0. These observations stresses the superior characteristics of VF on O-BDD surfaces due to the greater peak heights (> 50% ) and greater independence between peaks (0.150 mV for H-BDD and 0.180 mV for O-BDD). In light of these findings, the decision is made to advance with VF in 0.1 M $H_2SO_4$ at pH 0.6 for further testing and experiments.

### 5.2.3 Scan rate study

In Figure 5.7, the results from the LSV of 100 µM VF and DVF on O-BDD and H-BDD, respectively, are depicted – LSV at different scan rates – range – this information is missing in the text. It can immediately be noticed that the voltammogram of VF only has two visible peaks while in the previous DPV three distinct peaks could be seen. As DPV is a more robust detection method overall, more distinct peaks can be detected and even distinguished from the OER. For DVF, one peak is present over the entire scan rate. The peak currents of all the curves increase linearly with an increase in the square root of the scan rate. This can be seen in Figures 5.7A, B. The linear dependences are described by the following equations:

O-BDD - $VF_1$: $I_p(\mu A) = 24.2\ v^{1/2} - 0.56$ R = 1 (Eq. 5.3)

O-BDD - $VF_2$: $I_p(\mu A) = 24.0\ v^{1/2} - 1.12$ R = 0.999 (Eq. 5.4)

H-BDD - DVF: $I_p(\mu A) = 11.5\ v^{1/2} + 0.13$ R = 0.998 (Eq. 5.5)

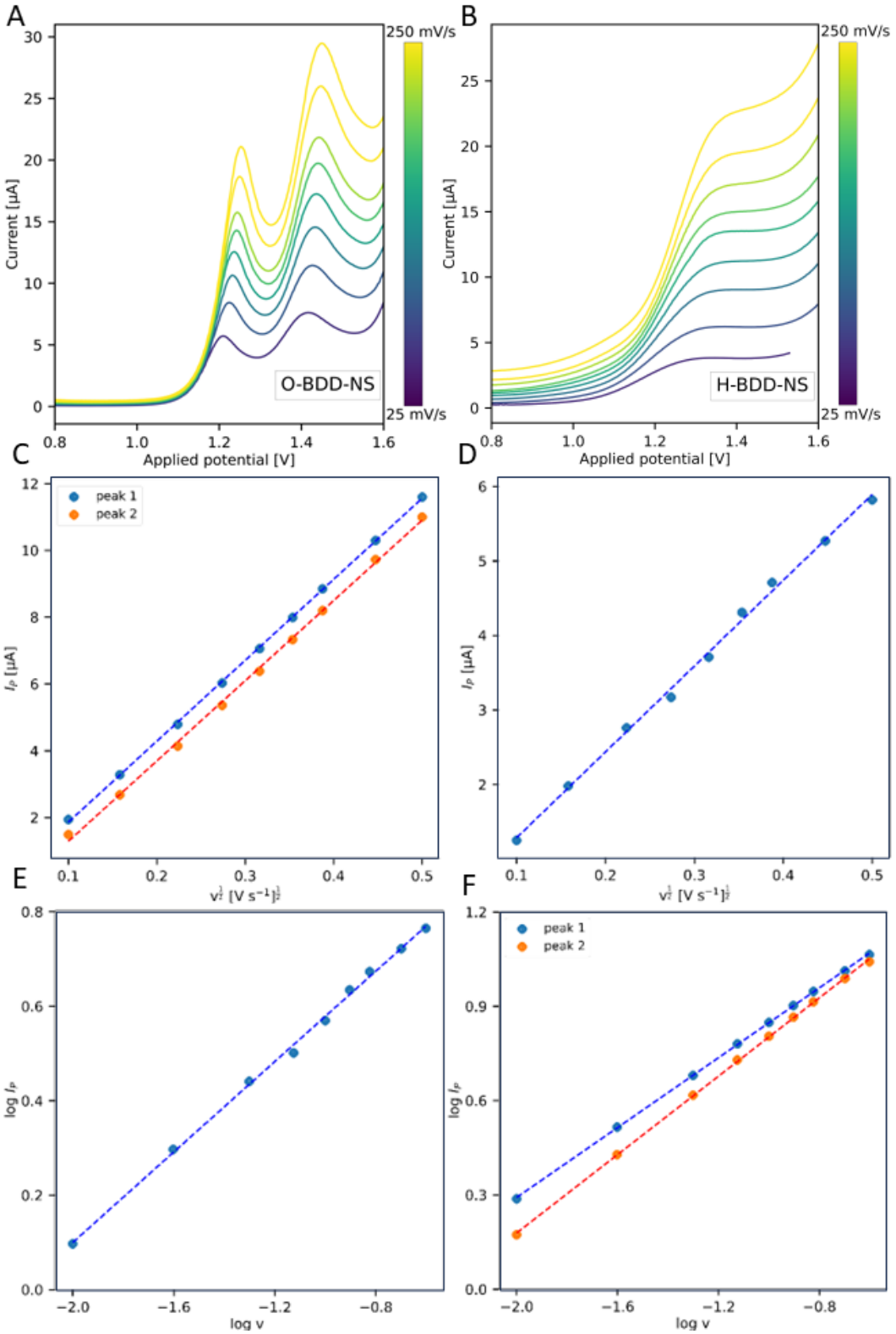


*Figure 5.7. (A,B) The results of LSV for the range of scan rates v of (A,C,E) 100 µM DVF in 0.1 M $H_2SO_4$ (pH 0.6) on the H-BDD and (B,D,F) 100 µM VF in 0.1 M $H_2SO_4$ (pH 0.6) on O-BDD surfaces. (C,D) the linear relation between peak potential ($I_p$) and square root of the scan rate ($v^{1/2}$) and (E,F) The logarithmic dependences between peak potential (log $I_p$) and scan rate (log v) are given as well.*

These linear equations prove the diffusion controlled mechanism for the oxidation of VF and DVF on BDD surfaces. Further evidence for this conclusion is the results of the log $I_p$ vs log $v$ study, as seen in Fig. 5.8E and F. The corresponding graphs have the following equations:

O-BDD - $VF_1$: $\log(I_p(\mu A)) = 0.56 \log(v) + 1.4$ $R = 1$ (Eq. 5.6)

O-BDD - $VF_2$: $\log(I_p(\mu A)) = 0.62 \log(v) + 1.42$ $R = 0.9998$ (Eq. 5.7)

H-BDD - DVF: $\log(I_p(\mu A)) = 0.47 \log(v) + 1.06$ $R = 0.9991$ (Eq. 5.8)

The slopes obtained from this analysis are all close to the theoretical value of 0.5 for diffusion controlled processes (1.0 for adsorption controlled processes).

Additionally, an analysis of the different peak potentials revealed a small but notable elevation in their values as the scan rate increased. This was the case for both VF peaks on O-BDD and the DVF peak on H-BDD. This behavior strengthens the earlier observation from section 5.2.1, where no reduction peaks indicated an irreversible voltametric behavior.

### 5.2.4 DPV parameter optimization

With the optimized conditions (pH, surface termination) determined in Section 5.2.3, the DPV parameter optimization can be performed on 100 µM of compound, according to the method outlined in Section 4.2.3. First The final parameters chosen for detection are: (i) a step size ($E_s$) of 15 mV, a modulation amplitude ($A$) of 115 mV and a modulation time ($t$) of 10 ms for VF in 0.1 M $H_2SO_4$ (pH 0.6) on O-BDD; and (ii) a step size ($E_s$) of 15 mV, a modulation amplitude ($A$) of 200 mV, and a modulation time ($t$) of 20 ms for DVF in 0.1 M $H_2SO_4$ (pH 0.6) on H-BDD. The results of the optimization are illustrated in Figure 5.9, and the increase of the peak potentials can found in Table 5.4. For the DPV curves of the optimization of the individual parameters refer to Appendix Figure A.6.

*Table 5.4. Peak potentials of peaks before and after DPV parameter optimization of 100 µM VF in 0.1 M $H_2SO_4$ on O-BDD-NS and 100 µM DVF in 0.1 M $H_2SO_4$ on H-BDD-NS.*

| Initial $I_p$ (µA) | | | Improved $I_p$ (µA) | | | Ratio (new/old) | | |
|---|---|---|---|---|---|---|---|---|
| **100 µM VF in 0.1 M $H_2SO_4$ on O-BDD-NS** | | | | | | | | |
| Peak 1 | Peak 2 | Peak 3 | Peak 1 | Peak 2 | Peak 3 | Peak 1 | Peak 2 | Peak 3 |
| 7.9 | 8.4 | 7.8 | 37.8 | 41.8 | 47.2 | 4.78 | 4.98 | 6.05 |
| **100µM DVF in 0.1 M $H_2SO_4$ on H-BDD-NS** | | | | | | | | |
| 3.2 | | | 21.5 | | | 6.72 | | |

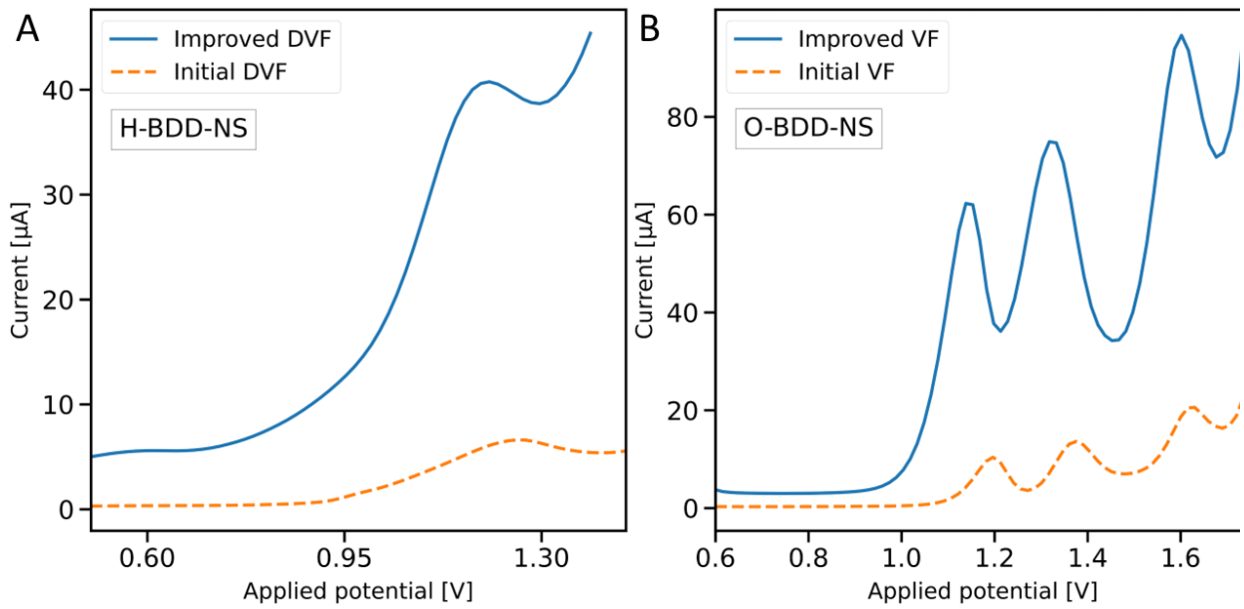


*Figure 5.8. The DPV curves with the optimized parameters (solid blue curve) and the initial DPV settings (dashed orange curve) for (A) 100 µM DVF in 0.1 M $H_2SO_4$ (pH 0.6) on H-BDD and (B) 100 µM VF in 0.1 M $H_2SO_4$ (pH 0.6) on O-BDD.*

### 5.2.5 Stability testing

Stability testing is performed under the optimized conditions for 100 µM DVF in 0.1 M $H_2SO_4$ (pH 0.6) on H-BDD and 100 µM VF in 0.1 M $H_2SO_4$ (pH 0.6) on O-BDD. The effects of (i) no actions, (ii) stirring, and (iii) stirring with pretreatment are all investigated. The pretreatment was an in-solution 30 second application of either anodic (O-BDD) or cathodic treatment (H-BDD). In Figure 5.9 the effects of these actions on the peak currents are displayed, and in Table 5.5 the decrease and RSD of the peak potentials can be found.

A gradual decrease in peak current can be observed in Figure 5.9 for both DVF on H-BDD and VF on O-BDD electrode, when no action is performed between the consecutive scans. This indicates electrode fouling is taking place, the surface treatment is steadily lost as more scans are performed on the pretreated surface.

The decrease in the peak current is less pronounced when a simple stirring action is taken. For DVF on H-BDD a significant drop takes place after the first scan. Further, a smaller continuous drop takes place after the first treatment. No such large decrease is present after the first scan in case of VF on O-BDD surfaces, in contrast a gradual decrease takes place over the ten scans. The incorporation of all actions, thus stirring and electrochemical pretreatment, leads to a stable overall signal for both compounds on the two surfaces. The detection of for both VF on O-BDD surfaces and DVF on H-BDD surfaces yields a highly repeatable signal. Combined with the lack of surface modifications make the surface easily reactivated with only limited in-solution actions

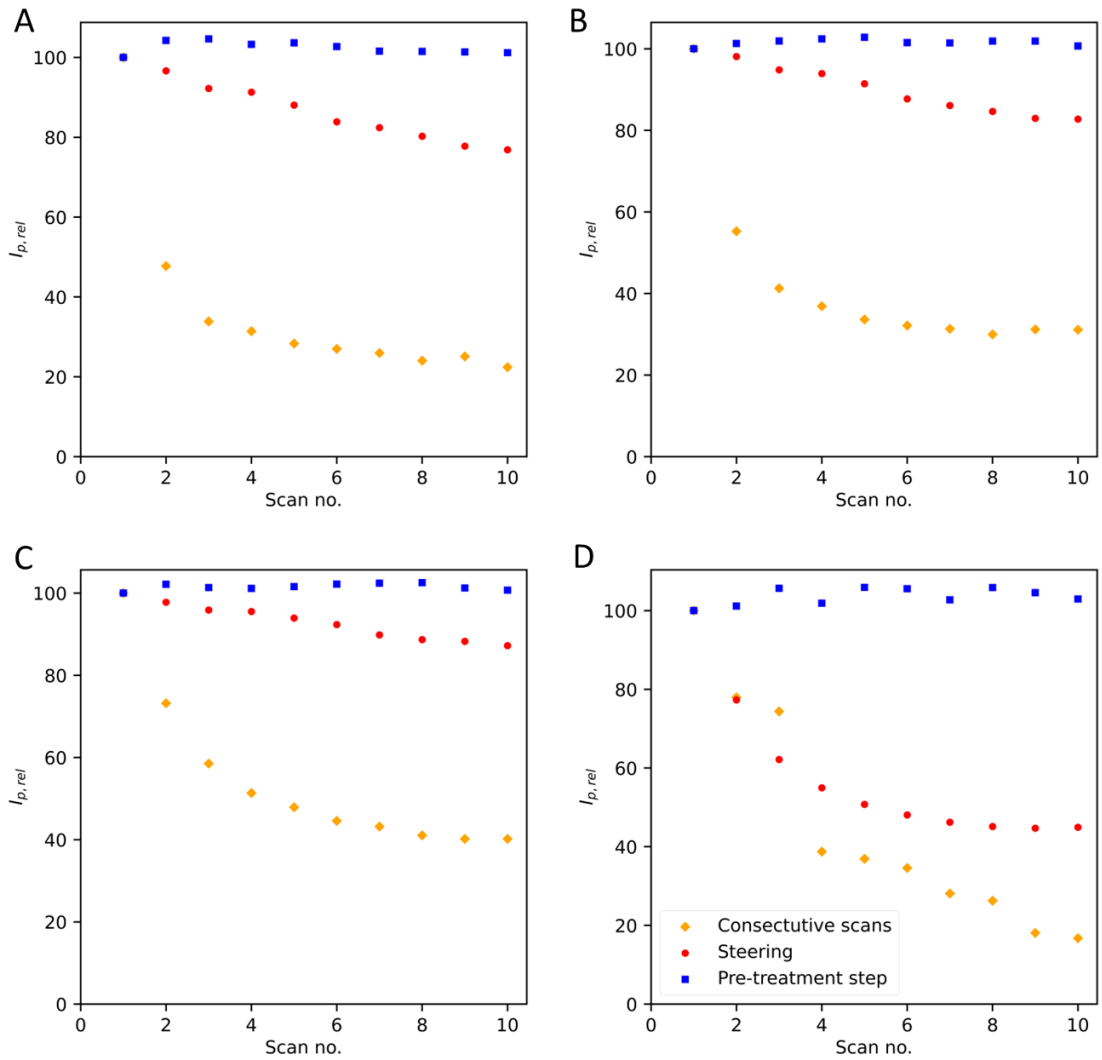


*Figure 5.9. Relative peak height ($I_{p,rel}$) of 100 µM VF in 0.1 M $H_2SO_4$ (pH 0.6) on O-BDD for (A) peak 1, (B) peak 2 and (C) peak 3. (D) 100 µM DVF in 0.1 M $H_2SO_4$ (pH 0.6) on H-BDD. Ten DPV measurements were acquired for three scenarios: consecutive scans, only steering the solution between scans and both steering and in-solution pre-treatment step between scans (30 s at +2 V for anodic pretreatment or -2 V for cathodic pretreatment).*

*Table 5.5. Intra-day stability of the VF and DVF signals for ten measurements recorded on the BDD electrodes, either consecutive scans, with stirring the solution between scans, or with stirring and in-solution pre-treatment step between scans (30 s at +2 V for anodic pretreatment or -2 V for cathodic pretreatment).*

| Peaks | Consecutive scans (decrease) | Stirring (decrease) | Pre-treatment step (RSD) |
|---|---|---|---|
| **100 µM VF in 0.1 M H2SO4 (pH 0.6) on O-BDD** | | | |
| Peak 1 | 77.4 | 23.2 | 1.4 % |
| Peak 2 | 68.9 | 17.2 | 0.8 % |
| Peak 3 | 59.8 | 12.8 | 0.8 % |
| **100 µM DVF in 0.1 M H2SO4 (pH 0.6) on H-BDD** | | | |
| DVF peak | 83.3 | 55.1 | 2.1 % |

### 5.2.6 Concentration study

The parameters optimized in section 5.2.4 were used to conduct the concentration study into VF and DVF. In Figure 5.10, DP voltammograms are depicted, and the resulting concentration-to-current curves are presented in Figure 5.11. These curves were utilized to determine the LOD and LOQ which are detailed in Table 5.6, alongside the curve's analytical parameters.

Both VF and DVF exhibit two linear ranges with similar behavior. Initially, the peak current increases from 2.5 µM up to a concentration of 75 µM for VF and 150 µM for DVF, followed by a gentler increase until stagnation of the peak current is reached.

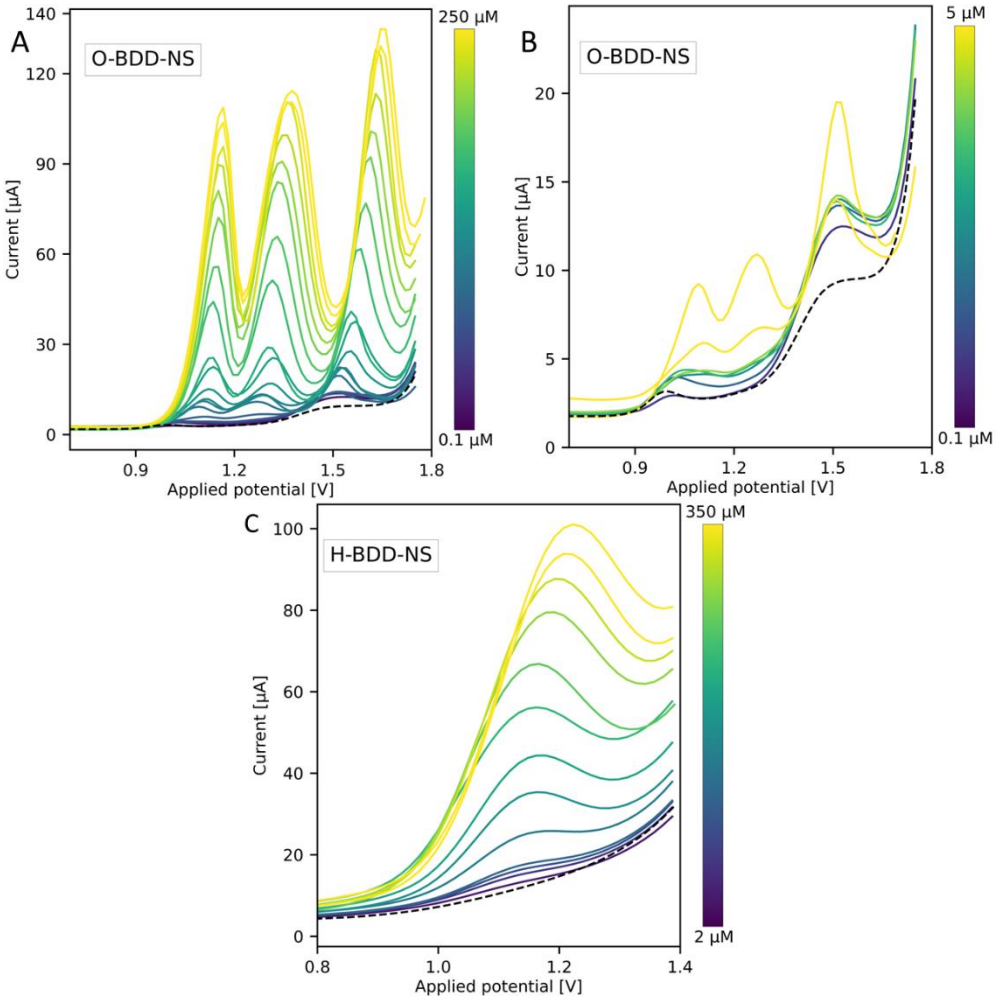


*Figure 5.10. The results of the DPV curves for the concentration study into of (A) VF in 0.1 M $H_2SO_4$ (pH 0.6) on O-BDD and (C) DVF in 0.1 M $H_2SO_4$ (pH 0.6) on H-BDD, with a zoom to the lower concentration levels for (B) VF.*

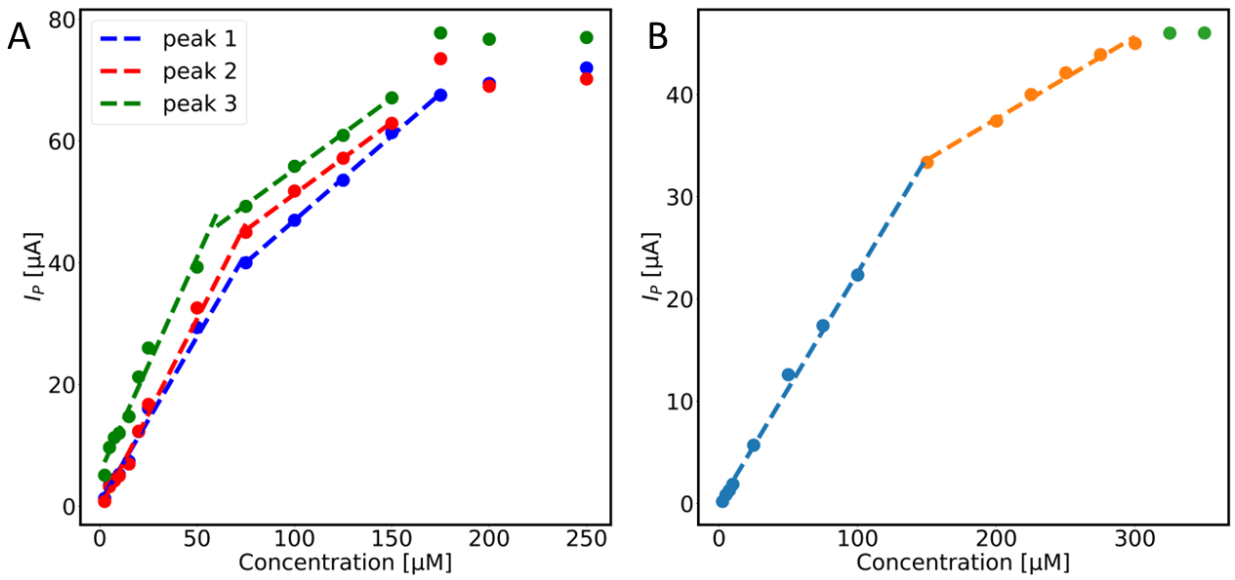


*Figure 5.10. The linear ranges found during the concentration study for (A) VF in 0.1 M $H_2SO_4$ (pH 0.6) on O-BDD and (B) DVF in 0.1 M $H_2SO_4$ (pH 0.6) on H-BDD.*

The results obtained for DVF on H-BDD are similar to the performance of carbon electrodes in prior studies as seen in Table 2.2. However, these electrodes had to undergo a complex modification and manufacturing procedure to prepare their surfaces. On the other hand, VF performed similar in the LOD to the MWCNTs/ CILE/carbon paste electrode [39] and MWCNT/RTIL [43] , and worse for the LOD and linear range than the other carbon electrode designs in Table 2.2. Nevertheless, these electrodes contain either catalysts or other surface depositions. Thus complicating reapplication of the surface characteristics after fouling, for the O-BDD electrode a simple in-solution anodic treatment of 30 seconds is sufficient.

In either case the BDD electrodes are capable of performing their purpose for VF and DVF sensing. As mentioned in the literature review, the concentration of VF and DVF in blood serum are 0.9 ± 0.5 µM and 0.95 ± 0.55 µM, respectively. This aligns with the LOQ of VF on O-BDD and DVF on H-BDD.

*Table 5.6. The analytical parameters from the concentration study results into VF in 0.1 M $H_2SO_4$ (pH 0.6) on O-BDD and DVF in 0.1 M $H_2SO_4$ (pH 0.6) on H-BDD.*

| | Linear range (µM) | Intercept (µA) | Slope (A/M) | R | LOD (µM) | LOQ (µM) |
|---|---|---|---|---|---|---|
| **O-BDD VF in 0.1 M $H_2SO_4$** | | | | | | |
| Peak 1 | 2.5-75 | 0.543 | 0.546 | 0.995 | 0.90 | 2.74 |
| | 75-175 | 19.183 | 0.278 | 0.999 | | |
| Peak 2 | 2.5-75 | -0.0485 | 0.625 | 0.997 | 0.29 | 0.89 |
| | 75-175 | 27.636 | 0.236 | 0.999 | | |
| Peak 3 | 2.5-75 | 5.467 | 0.708 | 0.988 | 0.14 | 0.42 |
| | 75-250 | 31.938 | 0.234 | 0.998 | | |
| **H-BDD DVF in 0.1 M $H_2SO_4$** | | | | | | |
| | 2.5-150 | -0.055 | 0.226 | 0.998 | 0.34 | 1.04 |
| | 150-275 | 21.573 | 0.080 | 0.995 | | |

### 5.2.7 Interference study

Figure 5.11 illustrates the effects of the investigated interferents on the VF and DVF peak currents at 10 µM concentrations. It is evident that the signals remain within tolerable ± 10 % levels for the following interferents: citric acid (50 -1000 µM in 0.1 M $H_2SO_4$), sucrose (5 mM in 0.1 M $H_2SO_4$) and glucose (5 mM in 0.1 M $H_2SO_4$). However, the ascorbic acid oxidation peak (partially) overlaps with DVF and VF peaks one and two. This results in a recoverable signal up to 100 µM ascorbic acid for DVF and combining the curves for VF peak one and two with the ascorbic acid peak at all concentrations . On the other hand, peak three from VF experiences minimal disturbance from ascorbic acid. Considering that ascorbic acid naturally occurs in the human body within the range from 10 µM to 115 µM [85], it allows DVF to remain unaffected for testing with human samples.

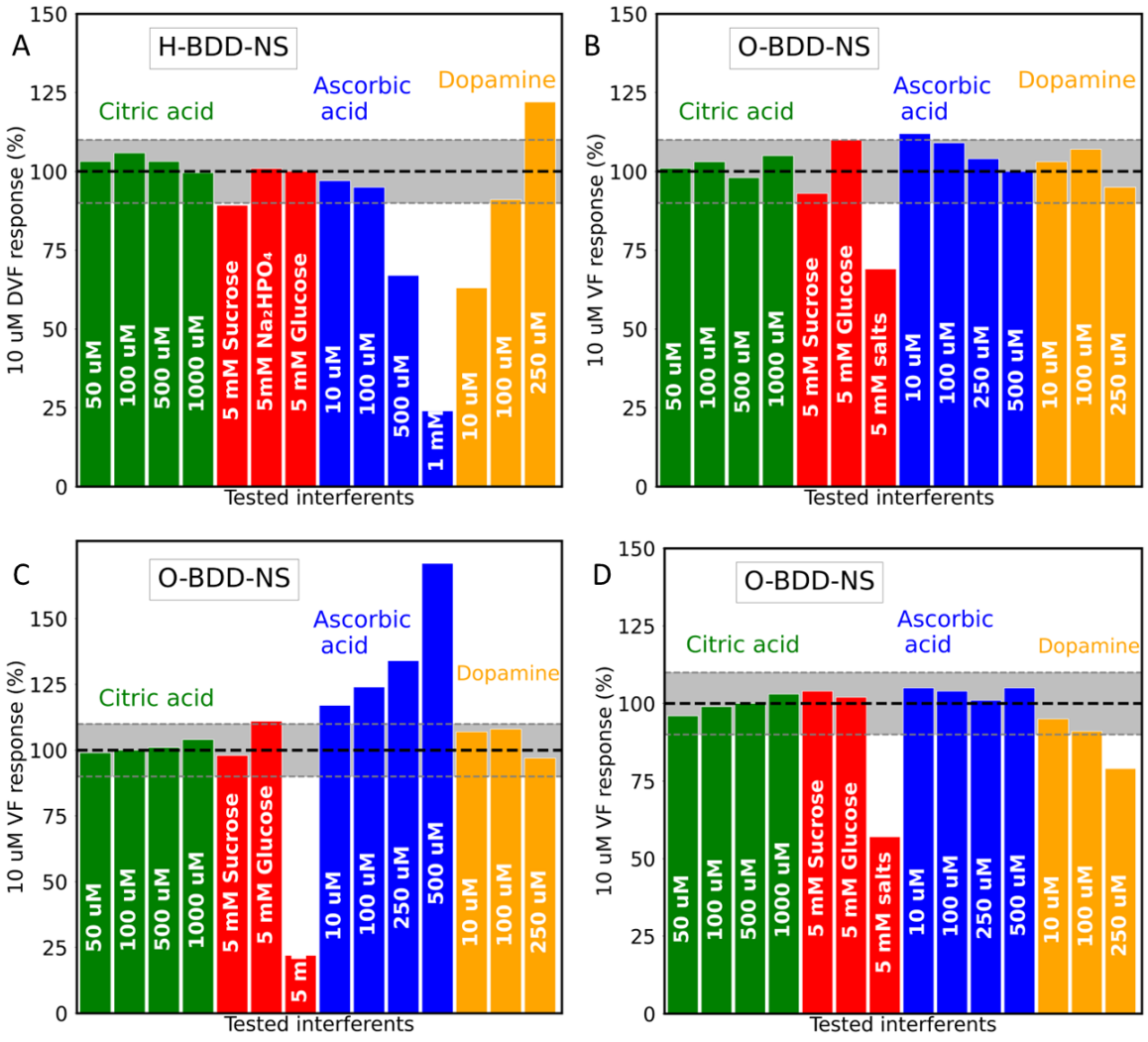


*Figure 5.11. The recovered peak heights of (A) 10 µM DVF in 0.1 M $H_2SO_4$ (pH 0.6) on H-BDD and 10 µM VF, peak (B) 1, (C) 2 and (D) 3, in 0.1 M $H_2SO_4$ (pH 0.6) on O-BDD after introduction of several interfering compounds*

Dopamine had a limited effect on VF detection. At concentrations of 250 µM the first major effects were noticed, well above the body's concentrations (< 0.1 µM). On the contrary, the peak for dopamine interferes with DVF measurements, leading to a lower recovered value of only 56 %. The inorganic salts had a negative effect on the performance of the electrode, with only $Na_2HPO_4$ among the tested salts

showing no interference with DVF results. For VF, recovery rates reach a maximum of 70 % (peak 1). Hence, it should be noted that detecting VF and DVF in human plasma, serum and urine samples will most likely incur difficulty due to the natural presence of salts. Even when electroanalysis in human samples includes dilution of the salts with the supporting electrolyte to adjust pH.

### 5.2.8 Investigation into synthetic urine, serum and river water

The selected results from VF and DVF testing in synthetic urine are displayed in Figure 5.12A, B, the other voltammograms (1:1 and 1:9 ratio) can be found in Appendix Figure A.7. Within the figure, an additional peak can be seen at ~+0.65 V for H-BDD surface and ~+0.85 V for H-BDD surfaces. This is a result of the presence of uric acid, as the salts and urea are non-electroactive and do not manifest directly in voltammetric curves. The results from the standard addition method are given in Table 5.7. In Appendix Figure A.10A and Figure A.11, the graphical quantification of the standard addition method for river water can be found. It is immediately apparent that both VF and DVF are sensitive to the interferents present. For DVF, although peaks are observable (See Figure 5.12A.), no recoverable concentration were found for the 1:1 and 1:4 ratios. For the 1:9 ratio a recovery rate of only 64% was achieved. VF performance is slightly better, with a recoverable concentrations identified for all ratios. Nevertheless, these recovery rates range from 40 % for the 1:9 ratio to 243 % for 1:4 the ratio. These results are undesirable, as it is not possible to accurately recover the original concentration.

*Table 5.7. The results of the found concentrations of VF on O-BDD and DVF on H-BDD in synthetic urine, synthetic serum and river water samples using the standard addition method.*

| Compound | Spiked(µM) | Found(µM) | | | Recovery (%) | | |
|---|---|---|---|---|---|---|---|
| **Synthetic urine** | | | | | | | |
| | | Peak 1 | Peak 2 | Peak 3 | Peak 1 | Peak 2 | Peak 3 |
| VF on O-BDD | 5 | 2.0 | 1.9 | 4.8 | 40 | 37.6 | 96 |
| | 10 | 12.4 | 12.3 | 23.5 | 124 | 123 | 235 |
| | 25 | 34.1 | 30.6 | 60.9 | 136 | 122 | 243 |
| DVF on H-BDD | 5 | 3.2 | | | 64 | | |
| | 10 | - | | | - | | |
| | 25 | - | | | - | | |
| **Synthetic serum** | | | | | | | |
| VF on O-BDD | 5 | 12.5 | 33.8 | 7.4 | 250 | 676 | 148 |
| | 10 | 47.6 | 76.1 | 30.6 | 476 | 761 | 306 |
| | 25 | 54.6 | 72.6 | 32.8 | 218 | 290 | 131 |
| DVF on H-BDD | 5 | - | | | - | | |
| | 10 | - | | | - | | |
| | 25 | - | | | - | | |
| **River Water** | | | | | | | |
| VF on O-BDD | 5 | 7.68 | 6.34 | 17.4 | 153 | 127 | 348 |
| | 10 | 14.3 | 13.7 | 22.4 | 143 | 137 | 224 |
| | 25 | 43.083 | 43.083 | 81.5 | 172 | 172 | 326 |
| DVF on H-BDD | 5 | 5.8 | | | 114 | | |
| | 10 | 2.9 | | | 29 | | |
| | 25 | 13.3 | | | 53.2 | | |

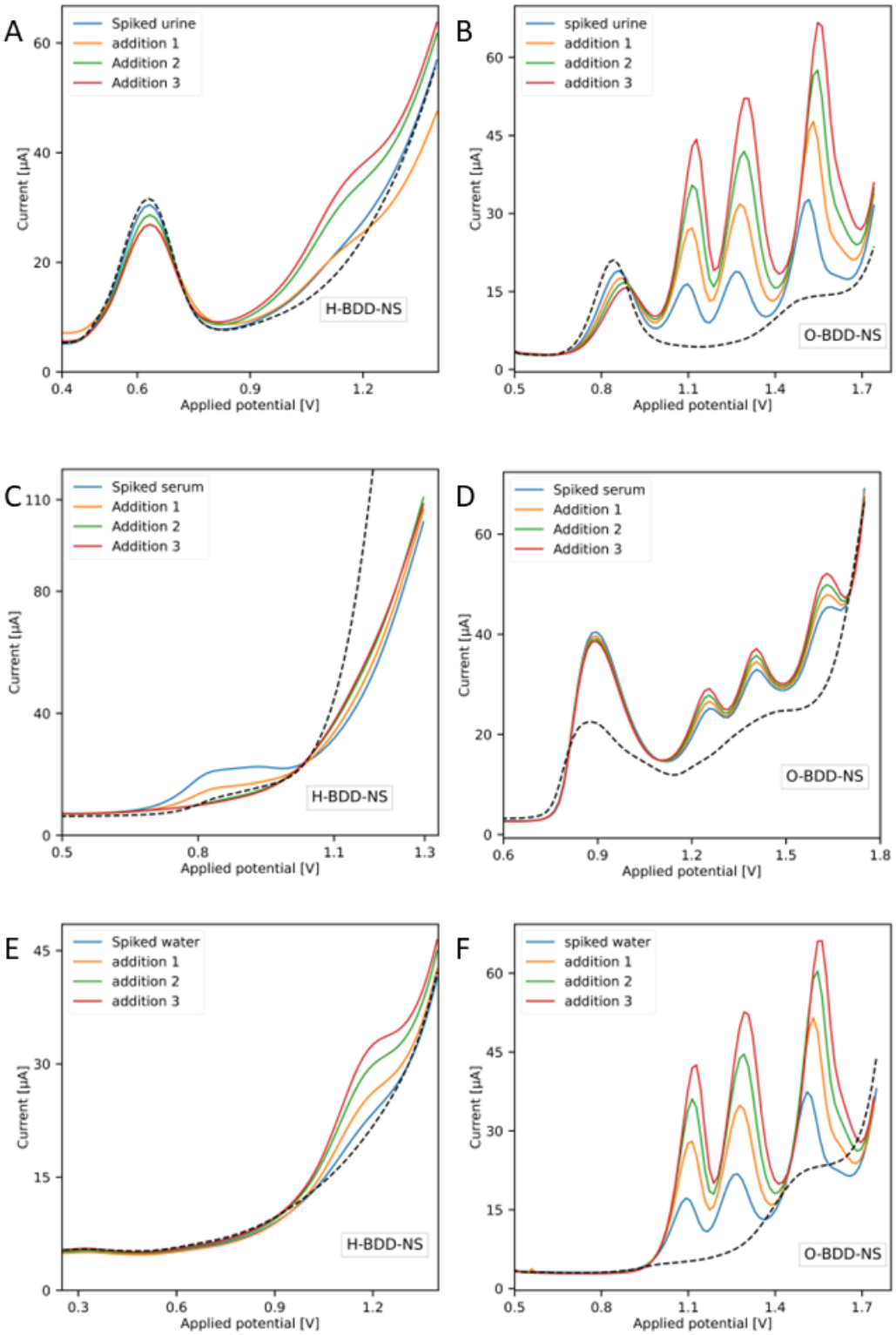


*Figure 5.12. DPV curves recorded in (A,B) synthetic urine, (C,D) synthetic serum and (E,F) river water samples diluted with 0.1 M $H_2SO_4$ (1:4) and spiked with (A,C,E) 10 µM DVF or (B,D,F) VF. Followed by three standard additions of 100 µL of 1 mM VF or DVF. The dashed lines correspond to the diluted urine, diluted serum or river samples.*

Furthermore, the obtained DPV of DVF and VF in synthetic serum (1:4 synthetic serum electrolyte ratio) can be found in Figure 5.12C, D, the other voltammograms (1:1 and 1:9 ratio) can be found in Appendix Figure A.8. In Appendix Figure A.12, the graphical quantification of the standard addition method for VF in synthetic serum can be found. For VF on a O-BDD surface a high intensity peak appeared around +0.9 V, this can be explained by the presence of electroactive and oxidizable amino acids present in the synthetic serum. On the H-BDD surface a far poorer developed peak is present, it is possible the negatively charged oxygen groups improve surface attraction and thus peak height for these reactions. However, it is more likely DVF and the serum contents interfere with another. In previous literature no dependency on surface termination was found for synthetic serum peak development [62]. This is also a possible explanation for the lack of peak development for DVF, as can be seen in Figure 5.12C and Appendix Figure A.8A, C. For VF the three peaks do develop in each ratio, however the recovered values are significantly higher than desired. The closest value found near the spiked value is for peak 3 in a 1:1 ratio, here a recovery of 131% occurred. It is therefore likely that matrix effects are occurring for VF as well. As each VF peak partially overlaps with each other, changes in one peak due to matrix effects will affect the others as well, this results in unpredictable results.

Figures 5.12E,F display the results for the detection of DVF and VF in river water (1:4 river water electrolyte ratio), the other voltammograms (1:1 and 1:9 ratio) can be found in Appendix Figure A.9. In Appendix Figure A.11B-D and Figure A.13, the graphical quantification of the standard addition method for river water can be found. On the voltammogram of the H-BDD surface, no discernible peaks are evident, while an observable peak at +1.5 V is visible for O-BDD surfaces. In the case of VF the found values exceed the spiked values and also acceptable levels. This is most likely due to matrix effects, wherein the VF will react with the contaminants in the river water, leading to a significantly higher recovery value ranging between 220% to 350%, as can be seen in Table 5.7. The recovery values for peak one and two are elevated as well ranging from 127% to 172%. For DVF, a lower recovery value is observed for the 1:1 and 1:4 ratio, attributable to the lower concentration of the electrolyte. As determined in the pH study, DVF is solely detectable at extremely acidic pH levels, and dilution with river water results in a higher pH. For the 1:9 ratio a higher recovery value of 114 % is found, most likely due to a sufficient concentration of the electrolyte. This is similar to the effect observed in VF, suggesting that the presence of river water increases perceived concentrations.

## 5.3 Inkjet printing

### 5.3.1 Printing the diamond pattern

Various patterns have been created based on a commercially available electrode chip from Metrohm DropSens and design concepts outlined by Ferrari et al. [69]. An overview of these designs can be found in Figure 5.13, with an overview of the patterns after BDD growth in Appendix Figure A.14. All designs are made to work with a standard DropSens connector cable. The wafers were pretreated by 12 seconds of oxygen plasma. Longer treatment would result in excessive wetting of the surface and shorter in a failure to for individual droplets to coalesce together.

To control the ejection of droplets, waveform tuning took place, a voltage wave was applied to fill and eject ink from the nozzles. The built-in-drop window of the PIXDRO printer allowed for real time tuning. For printing nanodiamond and silver nanoparticles, a voltage of 60 V was applied to the printhead. It became apparent that the waveform had to tuned differently during each printing occasion, as different moments required different parameters for droplet ejection and for prevention of satellite droplets. A

purge cycle was required for both nanodiamond every couple of prints as the nozzles will clog are prone to clogging.

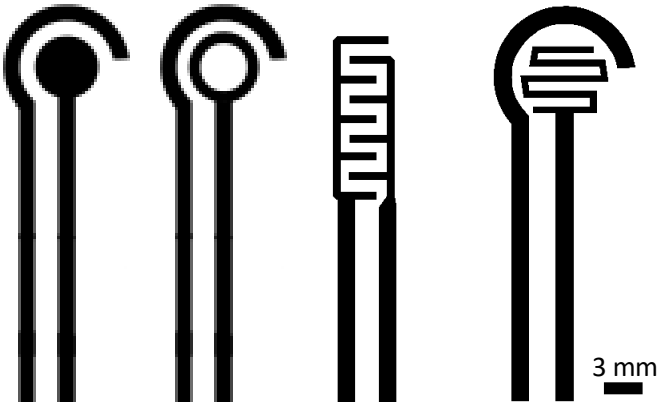


*Figure 5.13. The designs for the BDD WE and CE in black. The spacing between the CE and WE is 1.5 mm.*

.

## 5.3.2 Characteristics of the BDD growth

### *5.3.2.1 Diamond growth from Hasselt University*

In Figure 5.14B, a SEM image of one the Inkjet-printed electrodes after growth by Hasselt University is displayed. The growth appears to be homogeneous and no significant breaks in the deposited BDD layers are present. However, there seems to be spontaneous nucleation on areas where no nanodiamond particles were seeded. This is characterized by the white spots between the BDD film motifs, on these areas BDD is present and will interfere with the electrochemical sensing. The grain sizes of the microcrystalline structure range between 0.8 to 3 µm and have an average size of 1.3 µm. An instance of the crystal grain structure can be seen in Figure 5.14C, where the surface is marked by numerous individual crystal structures. To verify the degree of boron doping on the surface, Raman spectra of the BDD layers were obtained. In Figure 5.14A, an example of a typical graph for the inkjet-printed electrodes is presented. Utilizing the analysis tool developed by Mortet et al. [83], boron doping levels exceeding $2.2 \cdot 10^{21}$ $cm^{-3}$ were found, thus affirming the high boron content within the diamond material.

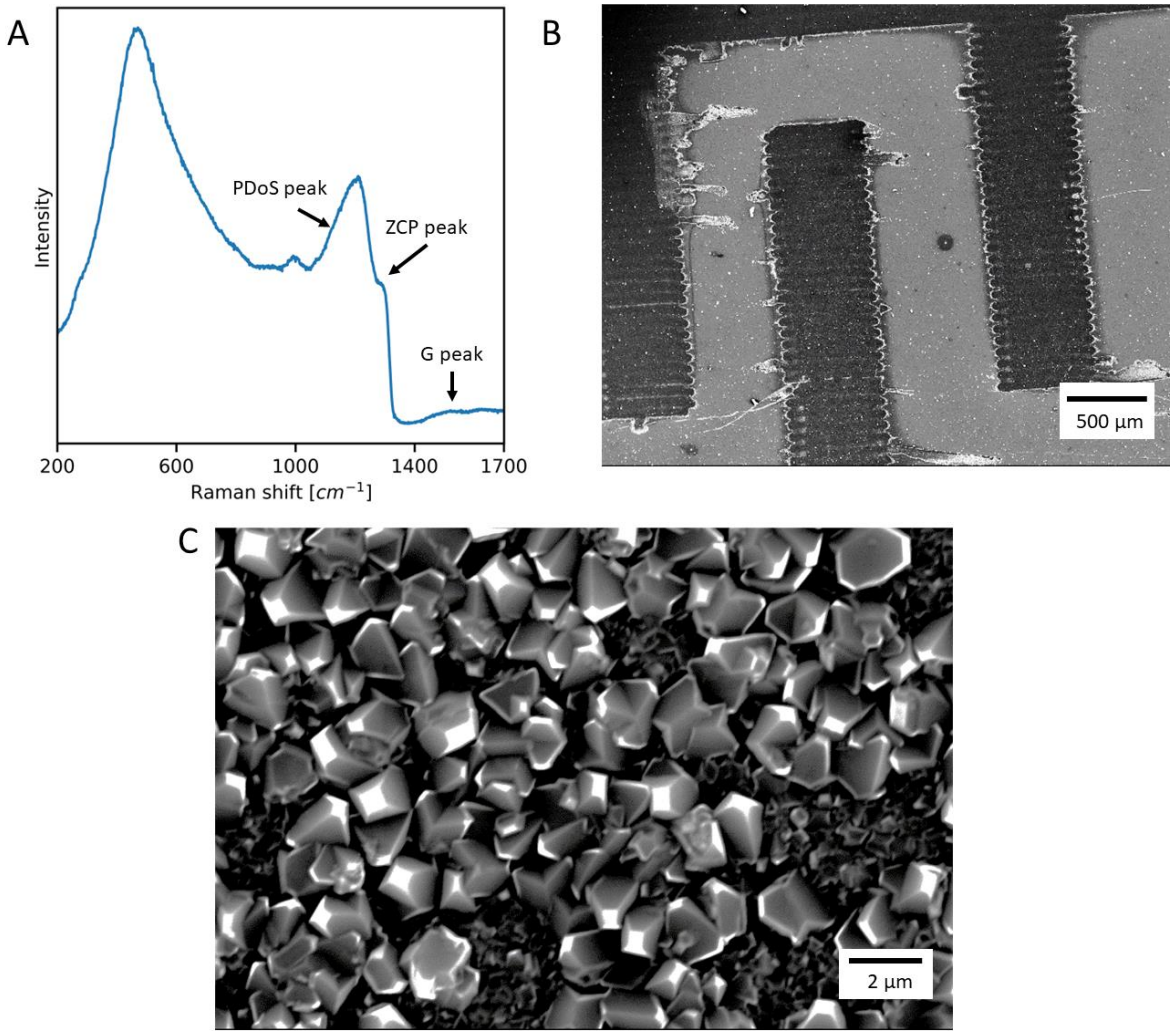


*Figure 5.14. (A) Raman spectrum of the BDD grown by MW-CVD at Hasselt University. (B) SEM image with an overview of the patterned BDD electrode. (C) SEM image of the assorted grain sizes present on the BDD electrodes.*

### *5.3.2.2 Diamond growth by Institute of Physics of the Czech Academy of Sciences*

Figure 5.15B displays a representative SEM image of one of the inkjet-printed electrodes after growth by Institute of Physics of the Czech Academy of Sciences. The growth of the BDD film is discontinuous, featuring several areas of inadequate growth. The print seems to be affected by the Marangoni effect, as evidenced by the visible print lines with poorly seeded areas connecting them. The absence of an uniform film impedes current flow, resulting in poor conductivity. It is likely that a higher seeding density could have prevented this issue, and one method to achieve that is by using a higher concentration of nanodiamond ink. In Figure 5.15C, it is also evident that the grains in the BDD film grown in Prague are sub-microcrystalline, with sizes ranging from 0.1 to 0.5 micrometers and an average size of 0.2 micrometers. In a manner similar to the previous section, Raman spectra were acquired for the BDD films of the electrode chips. Employing the Raman analysis tool of Mortet et al. [83] on the Raman spectral data shown in Figure 5.15A, the boron doping levels of the electrode chips were quantified. The film exhibited a high degree of boron doping, beyond $2.0 \cdot 10^{21}$ $cm^{-3}$ in boron content. These films are thus highly boron-doped diamond.

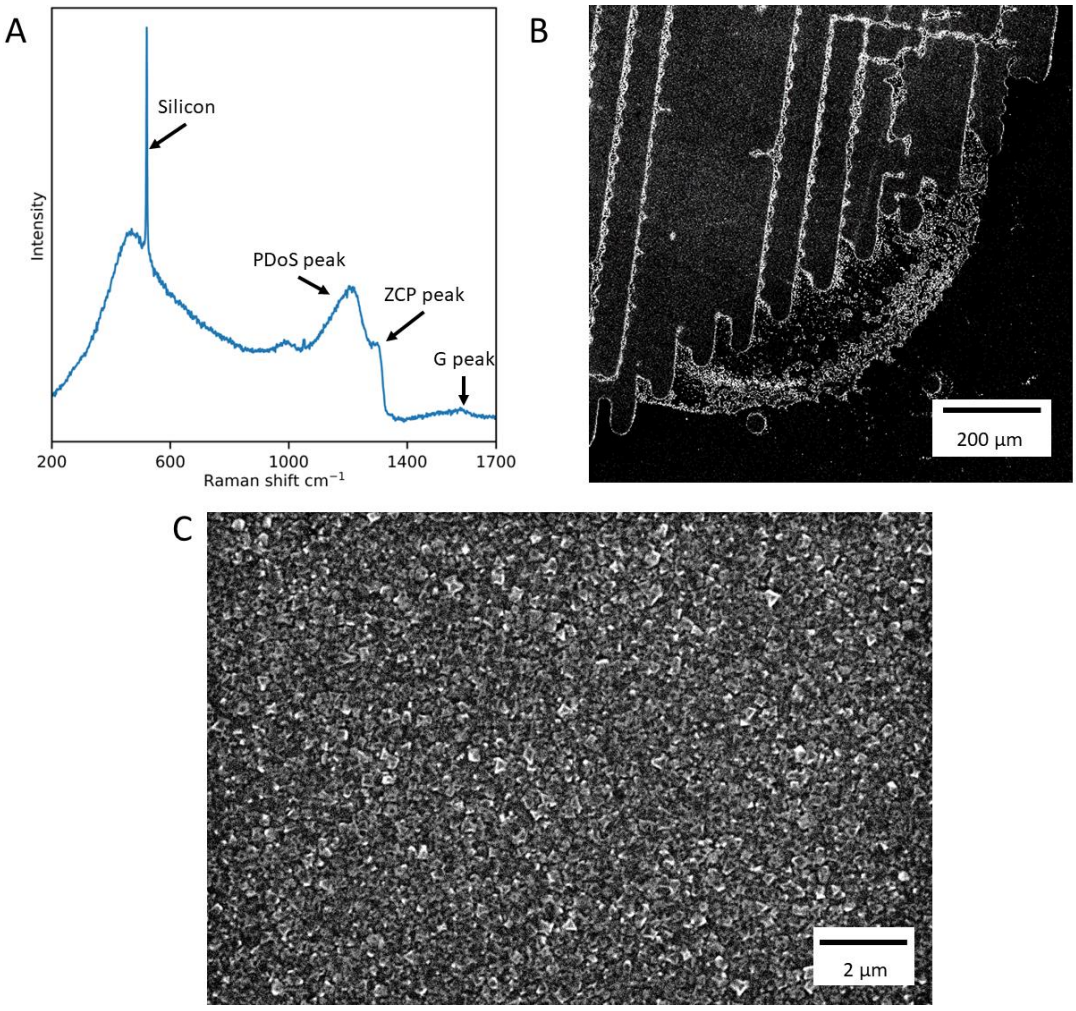


*Figure 5.15. (A) Raman spectrum of the BDD grown by MW-CVD at Institute of Physics in Prague. (B) SEM image with an overview of the patterned BDD electrode. (C) SEM image of the assorted grain sizes present on the BDD electrode.*

### 5.3.3 Printing of the silver reference electrode

An issue that afflicted the previous electrode chips fabricated by Liu et al. [14] is the inadequate adhesion of the silver reference electrode resulting in delamination during handling and voltammetric testing. The electrode was placed on a hotplate for 10 minutes at 300 °C to anneal to silver and enhance adhesion. In Figure 5.16A, an electrode chip featuring the silver reference electrode after ten minutes on a hotplate is presented. The metallic appearance clearly indicates a silver electrode. However, by examining the SEM image of Figure 5.17A the surface morphology is revealed. The electrode still exhibits small gaps between the silver, likely attributable to the locations where ink solvents were present during the drying process. To improve the adhesion a more extended annealing process is required. A longer heat treatment is required; however, excessive treatment will results in the transformation of silver into silver oxide. An example of a silver oxide reference electrode can be seen in Figure 5.16B, where the silver oxide is distinctly white as opposed to the metallic color of silver.

An alternative method is to transition from the hotplate to a vacuum oven, thereby reducing the presence of oxygen during the annealing process. Three different durations were investigated: 30 minutes, 60

minutes and 120 minutes in the vacuum oven at 250 ° C. The outcomes of these experiments can be seen in Figure 5.16C-E. After 120 minutes, the reference electrode exhibits a non-metallic white sheen to it and undergoes a conversion to silver oxide, this observation is further supported by the comparison of SEM images B-D in Figure 5.17. Namely, between the 10 min hotplate, 30 min oven and 60 min oven treatments the silver electrode appears amalgamate. However, a shift in the surface morphology occurs with 120 minute test, most likely due to the presence of silver oxide.

Both the 30 min oven and 60 min oven treatments were tested on their adhesion. Several CV scans were applied to the electrode chip and basic handling maneuvers were performed, such as insertion into the connector cable and placing it into the chip holder. During the scans no noticeable delamination took place for either chip. However, the 30 min treatment electrode would delaminate when exiting the connecter cable for the potentiostat. Therefore the 1 hour vacuum oven time is the recommended treatment method.

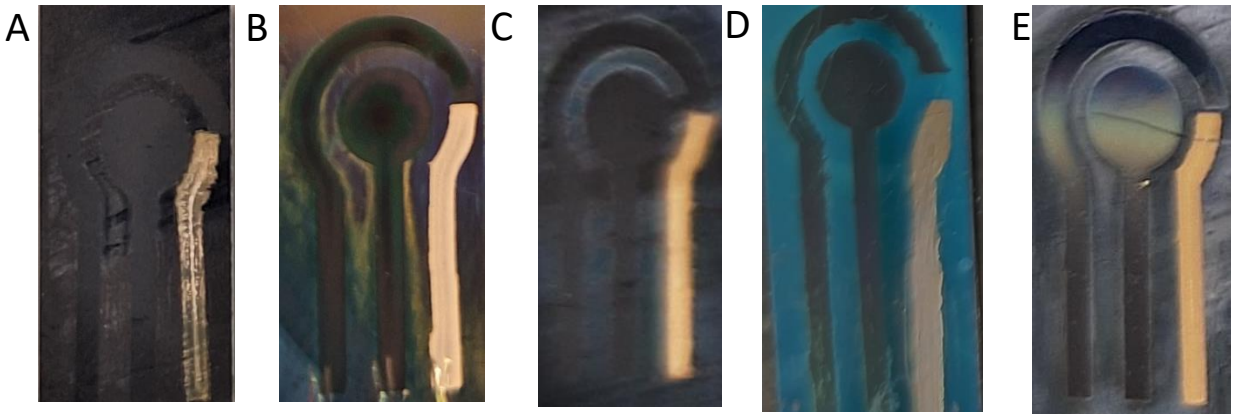


*Figure 5. 16. Images of the silver RE after (A) 10 min treatment at 300 °C on a hotplate, (B) 20 min treatment at 300 °C on a hotplate, (C) 30 min, (D) 60 min, (E) 120 min in a vacuum oven at 250 °C.*

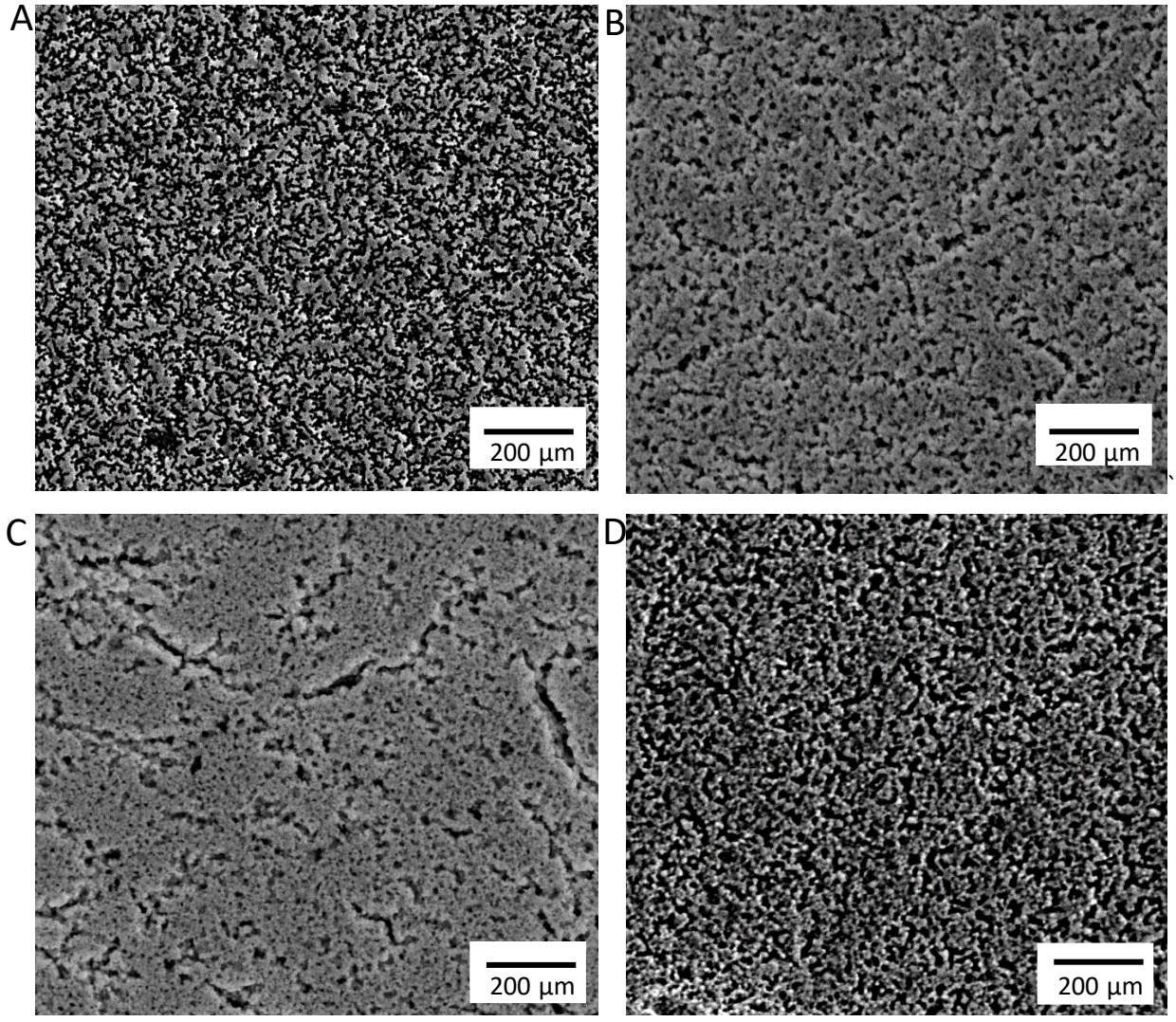


*Figure 5.17. Acquired SEM images of the silver reference after 10 min treatment at 300 °C on a hotplate (A), 30 min (B), 60 min (C) and 120 min (D) in a vacuum oven at 250 °C.*

### 5.3.4 Electrochemical characterization

To test the viability of the electrode chips for electrochemical detection of DVF and VF an electrochemical characterization had to occur. Sadly, during characterization it became apparent that the inkjet-printed electrodes would not be capable of performing the required voltammetric experiments. The results were mostly inconsistent and repeatability was poor, an example of a good result from a chip grown by Hasselt University is displayed in Figure 5.18. However, most cyclic voltammograms are similar to the curve in Figure 5.18B. This confirms the observations made in the SEM images in section 5.3.2, spontaneous nucleation on- and boron doping of the substrate has taken place. As a consequence, short circuits become prevalent.

A similar problem occurs for the electrode chips grown by the Institute of Physics of the Czech Academy of Sciences. This is best illustrated by the CVs of $[Ru(NH_3)_6]^{3+/2+}$ in $KNO_3$ presented in Figure 5.19. No useful data can be obtained from these measurements. A probable cause is the discontinuous film of the chips as seen in section 5.3.2. The current is unable to flow through the CE and WE leading to poor results.

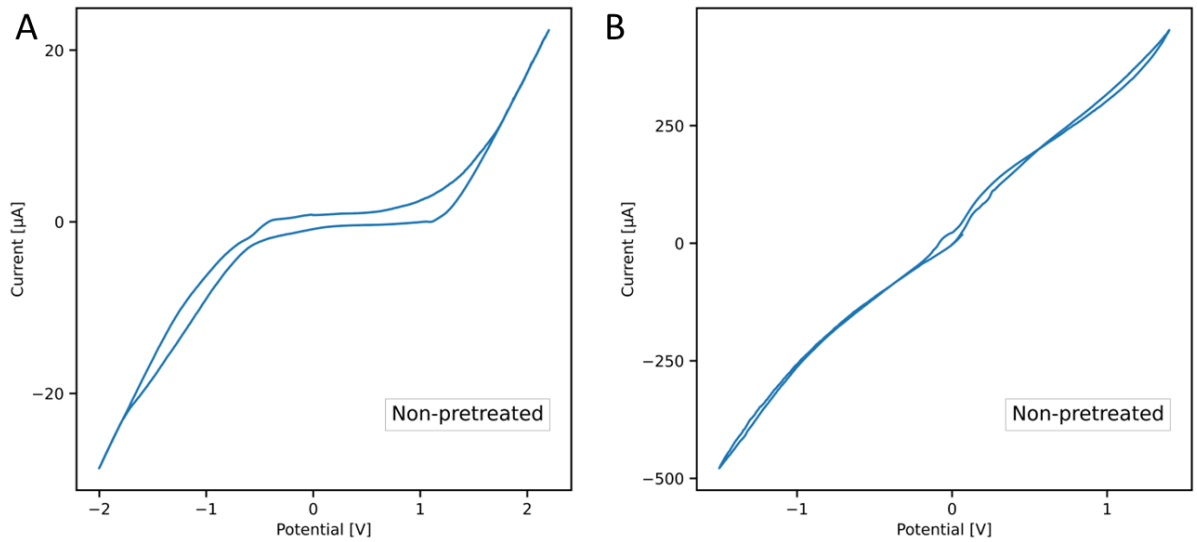


*Figure 5.18. Selected cyclic voltammograms recorded on the BDD electrode chips grown by MW-CVD at UHasselt. Electrolyte: 0.1 M $H_2SO_4$.*

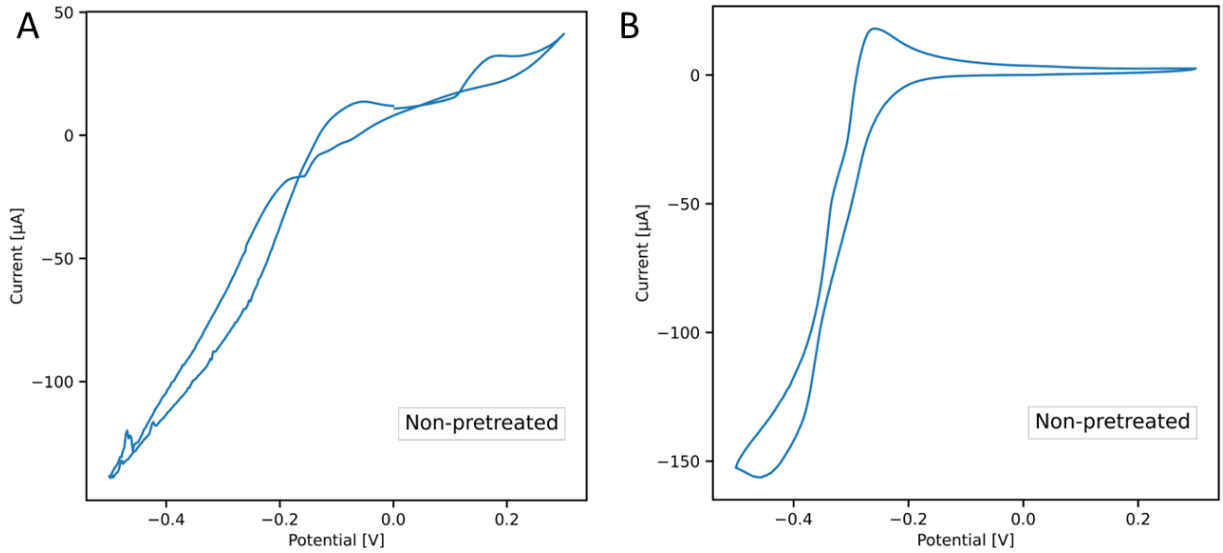


*Figure 5.19. Selected cyclic voltammograms recorded on the BDD electrode chips grown by MW-CVD at Institute of Physics of the Czech Academy of Sciences in Prague. 1 mM of $[Ru(NH_3)_6]^{3+/2+}$ in 0.1 M $KNO_3$ electrolyte.*

## 5.4 DropSens electrode

In this section, the DropSens (DP) electrode is characterized by SEM, Raman spectroscopy, and electrochemical tests. The boron doping, carbon content and effective surface area are determined. Then a comparison is made between the detection of DVF and VF under optimized conditions for the FSE and DP electrode, and in the end the LOD and LOQ of the DropSens are investigated.

### 5.4.1 DropSens electrode characterization

In Figure 5.20A the Raman spectra for the DP electrode can be found. Similar to the the previous BDD Raman spectra, a G-band indicating amorphous carbon and a peak for diamond are present. The diamond quality factor was 97.4% and determined by the following equation: $fq = 75\ I_d / 75\ I_d + \sum I_{nd}$, where $I_d$ is the Raman diamond peak area and and $I_{nd}$ the sum of the Raman $sp^2$ phase peak areas [82]. The tool developed by Mortet et al. [83] is employed to find a boron doping content larger than $2.0 \cdot 10^{20}$ atoms/cm$^3$, this corresponds to highly boron doped diamond.

The circular WE can be seen in Figure 5.20B, it is a continuous area and no major defects are present. The surface morphology has repeated spherical structures with are made out of small diamond crystals, as can be seen in Figure 5.20C. These grains are sub-microcrystalline with an average size of ~500 nm.

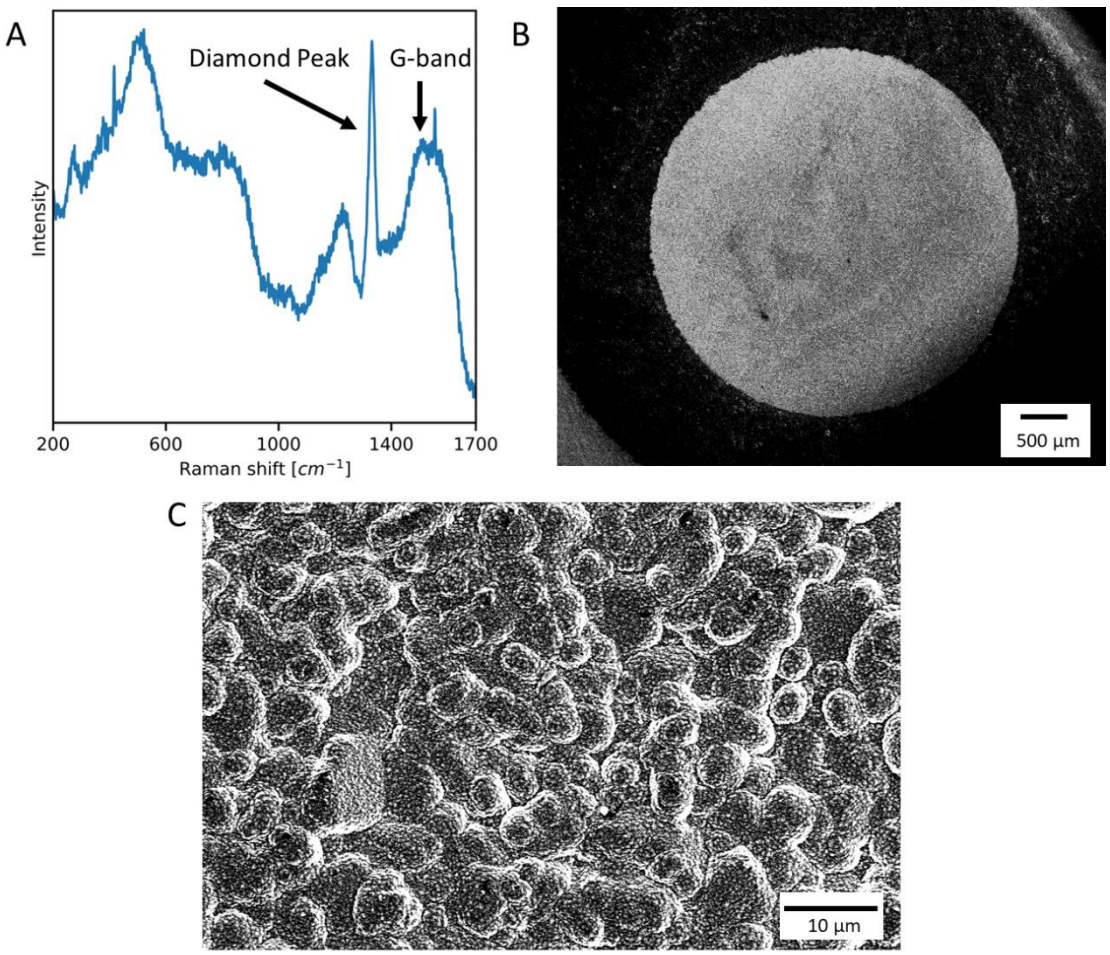


*Figure 5.20. (A) Raman spectrum of the DropSens electrode. (B) SEM image with an overview working electrode. (C) SEM image of the grain structure present on the working electrode.*

To be able to compare the FSE and DP electrode to each other the effective surface area has to be known. This allows for the normalization of the peak current values to peak current density values. To determine the effective surface area a scan rate study with $[Ru(NH_3)_6]^{3+/2+}$ was performed. The Randles-Sevcik equation is used to determine an effective surface area of 6.8 $mm^2$. The geometric surface area at 9.6 $mm^2$ is larger than the effective surface area. This could be explained by either the presence of contaminants of the electrode or the surface morphology. Contaminants would block active sites available for the reaction and thus reduce the effective surface area. The surface morphology of the electrode consists of uneven complex circular spheres stacked together. This can lead to a larger diffusion layer at some locations and they do not contribute as strongly to the measured current.

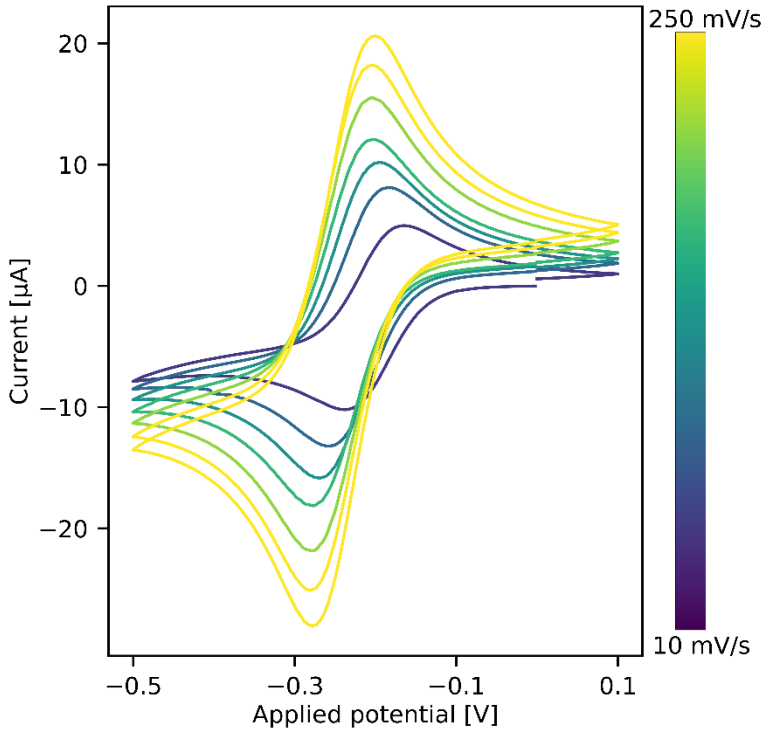


*Figure 5.21. Scan rate study results for the DropSens electrode with $[Ru(NH_3)_6]^{3+/2+}$ redox probe with scan rates varying in the range 10-250 mV/s.*

### 5.4.2 DropSens concentration test

A concentration study with optimized DPV parameters was performed for DVF and VF on the DP electrode. The resulting DPV curves can be found in Figure 5.22. These were used for the determination of the LOD and LOQ and these can be found in Table 5.8. For VF only two peaks are present, wherefor peak 1 can be observed until a concentration of 5 µM and peak 2 until a concentration of 10 µM. This translates to a LOD of 1.5 µM and a LOQ of 4.4 µM. For DVF a single peak is present. This peak is not very well developed and is only present until a concentration of 50 µM and has an LOD of 8.0 µM and a LOQ of 24.1 µM.

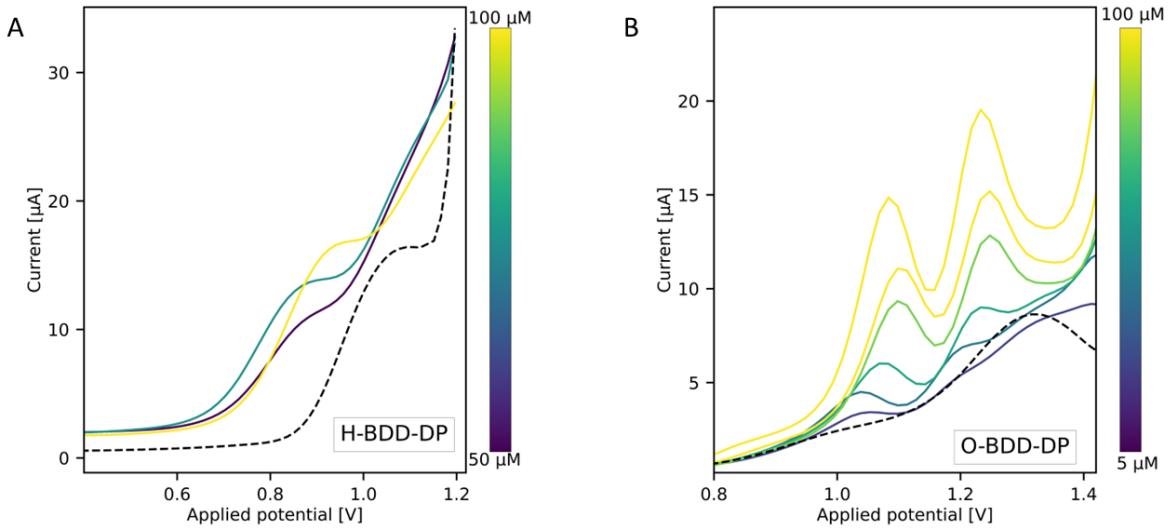


*Figure 5.22. The results of the DPV curves for the concentration study into of (A) VF in 0.1 M $H_2SO_4$ (pH 0.6) on O-BDD and (B) DVF in 0.1 M $H_2SO_4$ (pH 0.6) on H-BDD, with a zoom to the lower concentration levels for (B) VF.*

*Table 5.8. The results for the determination of the LOD and LOQ of VF in 0.1 M $H_2SO_4$ (pH 0.6) on O-BDD-DP and DVF in 0.1 M $H_2SO_4$ (pH 0.6) on H-BDD-DP.*

| | LOD (µM) | LOQ (µM) |
|---|---|---|
| O-BDD-NS VF in 0.1 M $H_2SO_4$, Peak 1 | 1.9 | 5.8 |
| O-BDD-NS VF in 0.1 M $H_2SO_4$, Peak 2 | 1.5 | 4.4 |
| H-BDD-NS DVF in 0.1 M $H_2SO_4$ | 8.0 | 24.1 |

### 5.4.3 Comparison between DropSens and free standing electrode

In Figure 5.23. an comparison between the peaks developed for 100 µM VF in 0.1 M $H_2SO_4$ (pH 0.6) on O-BDD and 100 µM DVF in 0.1 M $H_2SO_4$ (pH 0.6) on H-BDD on the FSE and DropSens electrode can be observed. For both DVF and VF the peaks are less well developed on the DP electrode and this results in lower peak current densities as well. In Table 5.9. the difference in peak current densities between the FSE and DropSens is given.

*Table 5.9. The comparison between the FSE and DropSens electrode for 100 µM VF in 0.1 M $H_2SO_4$ (pH 0.6) on O-BDD and 100 µM DVF in 0.1 M $H_2SO_4$ (pH 0.6) on H-BDD-DP.*

| **Peak** | **$I_p$ FSE (µA/cm$^2$)** | **$I_p$ DP (µA/cm$^2$)** | **Ratio (FSE/DP)** |
|---|---|---|---|
| VF peak 1 | 202.2 | 102.9 | 1.97 |
| VF peak 2 | 223.3 | 54.7 | 4.08 |
| DVF | 96.6 | 42.6 | 2.26 |

The poorer peak development is also represented in the worse LOD and LOQ for the DP electrode determined in Section 5.4.2. The LOD and LOQ for VF are factor ten higher for DP electrode compared to the FSE electrode. This is in part due to the lack of peak 3 for the DropSens electrode, which has the lowest LOD for the FSE electrode. However, even for peak 2 it is a factor of 5 difference. For DVF, the LOD and LOQ are 23 times as large for the DP electrode compared to the FSE.

There are two main difference between the nucleation side of the FSE and the DP electrode which could explain this difference: the surface morphology and the electrode size. The boron doping content is also higher for the DP electrode, but this should not cause a poorer developed peak. The carbon content for both electrodes is similar and will thus have a negligible effect on the performance. The surface morphology and the electrode size can have an effect on the diffusion profile of DVF and VF. A thicker layer could be present on the surface and the DP electrode could thus have a poorer developed peak

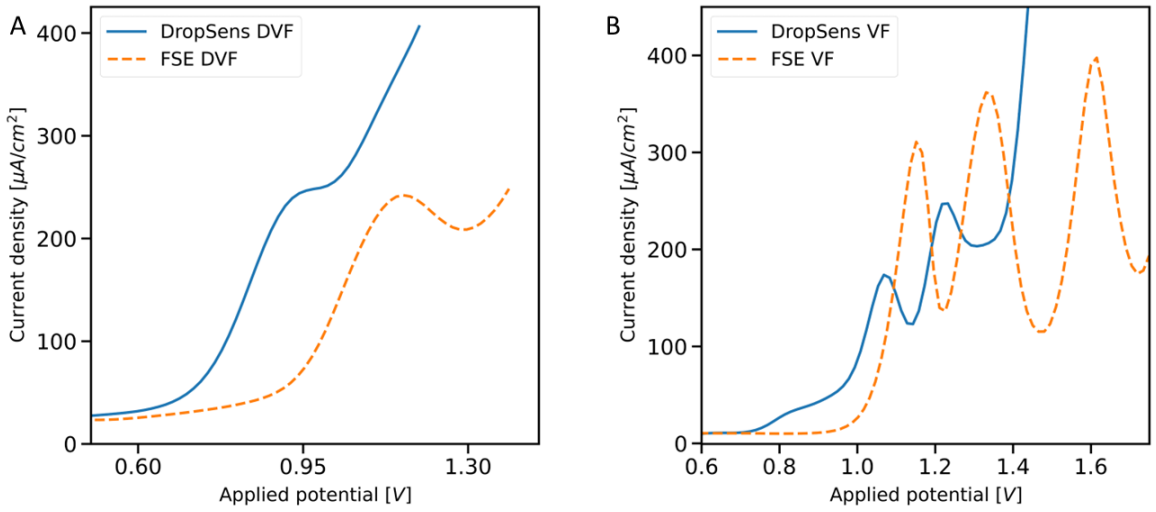


*Figure 5.23. The Comparison for the DPV curves for (A) 100 µM DVF in 0.1 M $H_2SO_4$ (pH 0.6) on H-BDD and (C) 100 µM VF in 0.1 M $H_2SO_4$ (pH 0.6) on O-BDD.*

# 6 Conclusions and recommendations

## 6.1 Conclusions

The goal of this master thesis work was twofold, namely to create an optimized detection method for the pharmaceutical compounds VF and DVF on BDD electrodes and to apply this method to the detection of VF and DVF on a three-electrode chip. The project was divided into two parts to achieve this goal: a voltammetric study of VF and DVF on a robust and well-established free-standing BDD electrode (FSE) for the creation of the optimized detection method and the fabrication of a three-electrode chip using inkjet printing techniques which took place concurrently. The detection results following the optimized method on the free-standing BDD electrode and a commercial three-electrode chip were compared.

For the FSE, the nucleation and growth sides were investigated and several observations were made. SEM imaging and Raman spectroscopy revealed marked differences in the surface morphology and composition. The growth side had significantly larger average grain sizes (~105 µm) compared to the nucleation side (~1.3 µm). This was mainly due to nucleation being the start of the diamond growth on the nanodiamond seeds and the growth side being the developed side of the diamond growth. These differences in grain sizes had a noticeable effect on the $sp^3/sp^2$ carbon ratio as well. The nucleation side had a significant concentration of $sp^2$ carbon whereas the growth side had a negligible amount. Nevertheless, analysis revealed no major difference in the boron dopant contents of the two different surfaces. Their electrochemical properties were investigated as well. The nucleation side had higher peak currents for the investigated redox markers whereas the low boron doping level in combination with the higher $sp^2$ carbon content led to a lower background current.

The voltammetric study involving VF and DVF detection on the FSE was done to create an optimized detection method and investigate the viability for practical applications. The pH study revealed the optimized electrolyte conditions and electrode surface termination, i.e. 0.1 M $H_2SO_4$ (pH 0.6) for both DVF and VF, and O-BDD for VF and H-BDD for DVF. The oxidative reaction of VF was expressed by three visible DPV peaks, and the reaction of DVF by a single peak. A scan rate study revealed that all reaction processes are diffusion controlled. Although testing revealed satisfactory analytical figures for DVF and VF monitoring, additional tests with inorganic salts, synthetic urine and river water identified issues with accurate recovery of spiked values. This would complicate the use in practical and clinical environments.

The successful creation of BDD three-electrode chips using inkjet printing was not achieved in this study. The printing process itself was a success, the seeding of the substrates with a nanodiamond particle ink was successful. However, both attempts at BDD film growth in a CVD reactor resulted in failures. High boron doping levels (> $10^{21}$ $cm^{-3}$) and complex patterned growth did happen, yet in the first growth session taken place at Hasselt University (Belgium) unwanted doping of the substrate led to short-circuiting, whereas the second attempt at the Institute of Physics of the Czech Academy of Sciences (Czech Republic) suffered from underdeveloped sections of BDD growth, most likely due to Marangoni flow and insufficient seeding. This led to poor current flow in the electrodes resulting in problems with the voltammetric graphs. Though, an improvement of the silver reference electrode was successfully achieved by utilizing one hour of post-processing treatment inside a vacuum oven.

The comparison of VF and DVF detection between the commercial DropSens electrode chip and the FSE revealed a worse performance for the DropSens chip. This chip had significantly higher LOD and LOQ under the optimized parameters. This was likely due to the difference in surface morphology and surface

area between the two electrodes. This could have an effect on the diffusion pattern and thus limit the reaction on the DropSens electrode.

## 6.2 Recommendations for future research

An optimized DPV method for the detection of DVF and VF on BDD electrodes proved to be promising for the detection of both compounds. The satisfactory analytical figures show that the method is a potential mean for the testing in physiological fluids, however the large effects of interferents show there still is room for improvement. Similarly, further optimization for the entire bottom-up fabrication process of inkjet-printing of BDD electrodes is required. Therefore, several recommendations for future research are detailed:

- As further selectivity of the surface would most likely improve the detection of VF and DVF in interfering compounds, the use of different types of surface modifications could be investigated. This could involve nano-modifiers, which have a catalytic effect, or laser etching to create nanopillars to enhance the surface area of the electrode. These procedures would most likely also improve the detection limit of the sensors. This is required for detection in environmental samples as these are mostly in nM concentration levels and thus not detectable with the current method.

- The initial tests on the growth and nucleation surfaces revealed the effect of $sp^2$ carbon levels. A more extensive investigation into how different $sp^2$ carbon contents can influence the detection of VF and DVF is of interest. This can be combined with an investigation into the effects of boron doping, where the interplay between boron levels and $sp^2$ carbon content is investigated.

- BDD can be advantageously used for the degradation of pollutants, while the pollution of VF and DVF in nature is an active problem. Therefore, research into the use of electrochemical advanced oxidation processes for their degradation on BDD is an intriguing direction of novel research. This could be combined into a single platform for both detection and degradation of the compounds, where inkjet printing might facilitate the fabrication of the required BDD electrode chips regarding the detection.

- The BDD growth of the inkjet seeded electrode designs made clear the importance of seed density. Different levels of diamond ink concentrations have to be studied to create a proper method for a successful growth of uniform thin-film BDD. The effects of varying diamond ink concentration on the quality and morphology of the BDD is an important consideration as well. A combination with a systematic BDD growth study using the in-house CVD reactor would be ideal as this would allow for tuning the seeding/growth parameters to desired electrode characteristics.

- Further diamond ink optimization could ease the electrode manufacturing process. Clogging of the inkjet nozzles and variable wettability of the substrate surface lead to delays in the printing process. By further optimizing the ink for increased wettability with surfactants or different solvents could improve performance. The use of a different nozzle less prone to clogging could also be a solution.

- Micro electrode arrays are grids of tiny micro electrodes used to record electrochemical current signals. They have several advantages over classical electrodes, such as high spatial resolution. By further minimizing droplet size and increasing printing resolution, inkjet printing could be ideal for their manufacturing process. This would require further tuning of the print parameters and

ink properties. It would also be helpful to remove the oxygen plasma treatment step, as this is an inconsistent process for short treatment durations.

.

# 7 Bibliography


1. Liu Q, He H, Yang J, et al (2020) Changes in the global burden of depression from 1990 to 2017: Findings from the Global Burden of Disease study. Journal of Psychiatric Research 126:134–140. https://doi.org/10.1016/j.jpsychires.2019.08.002

2. Hoefler R, Tiguman GMB, Galvão TF, et al (2023) Trends in sales of antidepressants in Brazil from 2014 to 2020: A time trend analysis with joinpoint regression. Journal of Affective Disorders 323:213–218. https://doi.org/10.1016/j.jad.2022.11.069

3. PubChem Venlafaxine. In: National Library of Medicine. https://pubchem-ncbi-nlm-nih-gov.tudelft.idm.oclc.org/compound/5656. Accessed 27 Jan 2023

4. PubChem Desvenlafaxine. In: National Library of Medicine. https://pubchem-ncbi-nlm-nih-gov.tudelft.idm.oclc.org/compound/125017. Accessed 27 Jan 2023

5. Wilkinson JL, Boxall ABA, Kolpin DW, et al (2022) Pharmaceutical pollution of the world's rivers. Proceedings of the National Academy of Sciences 119:e2113947119. https://doi.org/10.1073/pnas.2113947119

6. Sehonova P, Svobodova Z, Dolezelova P, et al (2018) Effects of waterborne antidepressants on non-target animals living in the aquatic environment: A review. Science of The Total Environment 631–632:789–794. https://doi.org/10.1016/j.scitotenv.2018.03.076

7. Gomez Cortes L, Joint Research Centre (European Commission), Marinov D, et al (2020) Selection of substances for the 3rd Watch List under the Water Framework Directive. Publications Office of the European Union, LU

8. Dobrzhinetskaya LF (2012) Microdiamonds — Frontier of ultrahigh-pressure metamorphism: A review. Gondwana Research 21:207–223. https://doi.org/10.1016/j.gr.2011.07.014

9. Handschuh-Wang S, Wang T, Tang Y (2021) Ultrathin Diamond Nanofilms—Development, Challenges, and Applications. Small 17:2007529. https://doi.org/10.1002/smll.202007529

10. Heard DM, Lennox AJJ (2020) Electrode Materials in Modern Organic Electrochemistry. Angew Chem Int Ed Engl 59:18866–18884. https://doi.org/10.1002/anie.202005745

11. Hicks M-L, Pakpour-Tabrizi AC, Jackman RB (2019) Polishing, preparation and patterning of diamond for device applications. Diamond and Related Materials 97:107424. https://doi.org/10.1016/j.diamond.2019.05.010

12. Domonkos M, Demo P, Kromka A (2020) Nanosphere Lithography for Structuring Polycrystalline Diamond Films. Crystals 10:118. https://doi.org/10.3390/cryst10020118

13. Ali B, Litvinyuk IV, Rybachuk M (2021) Femtosecond laser micromachining of diamond: Current research status, applications and challenges. Carbon 179:209–226. https://doi.org/10.1016/j.carbon.2021.04.025

14. Liu Z, Baluchová S, Buijnsters JG, et al Inkjet Printing Manufactured Boron-Doped Diamond Chip Electrodes for Electrochemical Sensing Purposes. [submitted for publication]

15. Švorc L, Tomčík P, Svítková J, et al (2012) Voltammetric determination of caffeine in beverage samples on bare boron-doped diamond electrode. Food Chemistry 135:1198–1204. https://doi.org/10.1016/j.foodchem.2012.05.052

16. Pierpaoli M, Dettlaff A, Szopińska M, et al (2021) Simultaneous opto-electrochemical monitoring of carbamazepine and its electro-oxidation by-products in wastewater. Journal of Hazardous Materials 419:126509. https://doi.org/10.1016/j.jhazmat.2021.126509

17. Yiğit A, Yardım Y, Şentürk Z (2016) Voltammetric Sensor Based on Boron-Doped Diamond Electrode for Simultaneous Determination of Paracetamol, Caffeine, and Aspirin in Pharmaceutical Formulations. IEEE Sensors Journal 16:1674–1680. https://doi.org/10.1109/JSEN.2015.2503436

18. Chaabene R, Khannous L, Samet Y (2022) Electrochemical degradation of aqueous metformin at boron-doped diamond electrode: kinetic study and phytotoxicity tests. Int J Environ Sci Technol. https://doi.org/10.1007/s13762-022-04325-2

19. Švorc Ľ, Stanković DM, Kalcher K (2014) Boron-doped diamond electrochemical sensor for sensitive determination of nicotine in tobacco products and anti-smoking pharmaceuticals. Diamond and Related Materials 42:1–7. https://doi.org/10.1016/j.diamond.2013.11.012

20. Güngör Ö (2022) Determination of naproxen by using differential pulse voltammetry with poly (aniline-2-sulfonic acid) modified boron doped diamond electrode. Macedonian Journal of Chemistry and Chemical Engineering 41:11–20. https://doi.org/10.20450/mjcce.2022.2381

21. Souza CD, Braga OC, Vieira IC, Spinelli A (2008) Electroanalytical determination of sulfadiazine and sulfamethoxazole in pharmaceuticals using a boron-doped diamond electrode. Sensors and Actuators B: Chemical 135:66–73. https://doi.org/10.1016/j.snb.2008.07.020

22. Alecrim MF, Oliveira FM, Guedes TJ, et al (2016) Electrochemical behavior of the cotinine at a boron-doped diamond electrode and its determination in saliva by multiple-pulse amperometry in an FIA system. Electrochimica Acta 222:331–337. https://doi.org/10.1016/j.electacta.2016.10.177

23. Pınar PT, Yardım Y, Şentürk Z (2020) Individual and simultaneous electroanalytical sensing of epinephrine and lidocaine using an anodically pretreated boron-doped diamond electrode by square-wave voltammetry. Diamond and Related Materials 101:107649. https://doi.org/10.1016/j.diamond.2019.107649

24. Švorc Ľ, Sochr J, Svítková J, et al (2013) Rapid and sensitive electrochemical determination of codeine in pharmaceutical formulations and human urine using a boron-doped diamond film electrode. Electrochimica Acta 87:503–510. https://doi.org/10.1016/j.electacta.2012.09.111

25. Scremin J, Sartori ER (2018) Simultaneous determination of nifedipine and atenolol in combined dosage forms using a boron-doped diamond electrode with differential pulse voltammetry. Can J Chem 96:1–7. https://doi.org/10.1139/cjc-2017-0302

26. Sanghavi BJ, Srivastava AK (2011) Adsorptive stripping differential pulse voltammetric determination of venlafaxine and desvenlafaxine employing Nafion–carbon nanotube composite glassy carbon electrode. Electrochimica Acta 56:4188–4196. https://doi.org/10.1016/j.electacta.2011.01.097

27. TGA eBS - Product and Consumer Medicine Information Licence. https://www.ebs.tga.gov.au/ebs/picmi/picmirepository.nsf/pdf?OpenAgent&id=CP-2010-PI-04889-3

28. Wilkinson JL, Boxall ABA, Kolpin DW (2019) A Novel Method to Characterise Levels of Pharmaceutical Pollution in Large-Scale Aquatic Monitoring Campaigns. Applied Sciences 9:1368. https://doi.org/10.3390/app9071368

29. Tiwari B, Ouarda Y, Drogui P, et al (2021) Fate of Pharmaceuticals in a Submerged Membrane Bioreactor Treating Hospital Wastewater. Frontiers in Water 3:. https://doi.org/10.3389/frwa.2021.730479

30. Kulandaivelu J, Choi PM, Shrestha S, et al (2020) Assessing the removal of organic micropollutants from wastewater by discharging drinking water sludge to sewers. Water Research 181:115945. https://doi.org/10.1016/j.watres.2020.115945

31. Silva A, Martinho S, Stawinski W, et al (2018) Application of vermiculite-derived sustainable adsorbents for removal of venlafaxine. Environ Sci Pollut Res 25:17066–17076. https://doi.org/10.1007/s11356-018-1869-6

32. Stadler LB, Su L, Moline CJ, et al (2015) Effect of redox conditions on pharmaceutical loss during biological wastewater treatment using sequencing batch reactors. J Hazard Mater 282:106–115. https://doi.org/10.1016/j.jhazmat.2014.08.002

33. Hiemke C, Baumann P, Bergemann N, et al (2011) AGNP Consensus Guidelines for Therapeutic Drug Monitoring in Psychiatry: Update 2011. Pharmacopsychiatry 44:195–235. https://doi.org/10.1055/s-0031-1286287

34. Rúa-Gómez PC, Püttmann W (2012) Impact of wastewater treatment plant discharge of lidocaine, tramadol, venlafaxine and their metabolites on the quality of surface waters and groundwater. J Environ Monit 14:1391–1399. https://doi.org/10.1039/C2EM10950F

35. Tran TTT, Nguyen DM, Dao AQ, et al (2022) A state-of-the-art review on the nanomaterial-based sensor for detection of venlafaxine. Chemosphere 297:134116. https://doi.org/10.1016/j.chemosphere.2022.134116

36. Rizk M, Taha EA, El-Alamin MMA, et al (2018) Highly Sensitive Carbon Based Sensors Using Zinc Oxide Nanoparticles Immobilized Multiwalled Carbon Nanotubes for Simultaneous Determination of Desvenlafaxine Succinate and Clonazepam. J Electrochem Soc 165:H333. https://doi.org/10.1149/2.0551807jes

37. Bajaber MA, Kamel AH (2022) All-Solid State Potentiometric Sensors for Desvenlafaxine Detection Using Biomimetic Imprinted Polymers as Recognition Receptors. Polymers 14:4814. https://doi.org/10.3390/polym14224814

38. Mohammadzadeh Jahani P, Akbari Javar H, Mahmoudi-Moghaddam H (2021) A new electrochemical sensor based on Europium-doped NiO nanocomposite for detection of venlafaxine. Measurement 173:108616. https://doi.org/10.1016/j.measurement.2020.108616

39. Eslami E, Farjami F (2018) Voltammetric Determination of Venlafaxine by Using Multiwalled Carbon Nanotube- Ionic Liquid Composite Electrode. Journal of Applied Chemical Research 12:42–52

40. Sultan S, Shah A, Firdous N, et al (2022) A Novel Electrochemical Sensing Platform for the Detection of the Antidepressant Drug, Venlafaxine, in Water and Biological Specimens. Chemosensors 10:400. https://doi.org/10.3390/chemosensors10100400

41. Madrakian T, Haryani R, Ahmadi M, Afkhami A (2016) A sensitive electrochemical sensor for rapid and selective determination of venlafaxine in biological fluids using carbon paste electrode modified with molecularly imprinted polymer-coated magnetite nanoparticles. J IRAN CHEM SOC 13:243–251. https://doi.org/10.1007/s13738-015-0731-8

42. Dourandish Z, Beitollahi H, Sheikhshoaie I (2023) Simultaneous Voltammetric Determination of Epinine and Venlafaxine Using Disposable Screen-Printed Graphite Electrode Modified by Bimetallic Ni-Co-Metal–Organic-Framework Nanosheets. Molecules 28:2128. https://doi.org/10.3390/molecules28052128

43. Ding L, Li L, You W, et al (2015) Electrocatalytic Oxidation of Venlafaxine at a Multiwall Carbon Nanotubes-Ionic Liquid Gel Modified Glassy Carbon Electrode and Its Electrochemical Determination. Croatica Chemica Acta 88:81–87. https://doi.org/10.5562/cca2420

44. Ali MFB, El-Zahry MR (2019) A comparative study of different electrodeposited NiCo2O4 microspheres anchored on a reduced graphene oxide platform: electrochemical sensor for anti-depressant drug venlafaxine. RSC Adv 9:31609–31620. https://doi.org/10.1039/C9RA04999A

45. Chen C, Chen Q (2008) RECENT DEVELOPMENT IN DIAMOND SYNTHESIS. International Journal of Modern Physics B 22:309–326

46. May PW (2000) Diamond thin films: a 21st-century material. Philosophical Transactions of the Royal Society of London Series A: Mathematical, Physical and Engineering Sciences. https://doi.org/10.1098/rsta.2000.0542

47. Haubner R (2021) Low-pressure diamond: from the unbelievable to technical products. ChemTexts 7:10. https://doi.org/10.1007/s40828-021-00136-z

48. Gracio JJ, Fan QH, Madaleno JC (2010) Diamond growth by chemical vapour deposition. J Phys D: Appl Phys 43:374017. https://doi.org/10.1088/0022-3727/43/37/374017

49. Arnault J-C, Saada S, Ralchenko V (2022) Chemical Vapor Deposition Single-Crystal Diamond: A Review. physica status solidi (RRL) – Rapid Research Letters 16:2100354. https://doi.org/10.1002/pssr.202100354

50. Sumant AV, Auciello O, Carpick RW, et al (2010) Ultrananocrystalline and Nanocrystalline Diamond Thin Films for MEMS/NEMS Applications. MRS Bulletin 35:281–288. https://doi.org/10.1557/mrs2010.550

51. Auciello O, Aslam DM (2021) Review on advances in microcrystalline, nanocrystalline and ultrananocrystalline diamond films-based micro/nano-electromechanical systems technologies. J Mater Sci 56:7171–7230. https://doi.org/10.1007/s10853-020-05699-9

52. Cheng H-Y, Yang C-Y, Yang L-C, et al (2018) Effective thermal and mechanical properties of polycrystalline diamond films. Journal of Applied Physics 123:165105. https://doi.org/10.1063/1.5016919

53. Williams OA (2011) Nanocrystalline diamond. Diamond and Related Materials 20:621–640. https://doi.org/10.1016/j.diamond.2011.02.015

54. Muchnikov AB, Vikharev AL, Gorbachev AM, et al (2010) Homoepitaxial single crystal diamond growth at different gas pressures and MPACVD reactor configurations. Diamond and Related Materials 19:432–436. https://doi.org/10.1016/j.diamond.2009.11.012

55. Macpherson J (2014) A practical guide to using boron doped diamond in electrochemical research. Physical chemistry chemical physics : PCCP 17:. https://doi.org/10.1039/c4cp04022h

56. D'Haenens-Johansson UFS, Butler JE, Katrusha AN (2022) Synthesis of diamonds and their identification. Reviews in Mineralogy and Geochemistry 88:689–753. https://doi.org/10.2138/rmg.2022.88.13

57. Achard J, Jacques V, Tallaire A (2020) Chemical vapour deposition diamond single crystals with nitrogen-vacancy centres: a review of material synthesis and technology for quantum sensing applications. J Phys D: Appl Phys 53:313001. https://doi.org/10.1088/1361-6463/ab81d1

58. Yang N, Yu S, V. Macpherson J, et al (2019) Conductive diamond: synthesis, properties, and electrochemical applications. Chemical Society Reviews 48:157–204. https://doi.org/10.1039/C7CS00757D

59. Einaga Y (2010) Diamond electrodes for electrochemical analysis. J Appl Electrochem 40:1807–1816. https://doi.org/10.1007/s10800-010-0112-z

60. Jackowska K, Krysinski P (2013) New trends in the electrochemical sensing of dopamine. Anal Bioanal Chem 405:3753–3771. https://doi.org/10.1007/s00216-012-6578-2

61. Baluchová S, Daňhel A, Dejmková H, et al (2019) Recent progress in the applications of boron doped diamond electrodes in electroanalysis of organic compounds and biomolecules – A review. Analytica Chimica Acta 1077:30–66. https://doi.org/10.1016/j.aca.2019.05.041

62. Baluchová S, Mamaloukou A, Koldenhof RHJM, Buijnsters JG (2023) Modification-free boron-doped diamond as a sensing material for direct and reliable detection of the antiretroviral drug nevirapine. Electrochimica Acta 450:142238. https://doi.org/10.1016/j.electacta.2023.142238

63. Hutton LA, Iacobini JG, Bitziou E, et al (2013) Examination of the Factors Affecting the Electrochemical Performance of Oxygen-Terminated Polycrystalline Boron-Doped Diamond Electrodes. Anal Chem 85:7230–7240. https://doi.org/10.1021/ac401042t

64. Souza FL, Saéz C, Lanza MRV, et al (2016) The effect of the sp3/sp2 carbon ratio on the electrochemical oxidation of 2,4-D with p-Si BDD anodes. Electrochimica Acta 187:119–124. https://doi.org/10.1016/j.electacta.2015.11.031

65. Garcia-Segura S, Vieira dos Santos E, Martínez-Huitle CA (2015) Role of sp3/sp2 ratio on the electrocatalytic properties of boron-doped diamond electrodes: A mini review. Electrochemistry Communications 59:52–55. https://doi.org/10.1016/j.elecom.2015.07.002

66. Sartori AF, Belardinelli P, Dolleman RJ, et al (2019) Inkjet-Printed High-Q Nanocrystalline Diamond Resonators. Small 15:1803774. https://doi.org/10.1002/smll.201803774

67. Sartori AF, Overes BHL, Fanzio P, et al (2019) Template-assisted bottom-up growth of nanocrystalline diamond micropillar arrays. Diamond and Related Materials 95:20–27. https://doi.org/10.1016/j.diamond.2019.03.017

68. Kondo T, Sakamoto H, Kato T, et al (2011) Screen-printed diamond electrode: A disposable sensitive electrochemical electrode. Electrochemistry Communications 13:1546–1549. https://doi.org/10.1016/j.elecom.2011.10.013

69. Kondo T, Horitani M, Sakamoto H, et al (2013) Screen-printed Modified Diamond Electrode for Glucose Detection. Chem Lett 42:352–354. https://doi.org/10.1246/cl.121242

70. Kondo T, Udagawa I, Aikawa T, et al (2016) Enhanced Sensitivity for Electrochemical Detection Using Screen-Printed Diamond Electrodes via the Random Microelectrode Array Effect. Anal Chem 88:1753–1759. https://doi.org/10.1021/acs.analchem.5b03986

71. Kondo T, Nakajima K, Osasa T, et al (2018) Effect of Substrate Size on the Electrochemical Properties of Boron-doped Diamond Powders for Screen-printed Diamond Electrode. Chem Lett 47:1464–1467. https://doi.org/10.1246/cl.180672

72. Matsunaga T, Kondo T, Osasa T, et al (2020) Sensitive electrochemical detection of ciprofloxacin at screen-printed diamond electrodes. Carbon 159:247–254. https://doi.org/10.1016/j.carbon.2019.12.051

73. Matsunaga T, Kondo T, Shitanda I, et al (2021) Sensitive electrochemical detection of l-Cysteine at a screen-printed diamond electrode. Carbon 173:395–402. https://doi.org/10.1016/j.carbon.2020.10.096

74. Chiao Y-H, Sivakumar M, Yadav S, et al (2021) Eco-friendly water-based graphene/sodium silicate dispersion for electrically conductive screen-printing technique and theoretical studies. Carbon 178:26–36. https://doi.org/10.1016/j.carbon.2021.02.089

75. Lohse D (2022) Fundamental Fluid Dynamics Challenges in Inkjet Printing. Annual Review of Fluid Mechanics 54:349–382. https://doi.org/10.1146/annurev-fluid-022321-114001

76. Li Y, Diddens C, Segers T, et al (2020) Evaporating droplets on oil-wetted surfaces: Suppression of the coffee-stain effect. Proceedings of the National Academy of Sciences 117:16756–16763. https://doi.org/10.1073/pnas.2006153117

77. Kim J-H, Kim K-S, Jang K-R, et al (2015) Enhancing Adhesion of Screen-Printed Silver Nanopaste Films. Advanced Materials Interfaces 2:1500283. https://doi.org/10.1002/admi.201500283

78. Dbira S, Bensalah N, Bedoui A, et al (2015) Treatment of synthetic urine by electrochemical oxidation using conductive-diamond anodes. Environ Sci Pollut Res 22:6176–6184. https://doi.org/10.1007/s11356-014-3831-6

79. Parham H, Zargar B (2001) Determination of isosorbide dinitrate in arterial plasma, synthetic serum and pharmaceutical formulations by linear sweep voltammetry on a gold electrode. Talanta 55:255–262. https://doi.org/10.1016/S0039-9140(01)00416-7

80. Liu Z, Sartori AF, Buijnsters JG (2021) Role of sp2 carbon in non-enzymatic electrochemical sensing of glucose using boron-doped diamond electrodes. Electrochemistry Communications 130:107096. https://doi.org/10.1016/j.elecom.2021.107096

81. Stratmann Differential Pulse Voltammetry (DPV). In: PalmSens. https://www.palmsens.com/knowledgebase-article/differential-pulse-voltammetry-dpv/. Accessed 28 Jul 2023

82. Fortunato W, Chiquito AJ, Galzerani JC, Moro JR (2007) Crystalline quality and phase purity of CVD diamond films studied by Raman spectroscopy. J Mater Sci 42:7331–7336. https://doi.org/10.1007/s10853-007-1575-0

83. Mortet V, Živcová ZV, Taylor A, et al (2019) Determination of atomic boron concentration in heavily boron-doped diamond by Raman spectroscopy. Diamond and Related Materials 93:54–58. https://doi.org/10.1016/j.diamond.2019.01.028

84. Xu J, Yokota Y, Wong RA, et al (2020) Unusual Electrochemical Properties of Low-Doped Boron-Doped Diamond Electrodes Containing sp2 Carbon. J Am Chem Soc 142:2310–2316. https://doi.org/10.1021/jacs.9b11183

85. Siraj S, McRae CR, Wong DKY (2021) Hydrogenating carbon electrodes by n-butylsilane reduction to achieve an antifouling surface for selective dopamine detection. Sensors and Actuators B: Chemical 327:128881. https://doi.org/10.1016/j.snb.2020.128881

86. Chemicalize - Instant Cheminformatics Solutions. In: Chemicalize. https://chemicalize.com. Accessed 21 Sep 2023

# 8 Appendix

## 8.1 Supplemental figures

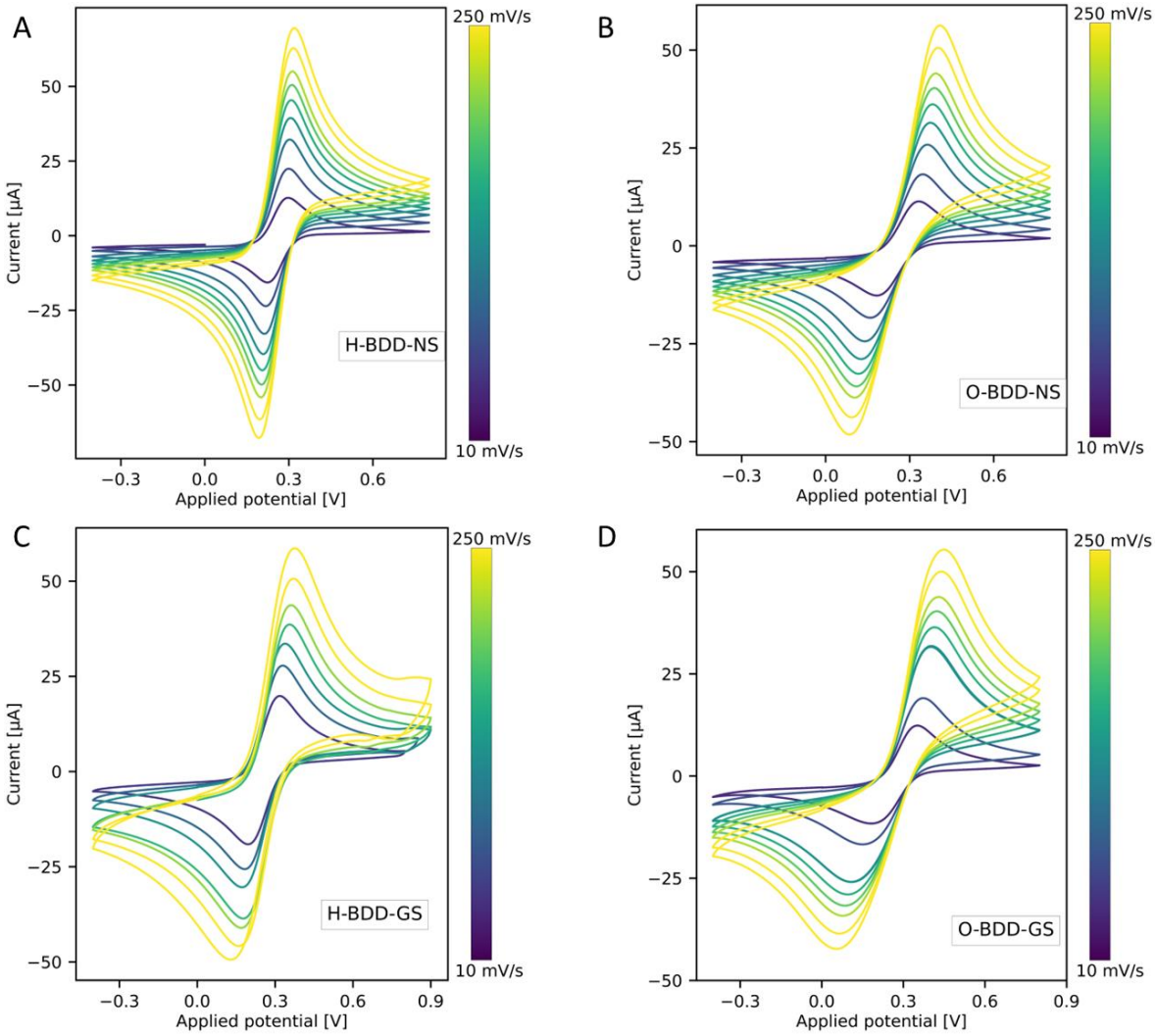


*Figure A.1. A scan rate study (10-250 mV/s) of $[Fe(CN)_6]^{3-/4-}$ on four different surface combinations: A) H-BDD-NS, B) O-BDD-NS, C) H-NDD-GS, and D) O-BDD-GS.*

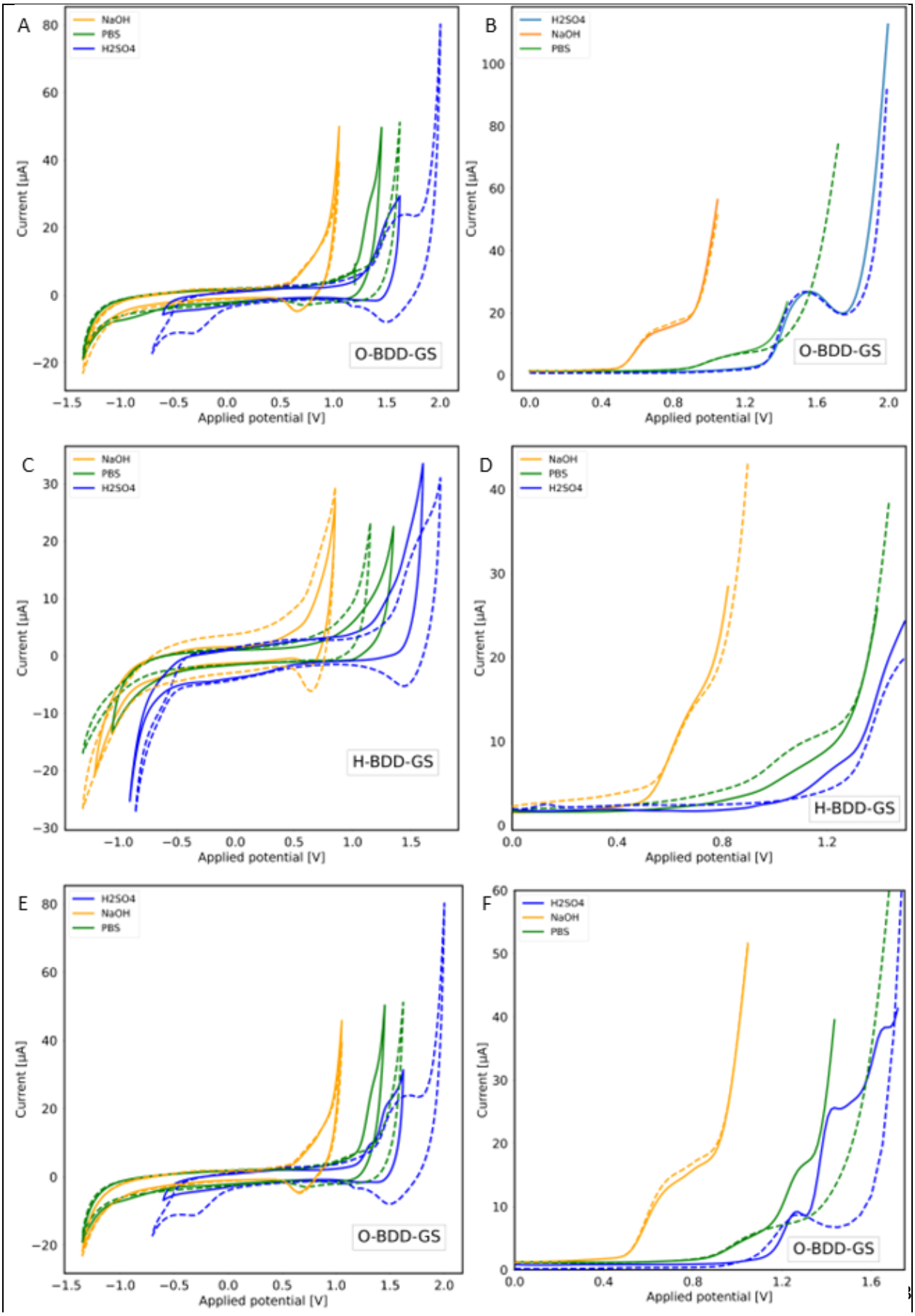
A
NaOH
PBS
H2SO4
O-BDD-GS
Current [µA]
Applied potential [V]
B
H2SO4
NaOH
PBS
O-BDD-GS
Current [µA]
Applied potential [V]
C
NaOH
PBS
H2SO4
H-BDD-GS
Current [µA]
Applied potential [V]
D
NaOH
PBS
H2SO4
H-BDD-GS
Current [µA]
Applied potential [V]
E
H2SO4
NaOH
PBS
O-BDD-GS
Current [µA]
Applied potential [V]
F
H2SO4
NaOH
PBS
O-BDD-GS
Current [µA]
Applied potential [V]

*Figure A.2. Continued*

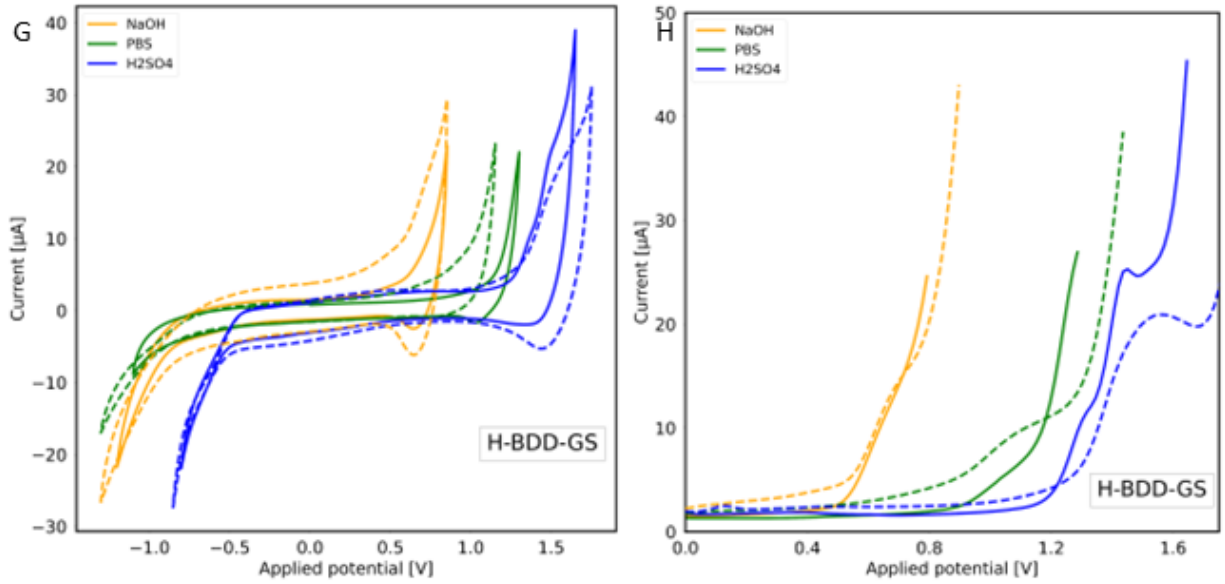


*Figure A.2. (A, C, E, G) Cyclic voltammograms and (B, D, F, H) DP voltammograms of (A, B, C, D) 100 µM DVF and (E, F, G, H) 100 µM VF recorded on (A, B, E, F) O-BDD-GS and (C, D, G, H)H-BDD-G S in varying supporting electrolytes. The dashed lines correspond to the supporting electrolyte without any compound.*

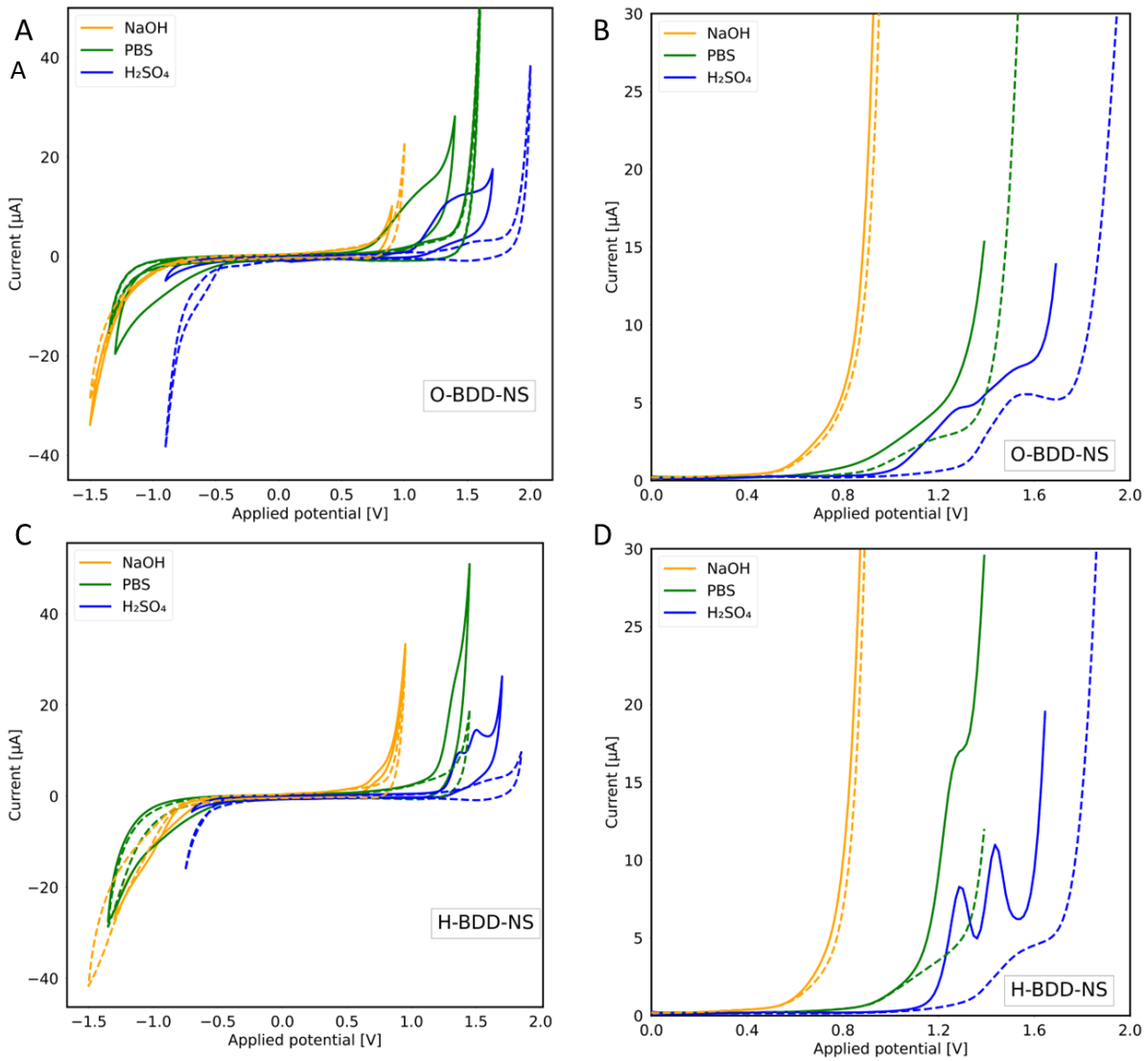


*Figure A.3 (A,C) Selected CVs and (B,D) DP voltammograms of (A, B) 100 µM DVF recorded on O-BDD-NS and (C, D) VF recorded on H-BDD-NS, recorded in various electrolyte solutions. The dashed lines correspond to the supporting electrolyte.*

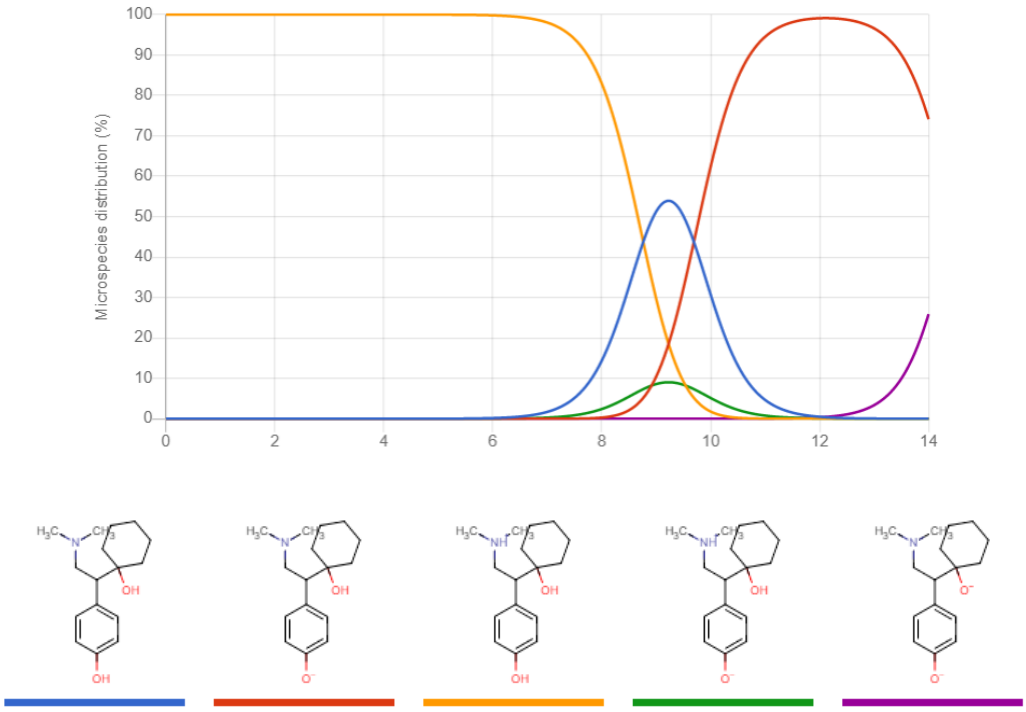


*Figure A.4. The effects of pH on the molecular form of DVF* [86].

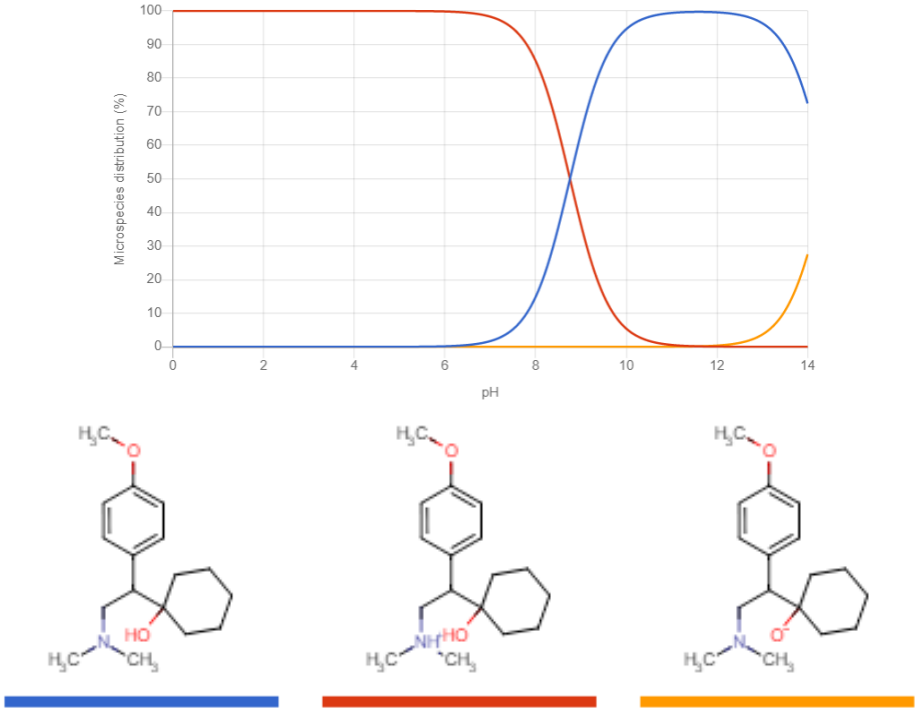


*Figure A.4. The effects of pH on the molecular form of VF* [86].

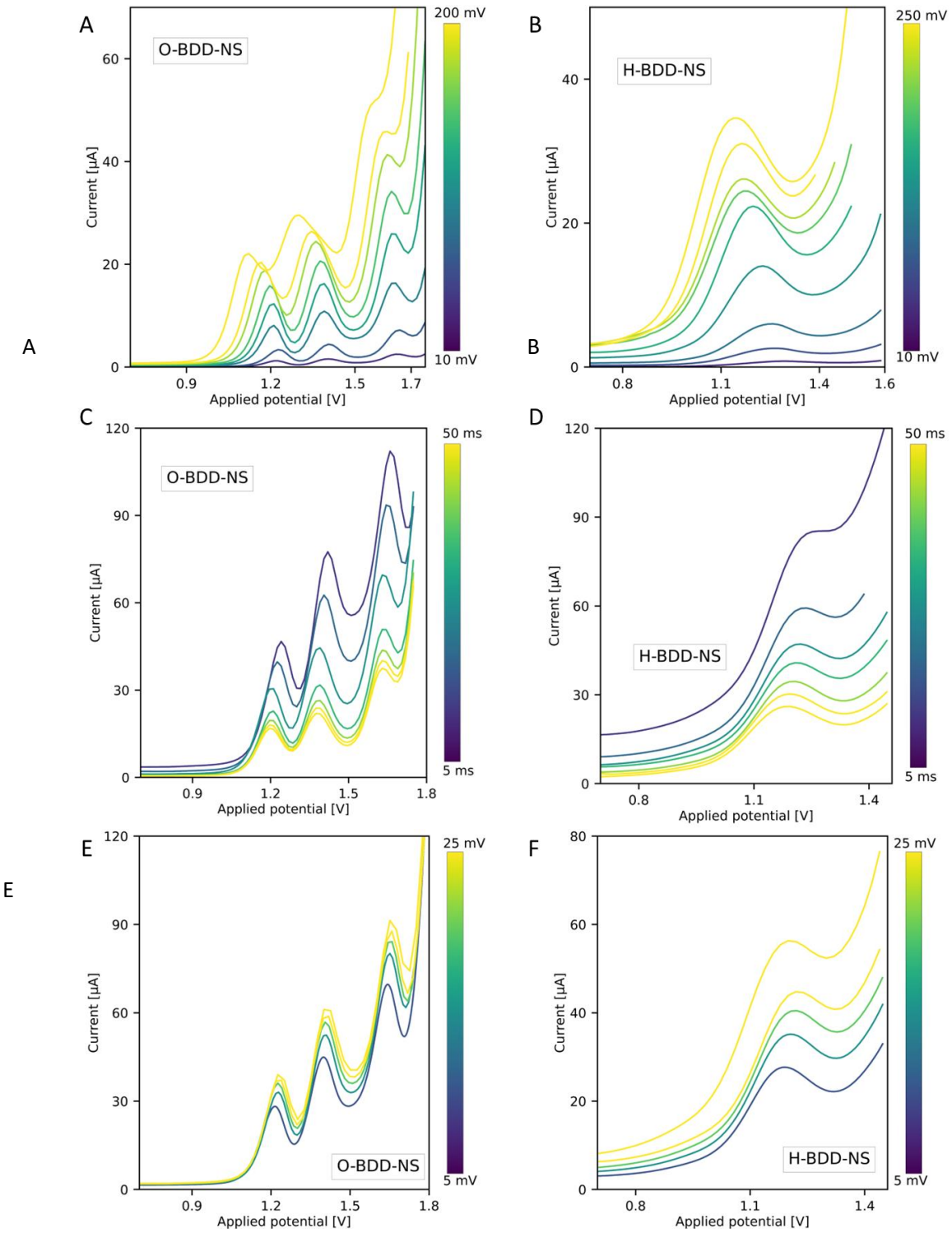


*Figure A.6. (A, C, E) The 100 µM VF in 0.1 M $H_2SO_4$ (pH 0.6) on O-BDD and (B, D, F) 100 µM DVF in 0.1 M $H_2SO_4$ (pH 0.6) on H-BDDS curves for DPV parameter optimization, (A, B) the modulation amplitude (10-100 mV), (C, D) modulation time (5-50 ms) and (E,F) step size (5-25 mV) are all illustrated.*

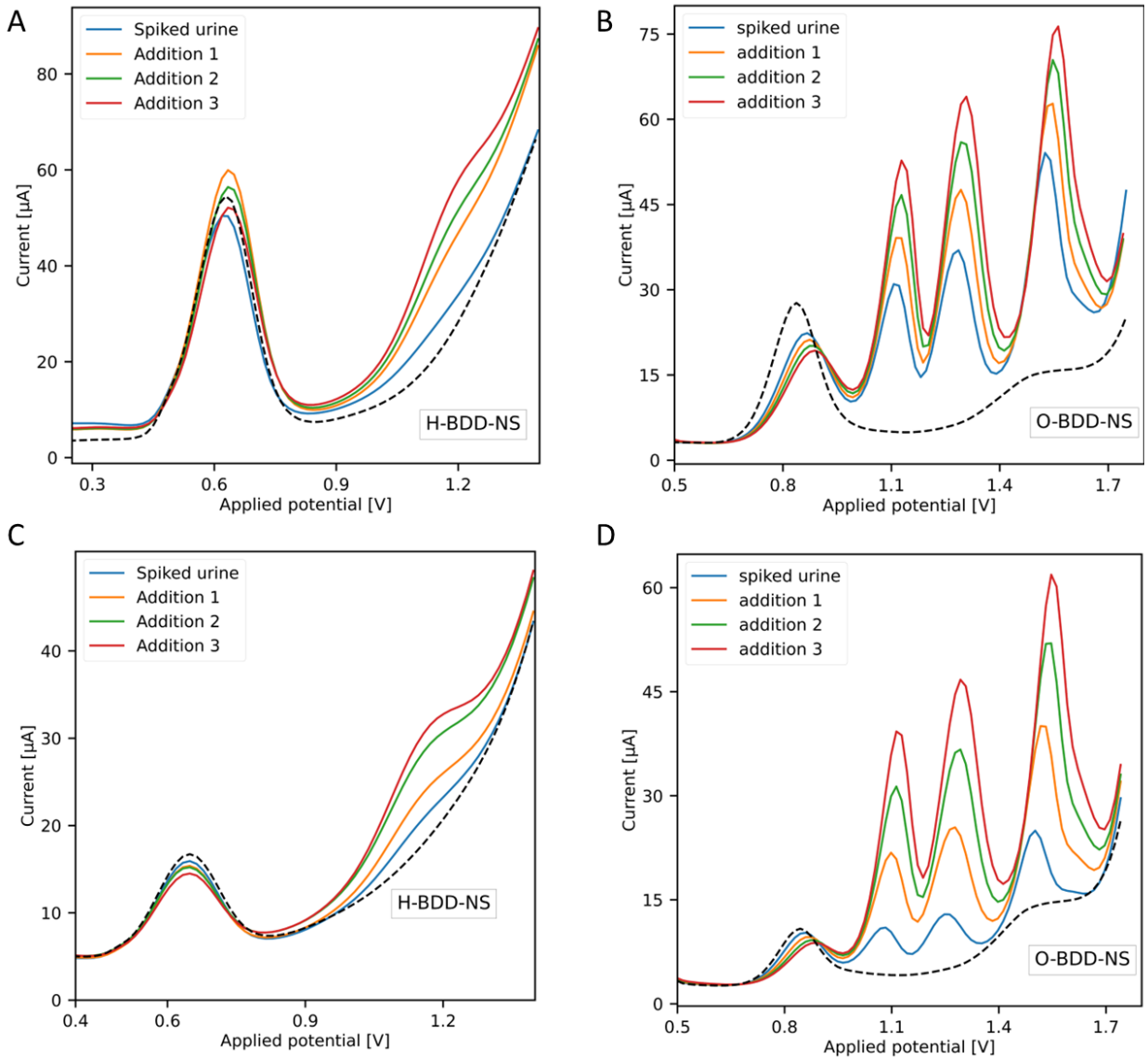


*Figure A.7. DPV curves recorded in synthetic urine samples diluted with 0.1 M $H_2SO_4$ in 1:1 (A,B) and 1:9 (C,D) ratio. Spiked with 25 µM (1:1) and 5 µM (1:4) of DVF (A,C) or VF(B,D) and followed by three standard additions of 100 µL, 1 mM VF or DVF. The dashed lines correspond to the diluted urine samples.*

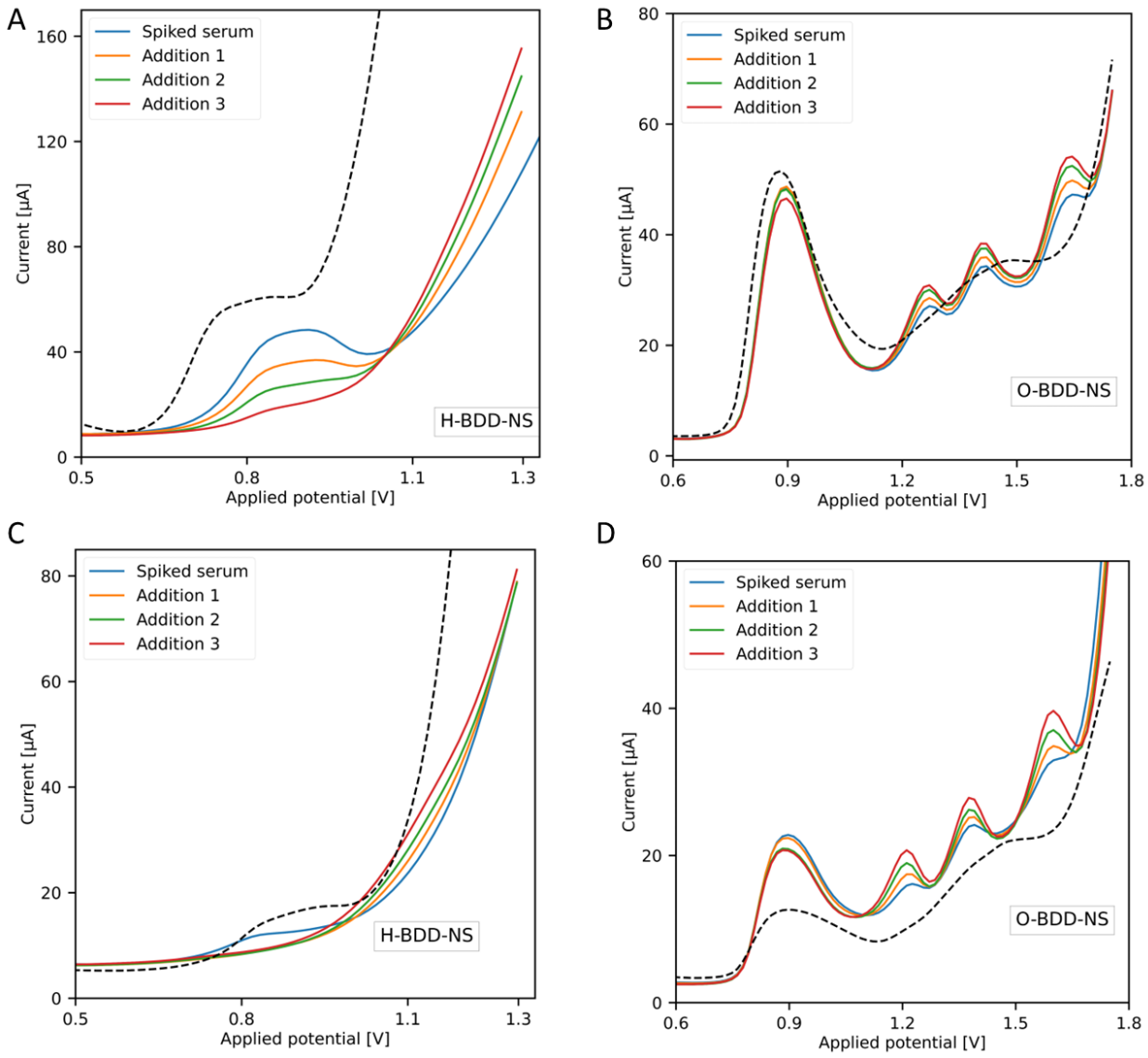


*Figure A.8. DPV curves recorded in synthetic serum samples diluted with 0.1 M $H_2SO_4$ in 1:1 (A,B) and 1:9 (C,D) ratio. Spiked with 25 µM (1:1) and 5 µM (1:4) of DVF (A,C) or VF(B,D) and followed by three standard additions of 100 µL, 1 mM VF or DVF. The dashed lines correspond to the diluted serum samples.*

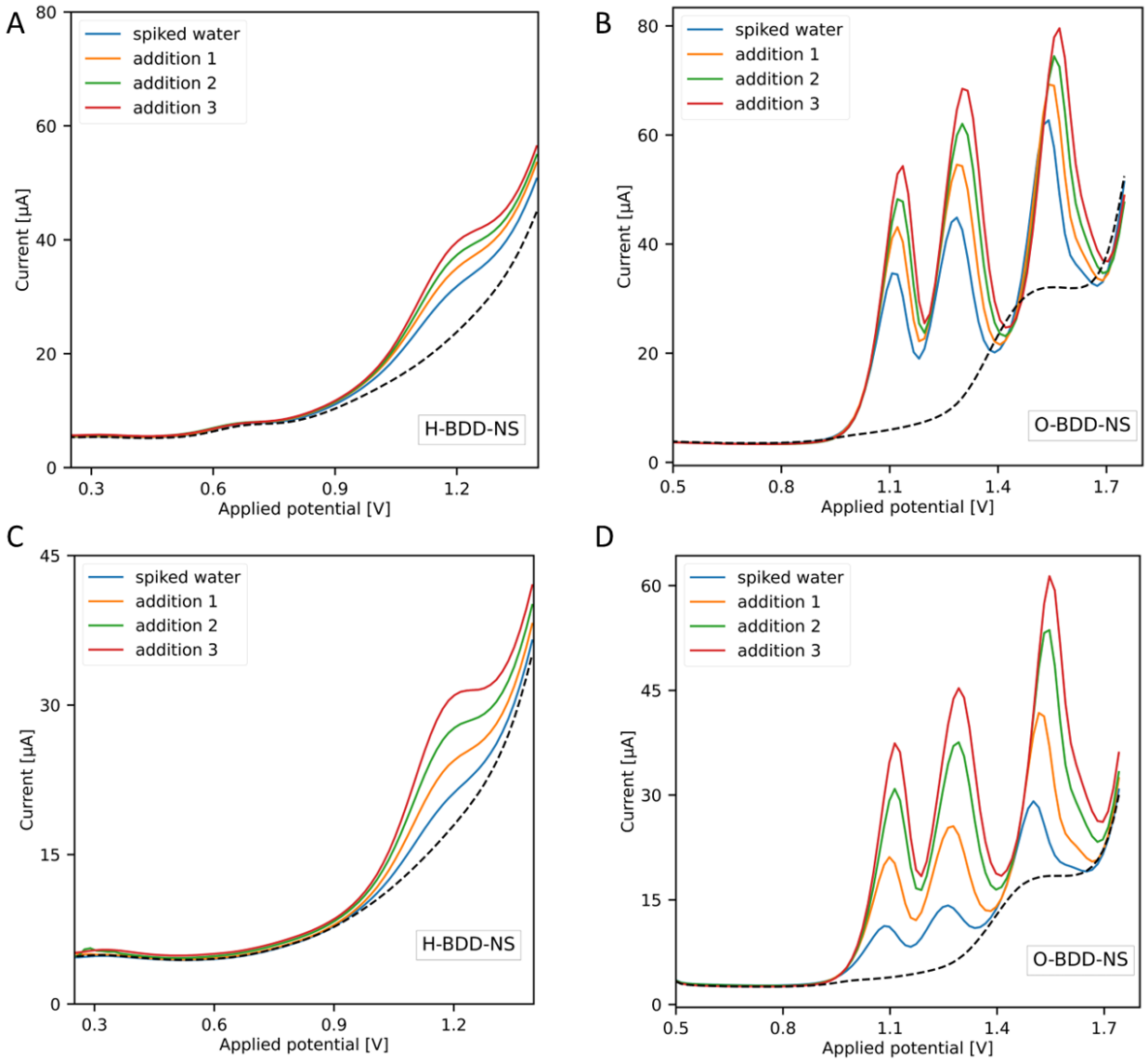


*Figure A.9. DPV curves recorded in river water samples diluted with 0.1 M $H_2SO_4$ in 1:1 (A,B) and 1:9 (C,D) ratio. Spiked with 25 µM (1:1) and 5 µM (1:4) of DVF (A,C) or VF(B,D) and followed by three standard additions of 100 µL, 1 mM VF or DVF. The dashed lines correspond to the diluted river samples.*

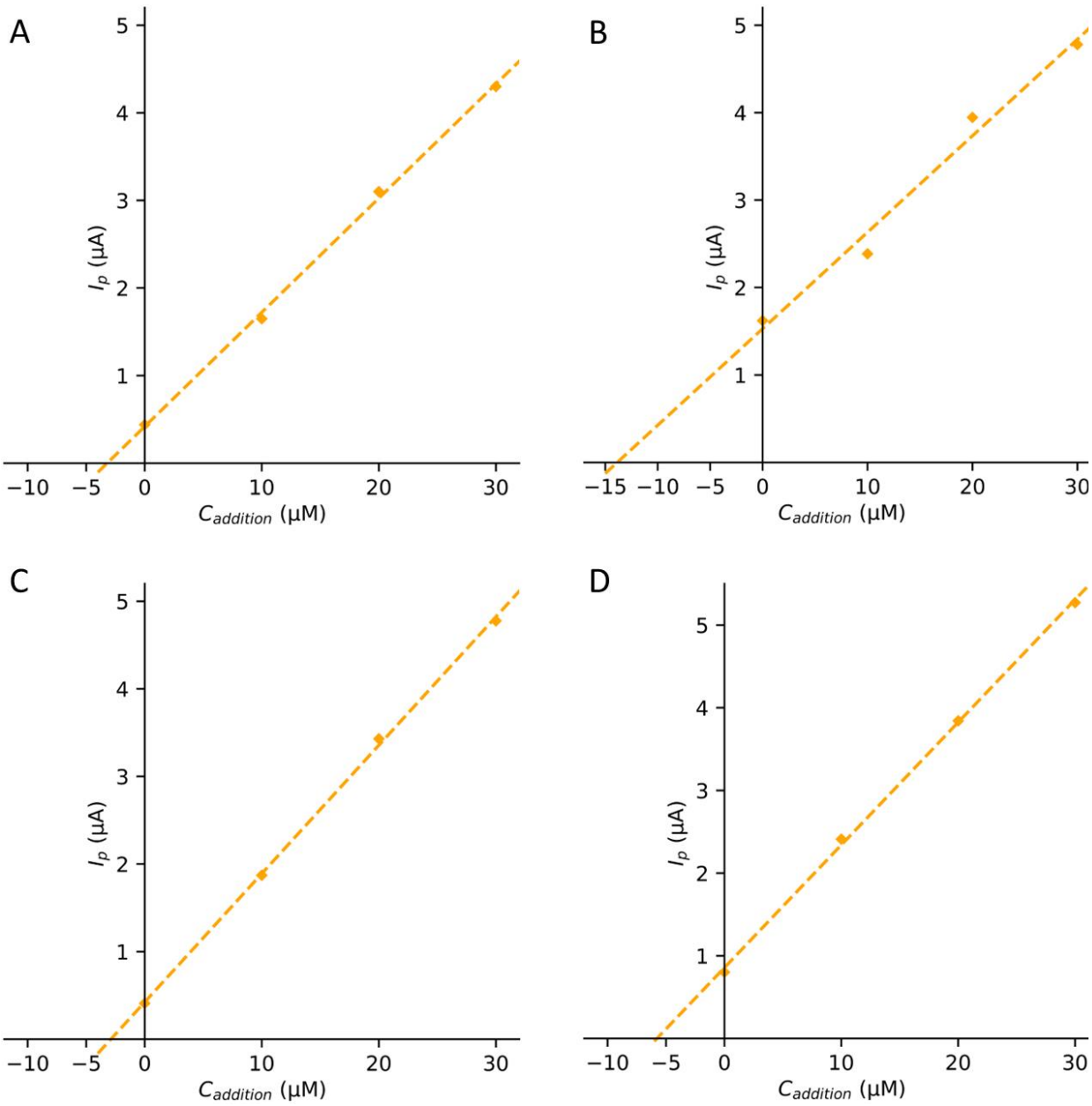


*Figure A.10. The graphical quantification of the standard addition method of spiked DVF on H-BDD-NS (5 μM, 5 μM, 10 μM, 25 μM) in (A) 1:9 synthetic urine in 0.1 M $H_2SO_4$ and (B) 1:1, (C) 1:4 and (D) 1:9 river water in 0.1 M $H_2SO_4$.*

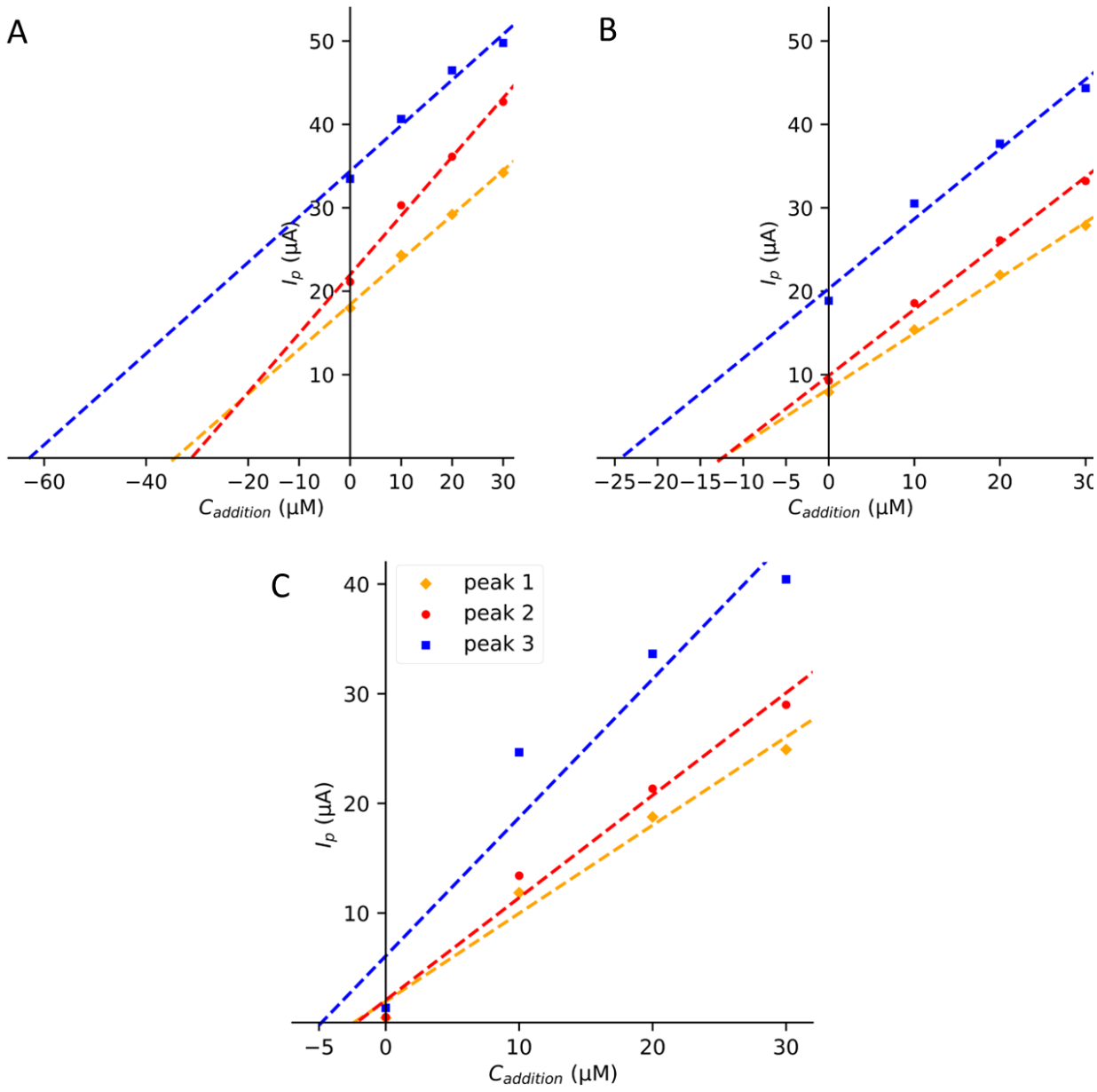


*Figure A.11. The graphical quantification of the standard addition method of spiked VF on O-BDD-NS (5 μM, 10 μM, 25 μM) in (A) 1:1, (B) 1:4 and (C) 1:9 synthetic urine in 0.1 M $H_2SO_4$.*

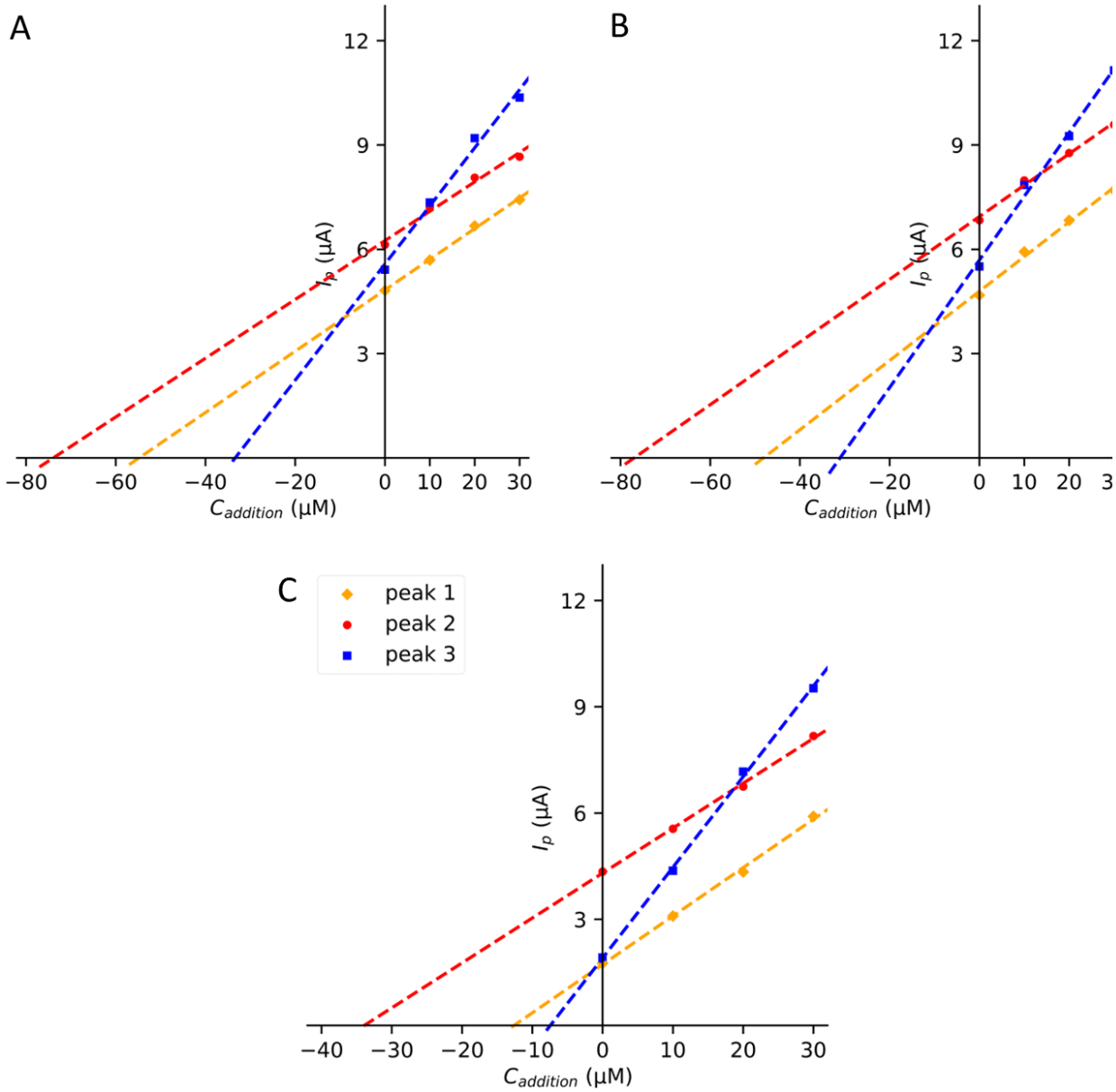


*Figure A.12. The graphical quantification of the standard addition method of spiked VF on O-BDD-NS (5 µM, 10 µM, 25 µM) in (A) 1:1, (B) 1:4 and (C) 1:9 synthetic serum in 0.1 M $H_2SO_4$.*

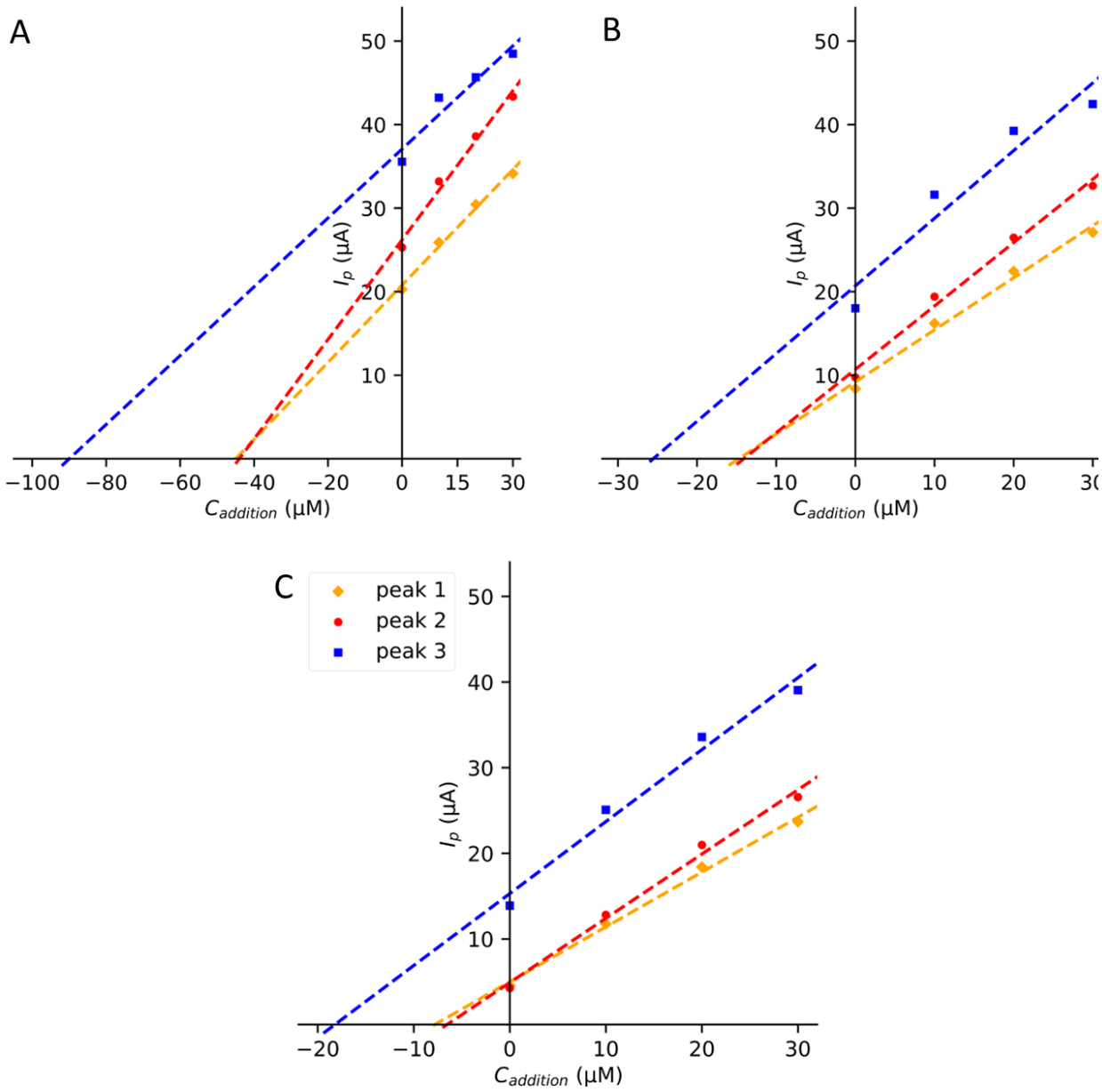


*Figure A.13. The graphical quantification of the standard addition method of spiked VF on O-BDD-NS (5 μM, 10 μM, 25 μM) in (A) 1:1, (B) 1:4 and (C) 1:9 river water in 0.1 M $H_2SO_4$.*

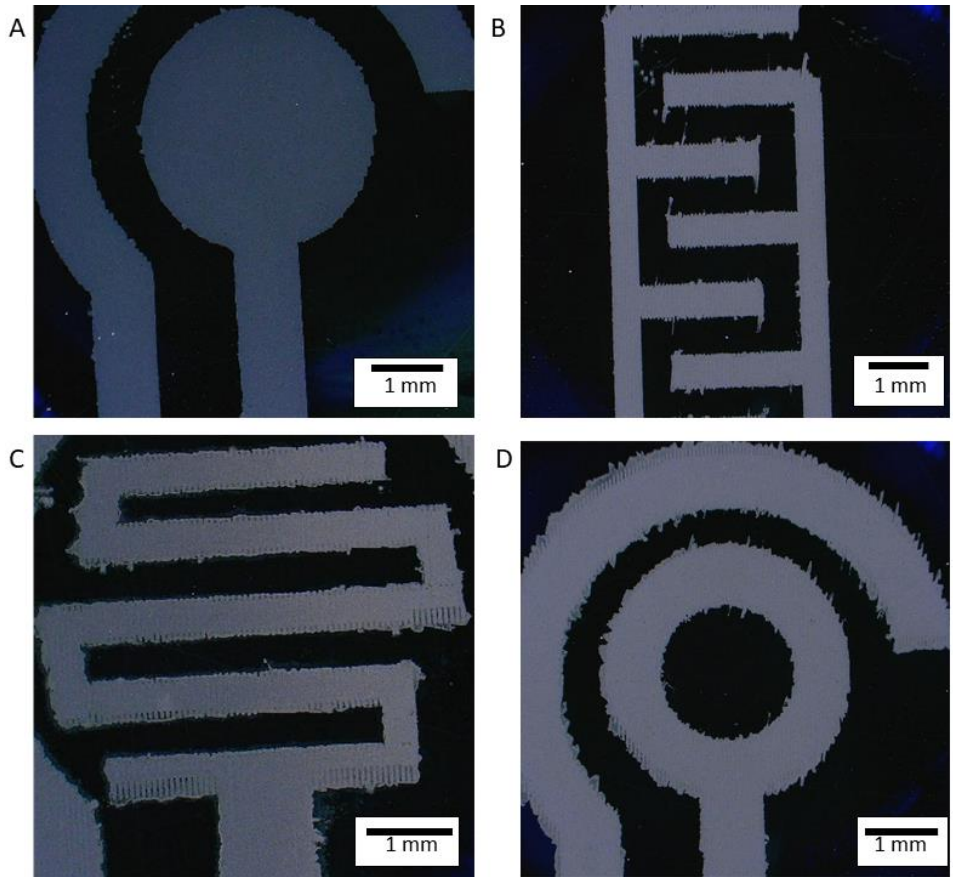


*Figure A.14. Digital microscopy images of the (A) circular, (B) interdigitated, (C) Line, and (D) circular with a hole inkjet-seeded diamond electrode patterns after BDD growth by UHasselt.*